SNOW DEPTH AND SWE ESTIMATION USING SPACEBORNE POLARIMETRIC AND INTERFEROMETRIC SYNTHETIC APERTURE RADAR

SAYANTAN MAJUMDAR
March, 2019

SUPERVISORS:
Dr. Praveen K. Thakur
Dr. Ling Chang
Advisor: Mr. Shashi Kumar

SNOW DEPTH AND SWE ESTIMATION USING SPACEBORNE POLARIMETRIC AND INTERFEROMETRIC SYNTHETIC APERTURE RADAR

SAYANTAN MAJUMDAR
Enschede, The Netherlands, March, 2019

Thesis submitted to the Faculty of Geo-Information Science and Earth Observation of the University of Twente in partial fulfilment of the requirements for the degree of Master of Science in Geo-information Science and Earth Observation.
Specialization: Geoinformatics

SUPERVISORS:
Dr. Praveen K. Thakur
Dr. Ling Chang
Advisor: Mr. Shashi Kumar

THESIS ASSESSMENT BOARD:
Prof. Dr. Ir. A. Stein (Chair, ITC Professor)
Dr. Snehmani (External Examiner, Snow and Avalanche Study Establishment (SASE))

"In this world, wherever there is light— there are also shadows."
-Madara Uchiha

ABSTRACT

Snow depth (SD) and Snow Water Equivalent (SWE) are two of the essential physical properties of snow. These are extensively used in the hydrological modelling domain for various avalanche and snow-melt runoff simulations. However, accurate large-scale measurement of the SD and SWE is still an ongoing research problem in the cryosphere paradigm due to the significant influence of the hydrometeorological conditions present in the area of interest. This is where the satellite remote sensing techniques are able to provide effective solutions over traditional in-situ measurements. In the past few decades, synthetic aperture radar (SAR) has been widely used in the cryospheric studies which mainly concern with the snow property retrieval, such as SD, SWE, and snow density. Moreover, spaceborne SAR systems benefit from global coverage at sufficiently high spatial resolutions. Recently, the copolar phase difference (CPD) method based on the X-band polarimetric SAR (PolSAR) technique has displayed promising results regarding the fresh snow depth (FSD) estimation. Still, this FSD inversion model has not been tested in the presence of extreme topographically varying conditions, such as the northwestern Himalayan belt. It is also susceptible to high volume scattering at X-band occurring from the increased snow grain sizes as a result of the standing (or old) snow formation driven by the temperature induced snow metamorphosis process. Hence, to model this volume decorrelation, the polarimetric SAR interferometry (Pol-InSAR) technique can be applied which has already provided highly accurate tree height estimates in prior studies. In this work, the FSD and standing snow depth (SSD) are computed using the PolSAR CPD method and the single-baseline Pol-InSAR based hybrid Digital Elevation Model (DEM) differencing and coherence amplitude inversion model. To achieve this, the TerraSAR-X, TanDEM-X Coregistered Single look Slant range Complex (CoSSC) bistatic acquisition over Dhundi (situated in the Beas watershed, northwestern Himalayas, India) on January 8, 2016, is used. Although meant for flexibility, these models involve several free parameters requiring data specific optimisation. Moreover, since the study area is characterised by steep slopes and forests, there exist significant uncertainty sources which exhibit temporally varying scattering mechanisms. Additionally, the ground-truth measurements are limited (only two points are available, with one falling in the layover area for descending pass acquisitions). As a result, appropriate sensitivity analyses have been carried out for the parameter optimisation. Furthermore, the uncertainty sources are identified by performing a summer (June 8, 2017) and wintertime (January 8, 2016) comparative analysis of the study area which quantitatively highlights the changes in the percentages of the surface and volume scatterings. Apart from this, a suitable error analysis is conducted for the reference ALOS PALSAR DEM using the Differential Global Positioning System (DGPS) readings acquired during the fieldwork. This showed that the elevation errors do not significantly modify the local incidence angle (LIA) values which are used in the FSD and SSD inversion algorithms. Evidently, the improved models display sufficiently high FSD and SSD accuracies of 94.83% and 99.53% respectively with the corresponding fresh SWE (FSWE) and standing SWE (SSWE) accuracies of 94.84% and 99.48% (these are measured over a 3×3 neighbourhood window surrounding Dhundi). Therefore, in summary, the overall outcome of this research showcases the practicability of these PolSAR and Pol-InSAR models in the context of the SD estimation over rugged terrains.

Keywords: Synthetic Aperture Radar, Copolar Phase Difference, Pol-InSAR, Snow Physical Properties, Sensitivity Analysis

NOMENCLATURE

List of acronyms

3DVAR	Three Dimensional Variation
AWS	Automatic Weather Station
BSA	Backscattering alignment
CoSSC	Coregistered Single look Slant Range Complex
CPD	Copolar Phase Difference
CT	Computer Tomography
DB	Database
DEM	Digital Elevation Model
DGPS	Differential Global Positioning System
D-InSAR	Differential InSAR
Doris	Delft object-oriented radar interferometric software
DSD	Dry Snow Depth
EM	Electromagnetic
EnKF	Ensemble Kalman Filter
FSCA	Fresh Snow Cover Area
FSD	Fresh Snow Depth
FSWE	Fresh Snow Water Equivalent
GPR	Ground Penetrating Radar
HH	Horizontal transmit Horizontal receive (linear polarisation)
HPC	High-Performance Computing
HV	Horizontal transmit Vertical receive (linear polarisation)
IDE	Integrated Development Environment
IIRS	Indian Institute of Remote Sensing
InSAR	Interferometric SAR
IST	Indian Standard Time
LIA	Local Incidence Angle
LiDAR	Light Detection and Ranging
LL	Left transmit Left receive (circular polarisation)
LR	Left transmit Right receive (circular polarisation)
NE	Northeast
NIR	Near-infrared
NW	Northwest
Pol-InSAR	Polarimetric SAR Interferometry/Polarimetric InSAR
PolSAR	Polarimetric SAR
Radar	Radio detection and ranging
RAR	Real Aperture Radar
RMSE	Root Mean Square Error
rp-InSAR	Repeat-pass InSAR
RR	Right transmit Right receive (circular polarisation)
RVoG	Random Volume over Ground
SA	Sensitivity Analysis
SAR	Synthetic Aperture Radar
SD	Snow Depth
SE	Southeast

SM	Stripmap (SAR acquisition mode)
SNAP	Sentinel Application Platform
SNR	Signal-to-Noise Ratio
SPA	Snowpack Analyser
sp-InSAR	Single-pass InSAR
SSCA	Standing Snow Cover Area
SSD	Standing Snow Depth
SSWE	Standing Snow Water Equivalent
SW	Southwest
SWE	Snow Water Equivalent
TDX	TanDEM-X
TSX	TerraSAR-X
UTC	Universal Time Coordinated
UTM	Universal Transverse Mercator
VH	Vertical transmit Horizontal receive (linear polarisation)
VV	Vertical transmit Vertical receive (linear polarisation)
WRD	Water Resources Department
WSD	Wet Snow Depth

List of symbols

ϵ_{ice}	Complex or effective permittivity (relative) of ice
ϵ_{air}	Relative permittivity of air
ϵ_{water}	Relative permittivity of water
ϵ_{snow}	Complex or effective permittivity (relative) of snow
N_i	Depolarisation factor, $i \in \{x, y, z\}$ in a 3D Cartesian coordinate system
$\epsilon_{eff,i}$	Effective permittivity of snow, $i \in \{x, y, z\}$
λ_0	Radar wavelength (cm)
θ	Mean incidence angle (rad)
θ_r	Microwave refraction angle obtained at the snow-air interface (rad)
k_z	Vertical wavenumber (rad/m)
m	Parameter used to calculate $k_z, m = 1$ for sp-InSAR and $m = 2$ for rp-InSAR
α	Scattering alpha angle (°) which lies in the interval [0°, 90°]
β	Target orientation angle (°) obtained from the scattering mechanism defined by α which lies in the interval [0°, 180°]
μ_f	Mean FSD (cm) calculated over a neighbourhood window
μ_{fs}	Mean FSWE (mm) calculated over a neighbourhood window
μ_s	Mean SSD (cm) calculated over a neighbourhood window
μ_{ss}	Mean SSWE (mm) calculated over a neighbourhood window
σ_f	FSD standard deviation (cm) calculated over a neighbourhood window
σ_s	SSD standard deviation (cm) calculated over a neighbourhood window
σ_{fs}	FSWE standard deviation (mm) calculated over a neighbourhood window
σ_{ss}	SSWE standard deviation (mm) calculated over a neighbourhood window
σ_e	Snow extinction coefficient
$\overline{\sigma_e}$	Mean snow extinction coefficient
ρ_{ice}	Ice density (g/cm^3)

ρ_{snow}	Snow density (g/cm³)
ρ_f	Fresh snow density (g/cm³)
ρ_d	Dry snow density (g/cm³)
ρ_s	Standing snow density (g/cm³)
$\rho_{critical}$	Maximum seasonal snow density limit (g/cm³)
γ_c	Copolar coherence amplitude which lies in the interval [0, 1]
$\widetilde{\gamma_c}$	Complex copolar coherence
$\gamma(\overrightarrow{w_v})$	Volume coherence amplitude which works on the volume scattering weight vector $\overrightarrow{w_v}$ and lies in the interval [0, 1]
$\tilde{\gamma}(\overrightarrow{w_v})$	Complex volume coherence which works on the volume scattering weight vector $\overrightarrow{w_v}$
$\gamma(\overrightarrow{w_s})$	Surface coherence amplitude which works on the surface scattering weight vector $\overrightarrow{w_s}$ and lies in the interval [0, 1]
$\tilde{\gamma}(\overrightarrow{w_s})$	Complex surface coherence which takes the surface scattering weight vector $\overrightarrow{w_s}$
$\widetilde{\gamma_v}$	Complex volume decorrelation
ϕ_{total}^u	Total absolute InSAR phase ((rad)) which belongs to the set of real numbers $\mathbb{R}$
ϕ_{atm}^u	Absolute atmospheric phase (rad) which belongs to the set of real numbers $\mathbb{R}$
ϕ_{flat}^u	Absolute flat-earth phase (rad) which belongs to the set of real numbers $\mathbb{R}$
ϕ_{flat}^w	Wrapped flat-earth phase (rad) in the interval [0, 2π)
ϕ_{topo}^u	Absolute topographical or ground phase (rad) which belongs to the set of real numbers $\mathbb{R}$
ϕ_{topo}^w	Wrapped topographical or ground phase (rad) in the interval [0, 2π)
ϕ_{snow}^u	Absolute snow phase (rad) which belongs to the set of real numbers $\mathbb{R}$
ϕ_{noise}^u	Random absolute phase noise (rad) which belongs to the set of real numbers $\mathbb{R}$
ϕ_0^w	Free parameter (rad) in the Pol-InSAR height retrieval model which lies in the interval [0, 2π)
ϕ_{CPD}	CPD (rad) which lies in the interval $[-\pi, \pi]$
$\overline{\phi_{CPD}}$	Mean CPD (rad) which lies in the interval $[-\pi, \pi]$
$\phi_{CPD,TDX}$	CPD for the TDX data (rad) which lies in the interval $[-\pi, \pi]$
$\phi_{CPD,TSX}$	CPD for the TSX data (rad) which lies in the interval $[-\pi, \pi]$
$\arg(\dots)$	Argument function which gives the phase of a complex number in the interval [0, 2π)
η	SSD scaling parameter which lies in the interval [0, 1]
η'	Vertical wavenumber scaling parameter which belongs to the set $\mathbb{R}_{>0}^+$
k_z'	Scaled vertical wavenumber
$\mathbb{R}_{>0}^+$	Set of all positive real numbers which lies in the interval (0, ∞)
ΔZ_f	FSD (cm)
ΔZ_s	SSD (cm)
ΔZ_d	DSD (cm)
ΔZ_{snow}	Generic SD (cm) which can denote either of FSD, SSD or DSD
$I(\overrightarrow{w_1}, \overrightarrow{w_2})$	Pol-InSAR interferogram which takes two scattering weight vectors $\overrightarrow{w_1}$ and $\overrightarrow{w_2}$
$\tilde{\gamma}(\overrightarrow{w_1}, \overrightarrow{w_2})$	Complex Pol-InSAR coherence which takes two scattering weight vectors $\overrightarrow{w_1}$ and $\overrightarrow{w_2}$
$\tilde{\gamma}(\overrightarrow{w_1})$	Complex Pol-InSAR coherence for the weight vectors $\overrightarrow{w_1} = \overrightarrow{w_2}$
$\vec{w}$	General weight vector for Pol-InSAR coherence calculation
$\Re(\dots)$	Gives the real part of a complex number
$\Im(\dots)$	Gives the imaginary part of a complex number
S_{HH}, S_{VV}	Scattering matrix for the HH and VV channels respectively
a_x, a_y, a_z	Orthogonal axes in the three directions x, y, z of a 3D Cartesian coordinate system
α_s	Constant in the snow depth and permittivity relation (cm³/g)

β_s	Constant in the snow depth and permittivity relation (cm^9/g^3)
$\Delta\zeta$	Relative path length difference used in the FSD estimation
f_{vol}	Snow volume fraction
n_H, n_V	Refractive indices of snow for the HH and VV polarisations respectively
χ	Surface to volume scattering ratio which lies in the interval [0, 1]
e_1, e_2	Eccentricities of a prolate (e_1) and an oblate (e_2)
ϑ	Free parameter ($\approx$ 1) in the dense time-series D-InSAR based SWE estimation model
ΔR	Slant range difference (m) between snow and non-snow time
ΔR_s	Slant range distance (m) for a non-moving target during the snow-free time
ΔR_a	Slant range distance (m) measured at the snow-air interface
μ_{γ_c}	Mean γ_c (calculated over a window) which lies in the interval [0, 1]
σ_{γ_c}	Standard deviation of the γ_c (calculated over a window) which lies in the interval [0, 1]
$\mu_{\gamma(\overrightarrow{w_v})}$	Mean $\gamma(\overrightarrow{w_v})$ (calculated over a window) which lies in the interval [0, 1]
$\sigma_{\gamma(\overrightarrow{w_v})}$	Standard deviation of the $\gamma(\overrightarrow{w_v})$ (calculated over a window) which lies in the interval [0, 1]
$\mu_{\gamma(\overrightarrow{w_s})}$	Mean $\gamma(\overrightarrow{w_s})$ (calculated over a window) which lies in the interval [0, 1]
$\sigma_{\gamma(\overrightarrow{w_s})}$	Standard deviation of the $\gamma(\overrightarrow{w_s})$ (calculated over a window) which lies in the interval [0, 1]
τ_v	Thresholding applied on $\gamma(\overrightarrow{w_v})$ which lies in the interval [0, 1]
τ_c	Thresholding applied on γ_c which lies in the interval [0, 1]
sinc	Traditional sine cardinal function
sinc_π	Normalised sine cardinal function
sinc_C^{-1}	Inverse (rad) of the sinc function computed using the Cloude (2010) approximation
sinc_S^{-1}	Inverse (rad) of the sinc function computed using the secant method
$\mathrm{sinc}_{\pi_C}^{-1}$	Inverse (rad) of the sinc_π function computed using the Cloude (2010) approximation
$\mathrm{sinc}_{\pi_S}^{-1}$	Inverse (rad) of the sinc_π function computed using the secant method
$\mathbb{C}$	Set of complex numbers
ψ	Angle (rad) which belongs to $\mathbb{C}$ and is used as the parameter in the sinc and sinc_π functions
α_r	Inverse (rad) of the sinc function which in general terms belong to $\mathbb{C}$, however, for numerical root finding algorithms, $\alpha_r \in \mathbb{R}$ is returned as the inverse or root
θ_l	Local incidence angle (°)
ω_x, ω_y	Slope angles (°) in the x and y directions of the pixel co-ordinate system.
A_f	Fresh snow cover area (km^2) based on either of terrain aspect, elevation or slope
A_s	Standing snow cover area (km^2) based on either of terrain aspect, elevation or slope
$A_{layover}$	Layover area (km^2) based on either of terrain aspect, elevation or slope
A_{forest}	Forest area (km^2) based on either of terrain aspect, elevation or slope
$A_{\mathrm{Z}i}$	Scattering type area (km^2) based on either of terrain aspect, elevation or slope where, $\mathrm{Z}i$, $\forall i \in$ [1, 9], denote the nine different scattering classes obtained from the H-α space
A_{total}	Total area (km^2) of a particular aspect, elevation or slope
μ_{A_f}	Mean FSD (cm) of A_f
μ_{A_s}	Mean SSD (cm) of A_s
$B_\perp$	Perpendicular baseline (m)
$h_{2\pi}$	Ambiguity height (m)
$h'_{2\pi}$	Scaled ambiguity height (m)
Δf_{DC}	Doppler centroid frequency difference (Hz)

ACKNOWLEDGEMENTS

During this research phase, I have received substantial support from my supervisors, mentors, friends, and family. I would like to take this opportunity to thank each one of them.

First of all, this work would not have been possible without the constant guidance from my MSc thesis supervisors. I remember the time when I first selected this research topic, and it was Dr. Praveen K. Thakur who made me believe that despite significant research challenges, with proper motivation and effort, I can successfully achieve my objectives. Later, when I was at ITC, Dr. Ling Chang helped me to grasp several underlying concepts of the techniques incorporated in the research workflow. Since then, through this entire research period, she has helped to improve my conceptual, critical thinking, and scientific writing abilities, for which I am extremely grateful. In addition, I would like to convey my sincere gratitude to Mr. Shashi Kumar who provided me with valuable advice for appropriately carrying out this work. Moreover, I am really fortunate to officially conduct fieldwork in my study area situated in the northwestern Himalayas, for which I would like to thank again Dr. Praveen K. Thakur, who has stood beside me through this tedious but exciting MSc thesis phase.

Next, I would like to thank all my peers who in their busy MSc thesis schedule took the time to help me out whenever necessary. In particular, I really appreciate the efforts made by Mr. Abhisek Maiti, Mr. Shashwat Shukla, and Mr. Raktim Ghosh to help me critically understand several mathematical jargons, which otherwise would have been quite difficult to solve all by myself. Moreover, I am grateful to my field collaborators and friends, Mr. Rajeev Ranjan, and Mr. Sachchidanand Singh, who helped me a lot during my field visit. Also, thanks to my good friend Mr. Manasij Mukherjee, from my undergraduate days, who motivated me to join the Linux community back in 2013 and learn about Git.

Furthermore, I would like to sincerely thank Dr. Sameer Saran and Dr. V.A. Tolpekin, who being the IIRS-ITC JEP course director and coordinator respectively, have supported me from the beginning of this course. Also, I am grateful to other IIRS and ITC faculty members, especially Mr. Prasun Kumar Gupta and Dr. F.B. Osei, whose mentorship enabled me to overcome several conceptual barriers.

Finally, I would like to express my heartfelt gratitude to my father, Mr. Suranjan Majumdar, and uncle, Mr. Anjan Majumdar, without whom it would not have been possible for me to enrol in this prestigious IIRS-ITC JEP. Thanks for all the financial freedom that you have given me. Also, I am thankful to my dearest cousin, Mr. Anirban Majumdar, who helped me to remain optimistic during tiresome situations. Moreover, I would like to thank Mr. Biswanath Chakraborty and Dr. Asoke Nath, under whose guidance I have substantially improved my programming skills over the past decade. Last but not the least, I owe my greatest thanks to my late grandmother (1935-2013), Mrs. Iva Majumdar, who looked after me since my childhood days— sorry 'dida' for all those troubles I put you through and hope that I have kept up to all your promises.

Apart from this, I would like to thank the Deutsches Zentrum für Luft- und Raumfahrt (DLR) for providing the free TerraSAR-X TanDEM-X datasets without which this research would never have been possible. Also, this research is part of the broader ISRO EOAM, and ALOS RA-4 funded project, so I am really grateful to ISRO for working on such a challenging and enticing research theme. Lastly, I would like to thank the entire open-source software community, NASA, ESA, SASE, IIRS, and ITC for providing all the necessary resources required towards the successful completion of this MSc thesis.

TABLE OF CONTENTS

LIST OF FIGURES

LIST OF TABLES

1. INTRODUCTION

1.1. Motivation

The estimation of snow depth (SD) and snow water equivalent (SWE) using Polarimetric Synthetic Aperture Radar (PolSAR), Interferometric SAR (InSAR) and Polarimetric SAR Interferometry (Pol-InSAR) is feasible but challenging. In this work, existing approaches are to be improved or customised for optimally estimating and evaluating SD and SWE over the rugged terrains of the Beas river watershed, near Manali, India.

1.2. Background

The cryosphere collectively represents the regions of the Earth where water is prevalent in its solid form, either permanently (annually) or temporarily (seasonally). These include the polar ice caps, and the snow covered mountainous areas, all of which significantly contribute to the global climate system change. Evidently, snow is the second most extensive component of the cryosphere after frozen ground having maximum and mean cover extents of approximately 47 million sq. km (in January) and 26 million sq. km respectively (Barry & Gan, 2011). As a result, the frequent large-scale monitoring of snow is central to implementing environmental policies, for which remote sensing is the only way forward (Tedesco, 2015).

Snow depth and snow water equivalent constitute two of the most important physical properties of snow and are extensively used in hydrological models that relate to snowmelt runoff and snow avalanche predictions (Thakur et al., 2017). While snow depth or snow height refers to the distance of the ground to the snow surface, SWE quantifies the amount of water present in a snowpack (layered snow formed by accumulation over time). Theoretically, SWE is defined as the product of snow depth and snow density and can be conceptualised as the amount of liquid water obtained owing to the instantaneous melting of an entire snowpack (Tedesco, 2015). The accurate estimation of these two parameters is quite challenging depending upon the data availability and variety, mathematical model selection, and the hydrometeorological conditions of the area of interest. Hence, it is considered to be an important research element in the cryosphere paradigm (Leinss, Parrella, & Hajnsek, 2014; Leinss, Wiesmann, Lemmetyinen, & Hajnsek, 2015).

Due to the difficulties posed by in-situ or ground based measurements of snow depth and SWE in rugged terrains, remote sensing techniques coupled with adequately sampled (both in space and time domains) ground measurements are widely used to improve the quality of these estimated parameters over considerably large areas (Takala et al., 2011). Currently, LiDAR (Light Detection and Ranging) and spaceborne SAR are the most popular techniques used in the studies related to snow, ice and the cryosphere in general (Deems, Painter, & Finnegan, 2013; Leinss et al., 2014; Tedesco, 2015). However, LiDAR can only be used to determine the height of the snow and cannot be used for measuring other physical properties such as snow density and snow wetness. In addition, the operating cost of LiDAR is sufficiently high and is also weather dependent (Deems et al., 2013). As a result, spaceborne SAR systems benefit from substantial coverage (globally available), cloud insensitivity, night-time operability and are extensively used to measure the snow physical properties sufficiently at high spatial resolutions (Moreira et al., 2013; Thakur et al., 2012).

The applicability of SAR systems for snow cover monitoring was discussed as early as 1977 (Ulaby, Stiles, Dellwig, & Hanson, 1977) wherein the snow backscatter coefficient was measured and was thereafter modelled for various frequencies, layers, and polarisations (Zuniga, Habashy, & Kong, 1979). It was shown that only very high microwave frequencies (Ku-band or higher) exhibit a significant dependence on SD or the SWE of dry or standing (deposited) snow (Yueh et al., 2009). However, lower frequencies (X-band or below) penetrate through dry snow whereby the underneath frozen soil or ground primarily contributes to the radar backscatter signal. On the other hand, in case of moist snow (the transitional stage between dry and wet snow) and wet snow, the predominant scattering occurs from the snow volume and snow surface respectively due to the presence of water. Essentially, water, with its high dielectric constant, heavily modifies the dielectric properties of snow and effectively reduces the snow penetration capacity of the radar pulses (Abe, Yamaguchi, & Sengoku, 1990). The radar backscattering mechanism for a typical snow covered area can be conceptualised from Figure 1. In principle, PolSAR and InSAR systems utilise these received target echoes for supporting various microwave remote sensing applications in the cryosphere domain.

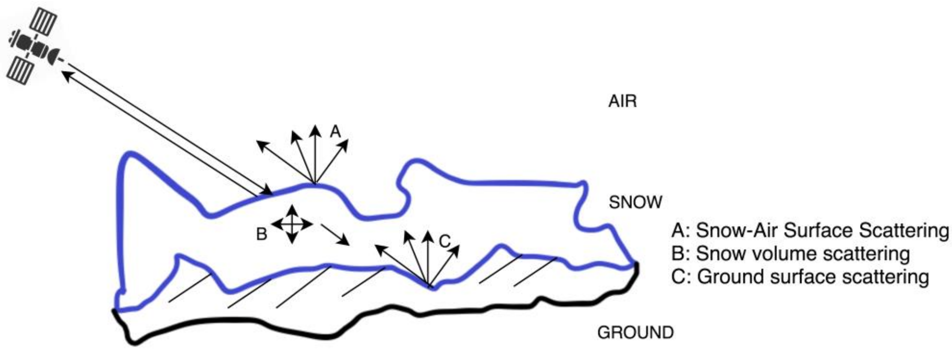

Figure 1: Conceptual diagram displaying the radar backscattering mechanism in hilly terrains. Adapted from Thakur et al. (2012).

A polarimetric SAR system utilises the polarised radar echoes to obtain information about the specific scattering mechanism for a particular target. In essence, by using a coherent analysis which incorporates the phase of different polarimetric channels, it is possible to differentiate various scattering mechanisms (Lee & Pottier, 2009). Nowadays, PolSAR based algorithms that work on the polarimetric backscatter signal have been widely adopted for various snow related applications such as the classification of dry and wet snow, measuring snow wetness and snow density (Singh et al., 2017; Snehmani, Venkataraman, Nigam, & Singh, 2010; Thakur et al., 2017, 2012; Usami, Muhuri, Bhattacharya, & Hirose, 2016). In this context, the roll-invariant entropy-anisotropy-alpha (H-A-α) decomposition and Wishart classification have been successfully tested to classify different snow types as well as demarcate snow covered areas (Cloude, 2010; Lee & Pottier, 2009; Singh, Venkataraman, Yamaguchi, & Park, 2014). Recently, the use of spaceborne PolSAR for snow height determination has been introduced, wherein the relationship between the copolar phase difference (CPD) and fresh snow depth (FSD) is quantitatively analysed by deriving a theoretical model (Leinss et al., 2014). However, the major challenge in this approach lies in accurately modelling the anisotropic effective permittivity of dry snow which is dependent on the depolarisation factor (calculated by fixing the shape of the ice grain) and ice grains' volume fraction (measured using snow density).

Interferometric SAR techniques find significant usage in the cryosphere domain and have been used to construct highly accurate digital elevation models (DEMs), measure dry snow depth and SWE in several studies (Guneriussen, Høgda, Johnsen, & Lauknes, 2001; Lei, Siqueira, & Treuhaft, 2016; Leinss et al., 2015; Li, Wang, He, & Man, 2017; Liu, Li, Yang, Chen, & Hao, 2017). The principle of SAR interferometry builds upon measured phase differences between radar images of the same area acquired at different temporal instances (repeat-pass) (Massonnet & Feigl, 1998) or different viewing geometries but same epoch (single-pass) (Budillon, Pascazio, & Schirinzi, 2008). Still, the inherent problems of spatial and temporal decorrelations and atmospheric inhomogeneities are the primary limiting factors in the studies involving InSAR and its variant D-InSAR (Differential InSAR) (Pepe & Calò, 2017). While spatial decorrelation is caused by large perpendicular baselines (Pepe & Calò, 2017), the problem of temporal decorrelation arises due to the change in the surface over time (Leinss et al., 2018, 2015). Moreover, the atmospheric noise occurs owing to the variation in the water vapour distribution in the atmosphere (Hanssen, 2001). These factors are responsible for inaccurate and low-coherence measurements, thereby leading to a potential decrease in the accuracy of the final results. In cryosphere research, the loss of coherence in InSAR is heavily influenced by the snow humidity, melting, and refreezing and is also susceptible to the variations in both spatial and temporal baselines. Although data assimilation algorithms like 3DVAR (three dimensional variation) and EnKF (Ensemble Kalman Filter) have been applied to the produced outputs of the SD inversion models for minimizing the effect of temporal decorrelation, the applicability and feasibility of such algorithms remains untested on varying data sets and study areas (Liu et al., 2017).

The Pol-InSAR technique works on the coherent combination of both PolSAR and InSAR observations, thereby enabling the interferogram generation in arbitrary transmit and receive channels (Cloude, 2005, 2010). It has been widely used for estimating tree height in forested regions and can be effectively applied to natural or artificial volume scatterers including snow and ice (Hajnsek, Kugler, Lee, & Papathanassiou, 2009; Kugler, Lee, Hajnsek, & Papathanassiou, 2015; S. Kumar, Khati, Chandola, Agrawal, & Kushwaha, 2017; Papathanassiou & Cloude, 2001). In essence, the identification of different scattering processes (PolSAR) and the vertical profile sensitivity (InSAR) are unique to this technique. Therefore, the applicability of Pol-InSAR based SD retrieval could prove its potential in case of the standing snow depth (SSD) (Negi, Kulkarni, & Semwal, 2009; Thakur et al., 2017, 2012).

1.3. Problem Statement

The selected study area (Manali, India) is characterised by steep slopes and forests. As a result, the SAR images acquired over this region will be affected by speckle and geometric distortions caused by layover, foreshortening and shadowing (Thakur et al., 2017, 2012). Consequently, the estimated values in these distorted regions will be highly susceptible to error. Another closely associated issue in this context is the evaluation of the SD and SWE results. Due to the rugged topography and possible unavailability of suitable instruments, conducting in-situ measurements may be difficult. Thus, in the absence of such data, ensuring the quality of the computed results is also challenging. So, uncertainty assessment constitutes a fundamental problem in this research work.

In addition, the snow depth inversion model for estimating FSD takes the ice volume fraction and depolarisation factor as inputs along with the CPD. Although the computation of CPD is relatively simple, a significant effort needs to be put into deciding the shape of the ice grains such as oblate, prolate and spherical for accurately computing the depolarisation factor. Also, prior knowledge about snow density is required for calculating the ice volume fraction and SWE (Leinss et al., 2014, 2015).

Regarding the interferometric processing, the key concern is to minimise the loss of coherence occurring mainly due to the spatial and temporal decorrelations. So while creating a DEM, optimal spatio-temporal baselines need to be chosen for reducing the height ambiguity, which could be challenging depending on the available datasets. Moreover, the precise coregistration of the master and slave images is also crucial for both InSAR and Pol-InSAR, and hence, careful selection of the coregistration parameters is extremely important (Guneriussen et al., 2001; Hanssen, 2001; Leinss et al., 2015; Li et al., 2017). Also, the choice of applying phase filtering should be carefully considered as it is a compromise between noise reduction and fringe continuity preservation (Mestre-Quereda, Lopez-Sanchez, Selva, & Gonzalez, 2018).

In the case of the Pol-InSAR approach, the vertical wavenumber is an essential factor for scaling the snow depth values. However, for single-pass interferometric data, the wavenumber is generally quite small and needs to be simulated or scaled for accurate vertical profile retrieval (Hajnsek et al., 2009; Kugler et al., 2015). Additionally, there is a requirement for applying proper filtering steps, and hence, sufficient sensitivity analysis (SA) needs to be carried out for the free parameters.

1.4. Research Identification

The prime focus of this research is to estimate the FSD and SSD using PolSAR and Pol-InSAR respectively. In addition, the snow water equivalent needs to be determined, for which the snow density needs to be known. Essentially, the study will involve uncertainty assessment of the computed SD and SWE for providing a quantitative quality measure to the end users.

1.4.1. Research Objectives

The specific research objectives are stated as follows:

1) Estimating FSD using the copolar phase difference method.
2) Measuring SSD using Pol-InSAR.
3) Estimating SWE of fresh snow and standing snow.
4) Performing uncertainty assessment and sensitivity analysis of the computed results.

1.4.2. Research Questions

1) Is it possible to prepare an accurate DEM for improving the snow depth and snow water equivalent estimates?
2) <u>Specific Objective 1:</u>
    a. What type of ice grain shape should be considered for calculating the depolarisation factor?
    b. What should be an appropriate axial ratio for a fresh snow particle?
    c. How to calculate the ice grains' volume fraction using snow density?
3) <u>Specific Objectives 2:</u>
    a. Which Pol-InSAR height inversion model should be chosen?
    b. How to optimise the free parameters for accurate snow height retrieval?
    c. What type of filters should be applied?
4) <u>Specific Objective 4:</u>
    a. How to perform uncertainty assessment and sensitivity analysis?
5) How to validate the SD and SWE results?
6) What should be the optimal filter window (kernel) size for reducing noise in the obtained results?

1.5. Innovation

In this research, a first-time effort has been made to estimate the fresh snow depth using SAR remote sensing in the presence of complex hydrometeorological and topographical situations. This is carried out using the polarimetric CPD method developed by Leinss et al. (2014). Subsequently, the fresh snow water equivalent (FSWE) is also measured using a fixed snow density value for the entire study area.

Another major innovative aspect of this work is the estimation of deposited or standing snow depth using Pol-InSAR based height inversion. Previously, this technique has resulted in successful tree height retrieval from the volume decorrelation effects observed in the forested areas. Till date, some studies have measured the Pol-InSAR signatures for different microwave wavelengths and also the penetration depth in case of glacial ice (Hoen & Zebker, 2000; Sharma, Hajnsek, Papathanassiou, & Moreira, 2013). Thus, the computation of SSD and the corresponding standing SWE (SSWE) in the presence of significant uncertainty sources is unique to this work. Finally, the SSD and FSD are compared along with the respective SWEs which also constitutes the novelty of this thesis.

1.6. Thesis Outline

This thesis is compartmentalised into seven chapters each consisting of several sub-chapters. It starts with an introductory discussion in Chapter 1 following which the relevant studies and their theoretical background are described in Chapter 2. Thereafter, the study area is specified in Chapter 3. From Chapter 4 onwards the methodology and results are discussed. Finally, the answers to the aforementioned research questions are explicitly mentioned in Chapter 6 after which the conclusions and recommendations are put forward in Chapter 7. Apart from this, three appendix chapters have been provided for additional information related to SAR and other methodological aspects which have been briefly put in the main content.

2. LITERATURE REVIEW

This chapter deals with state of the art SAR approaches in the context of cryosphere research with particular emphasis on snow depth and snow water equivalent. At first, a general overview of the electromagnetic (EM) properties of snow is provided in section 2.1 for coherently guiding the reader through this chapter. Thereafter, an in-depth discussion is put forward about SAR specific literatures concerning the estimation of SD and SWE in section 2.2.

2.1. Electromagnetic Properties of Snow

Most remote sensing based applications are built upon the theories of the interaction of the EM wave and matter, with the exceptions being those which rely on gravimetric measurements (Tedesco, 2015). The characteristics of snow in the visible/near-infrared and microwave regions are briefly reviewed in this section. Noted that since microwave remote sensing of snow is the primary topic of concern in this thesis, the relevant optical remote sensing concepts are succinctly mentioned.

2.1.1. Snow Reflectance in the Visible/Near-Infrared and Thermal Infrared Regions

Freshly fallen snow appears brighter to the human eye as compared to the metamorphic snow such as firn and depth hoar. This is due to its high and relatively flat spectral reflectance values across the entire visible EM spectrum (Figure 2). Moreover, the spectral reflectance values are indirectly proportional to the snow/ice grain size. In essence, by having the least grain size, fresh snow exhibits the highest albedo (sometimes more than 90%) whereas for metamorphosed and dirty snow it is usually in the range of 20-40%. Additionally, the presence of liquid water within the snowpack indirectly affects the albedo as it results in grain size growth and subsequent recrystallisation and metamorphosis (Tedesco, 2015).

Figure 2 shows the reflectance peaks occur between 400 and 600 nm (visible portion) and close to 800 nm in the near-infrared (NIR). However, in the thermal infrared (3 μm – 100 μm) and higher wavelength regions of the EM spectrum, the snow reflectance is quite low. Also, the thermal emissivity of snow lies in the range of 0.965 to 0.995 with the maximum being at 10 μm (Tedesco, 2015).

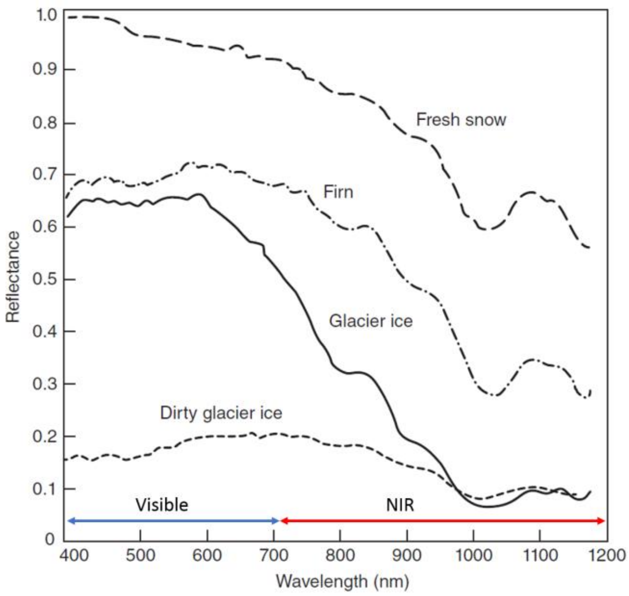

Figure 2: Spectral reflectance curves in the visible and NIR regions for different snow and ice surfaces. Adapted from Tedesco (2015).

2.1.2. Microwave Region

Microwaves play a substantial role in the cryosphere research domain because they can pass through the Earth's atmosphere almost without any obstruction and can significantly interact with the snowpack volume. Due to the porous structure of snow, which in effect, is composed of three material phases— air, ice and water, the interaction of microwaves occur with all these constituent phases (Leinss, 2015; Petrenko & Whitworth, 2002). Essentially, the microscopic structure of snow can be characterised based on the microwave wavelength, for which the dielectric properties of air, ice and water need to be considered along with other features of the snow medium (Leinss, 2015).

Dielectric Properties of Air, Ice and Water

Due to the significant water vapour content in the atmosphere, the microwave absorption owing to the water vapour saturated air in a snowpack of few meters depth is negligible. Accordingly, the relative permittivity of water vapour saturated air in snow (ϵ_{air}) has been calculated to be about 1.00059 (Bryan & Sanders, 1928).

In the case of ice, a solid state body, the imaginary part of the complex permittivity as shown in Eq. (1), is quite small and hence, radio waves below 1 GHz have large penetration, from several hundred metres to even kilometres. However, the penetrating capacity of the radio wave decreases with increasing frequency (about 1 m at 20 GHz) (Warren & Brandt, 2008). It has also been found that with increasing temperature, there is a slight increase in the real and imaginary parts of the dielectric permittivity (Matzler & Wegmuller, 1987). Furthermore, this real part ($\Re(\epsilon_{ice}) = 3.179$) has almost no frequency dependence between 10 MHz and 100 GHz, and for measuring seasonal snow properties using microwave remote sensing, the imaginary part can be neglected (Bohleber, Wagner, & Eisen, 2012; Leinss, 2015; Warren & Brandt, 2008).

$$\epsilon_{ice} = \Re(\epsilon_{ice}) - j\Im(\epsilon_{ice}) \tag{1}$$

where, ϵ_{ice}, $\Re(\epsilon_{ice})$, and $\Im(\epsilon_{ice})$ are the complex permittivity, relative permittivity (based on vacuum as unity) and the relative loss factor of ice respectively with j being the imaginary unit, and the negative sign is appearing as snow is a lossy dielectric medium (Evans, 1965).

Liquid water, on the other hand, is responsible for strong microwave absorption in snow and its relative permittivity is calculated based on the Debye relaxation peak. For water at 0°C, this peak is located at approximately 10 GHz, i.e., at the centre of the radio window. As a result, the relative permittivity (ϵ_{water}) varies greatly with the change in microwave frequencies, from $\epsilon_{water} < 5$ (about 100 GHz) to $\epsilon_{water} \approx 87$ (below 10 GHz) (Buchner, Barthel, & Stauber, 1999; Ellison, Lamkaouchi, & Moreau, 1996).

Spatial Distribution and Length Scales of Snow

The three constituent phases of snow (air, ice and water) exhibit spatial distribution across many length scales, the smallest being the crystal edges of dendritic snow crystals having length scales in the order of micrometres or below (Leinss, 2015). While single ice grains in the snowpack display length scales in the range of a few tens of micrometres to a few millimetres, the depth of an entire snowpack can vary from meters to several kilometres and is strongly dependent on the topography (Deems, Fassnacht, & Elder, 2006; Mätzler, 2002; Sturm & Benson, 2004). Such multi-scale variation of the snow properties is primarily governed by the snow accumulation, metamorphosis, and ablation processes (Deems et al., 2006). Hence, in order to understand and describe the interaction between microwave and snow, all the relevant scales need to be assessed. In fact, for remote sensing systems, it is actually the resolution of the observing sensor that defines these length scales (Leinss, 2015).

Snow as a Homogeneous and Effective Medium

When the length scale of snow is much smaller than the incident microwave wavelength (λ_0), then the snowpack can be modelled as a non-scattering homogeneous medium having an effective (or complex) permittivity ϵ_{snow}. In such a case, the interference pattern resulting from the entire ensemble of scatterers (each having length d) present in a cube of length λ_0 needs to be considered to theoretically understand this non-scattering mechanism. Since $d \ll \lambda_0$, the scattering characteristics of all the $(\lambda_0/d)^3$ scatterers can be described with the help of Rayleigh scattering. A more detailed description in this regard is provided by Leinss (2015).

Snow as a Heterogeneous Medium

Snow can also act as a heterogeneous medium composed of small ($\lambda_0 \approx 10d$) or large ($\lambda_0 \approx d$) ice grains. For both these scenarios, the assumption of a non-scattering medium does not hold, and the scattering effects must be taken into account (Leinss, 2015).

In the first case, the Rayleigh scattering can again be applied to describe the scattering characteristics of the medium. The relatively larger ice grains scatter the microwave radiation more strongly owing to the higher dependence on the radar cross-section. This eventually leads to volume scattering which takes place because of the constructive interference in all directions. Thus, the ice grain size is a significant factor for the occurrence of volume scattering within the snowpack (Tsang et al., 2007).

When the ice grain size is comparable to the wavelength (for frequencies higher than 100 GHz), Mie scattering is used to describe the scattering mechanism instead of Rayleigh scattering. However, due to multiple scattering, the propagation direction and coherence of the incident wave cannot be recovered and as such are entirely lost (Hallikainen, Ulaby, & Van Deventer, 1987; Tsang et al., 2007).

Snow Anisotropy

Initially, the accumulated fresh snow (after snowfall) exhibits a random isotropic structure where the ice and snow inclusions are smaller than the operating wavelength of the X-band. Thereafter, the snow settling takes place by which the fresh snow is compressed by its weight. As a result, the previous randomly oriented microstructure gradually transforms into an anisotropic medium consisting of horizontally aligned snow particles. Eventually, these horizontally shaped particles undergo further metamorphosis to form isotropic structures, and finally, weeks later, depth hoar (occurs at the base of a snowpack) and firn (granular snow) are formed which display vertically aligned structures. The entire chain of processes that govern this snow metamorphosis process has been experimentally evaluated using X-ray computer tomography (CT) scans (Riche, Montagnat, & Schneebeli, 2013). A simplistic conceptual diagram is provided (Figure 3) to understand this transformation process clearly.

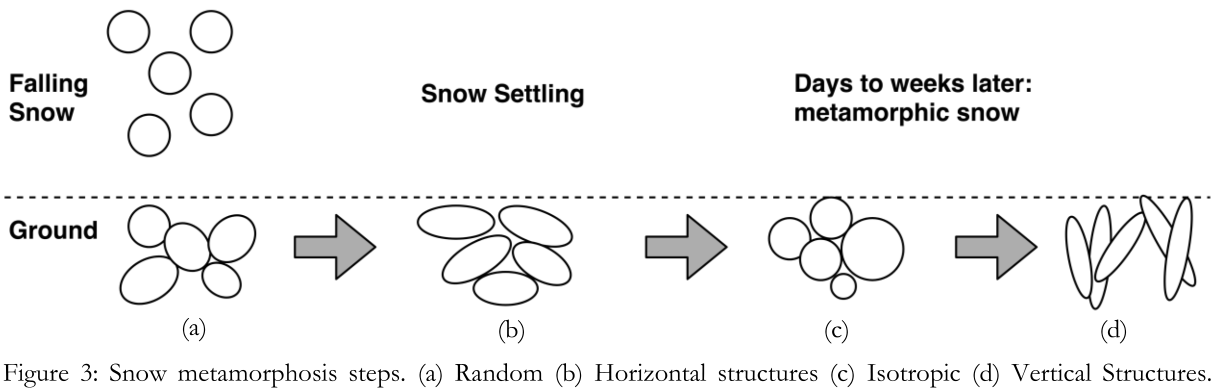

Figure 3: Snow metamorphosis steps. (a) Random (b) Horizontal structures (c) Isotropic (d) Vertical Structures. Adapted from Leinss et al. (2014).

Snow as a Multilayered Structure

A snowpack is formed from layers of snow that have accumulated over time. So when the microwave interaction of snow is concerned, the respective measurements need to be conducted for different layers displaying varying physical properties of snow and consequently, different refractive indices (Leinss et al., 2014). In this case, multilayer and multiple-scattering radiative transfer models have been applied for obtaining reliable simulation results related to snow microwave emission and backscattering (Mätzler & Wiesmann, 1999; Picard, Sandells, & Löwe, 2018; Royer et al., 2017; Tuzet et al., 2017).

Speckle Formation by the Snowpack

Although plane wavefronts propagating through homogeneous media are not distorted, in the context of snow as an effective homogeneous medium, it has been observed that the wavefronts get significantly deteriorated due to the snow-ground surface and snow-air surface scatterings (Figure 1). These plane wavefronts are also affected by the varying densities and volume scattering within a snowpack. In essence, the interference of these distorted wavefronts results in a randomly distributed intensity pattern called speckle, which is a common phenomenon for all scattering surfaces (particularly the rough ones) which interact with coherent EM waves such as SAR and LiDAR (Goodman, 2007; Leinss, 2015).

Due to the inherently spatial nature of speckle, the backscattered signal undergoes heavy spatial modulation, and as a result, suitable spatial averaging is an essential factor that needs to be incorporated for obtaining statistically significant measurements. Moreover, for snow related studies which rely on the phase information of the backscattered signal, large temporal changes in the snow surface (caused by wind drift, snow depth and density variations) lead to strong decorrelations in the phase and the speckle patterns, thereby posing difficulty in obtaining results with sufficient quality (Leinss, 2015).

2.2. Estimation of Physical Snowpack Parameters using SAR

SAR based remote sensing applications have grown tremendously in the past few decades as they provide unique weather independent day-night imaging facility across the globe (Moreira et al., 2013). Naturally, a substantial amount of cryospheric research activities have been conducted using SAR imagery (Dierking, 2013; Leinss, 2015; Leinss et al., 2018; Singh et al., 2017; Winsvold et al., 2018). Since the primary focus of this thesis lies in estimating SD and SWE using spaceborne PolSAR and Pol-InSAR techniques, the relevant literatures which have been studied during the thesis period are summarised in this section.

2.2.1. Snow Depth Measurement

Snow depth measurement is still a challenging topic in the remote sensing domain due to numerous uncertainty sources such as the topography induced snow density and microstructure variations (Leinss et al., 2014). However, significant efforts have been made to minimise these uncertainties, thereby achieving sufficiently accurate site-specific snow depth results. In the context of snow depth retrieval using SAR, the research works have mainly emphasised on estimating dry snow depth (DSD) (Esmaeily-Gazkohani, Granberg, & Gwyn, 2010; Li et al., 2017; Liu et al., 2017), however, there have been recent studies on fresh and wet snow depth measurements (Leinss et al., 2018, 2014). Additionally, the well-known Pol-InSAR based tree height inversion algorithms are also applicable for SSD estimation (Leinss et al., 2014).

Fresh Snow Depth

The estimation of fresh snow depth using X-band SAR polarimetry has been recently introduced by Leinss et al. (2014). In this work, a theoretical relationship has been derived based on the CPD between VV and HH polarisations. According to the PolSAR theory (Lee & Pottier, 2009), three primary scattering mechanisms can be classified with CPD (ϕ_{CPD})— surface ($\phi_{CPD} = 0$), dihedral ($\phi_{CPD} = \pi$) and volume scattering (ϕ_{CPD} is uniformly distributed between $-\pi$ and π) wherein ϕ_{CPD} is defined as follows:

$$\phi_{CPD} = \phi_{VV} - \phi_{HH} = \left\langle \tan^{-1}\left(\frac{\Im(S_{VV})}{\Re(S_{VV})}\right) - \tan^{-1}\left(\frac{\Im(S_{HH})}{\Re(S_{HH})}\right)\right\rangle, \phi_{CPD} \in [-\pi, \pi] \tag{2}$$

In Eq. (2), it can be seen that ϕ_{CPD} is simply the ensemble average (denoted by the $\langle \dots \rangle$ operator) of the phase difference between the two copolarised channels VV and HH. Here, $\Im$ and $\Re$ denote the imaginary and real parts of the complex scattering matrices S_{VV} and S_{HH} respectively. Moreover, the opposite sign convention ($\phi_{CPD} = \phi_{HH} - \phi_{VV}$), a common notation in some texts (Haldar, Rana, Yadav, Hooda, & Chakraborty, 2016), is not used so as to ensure the positive phase difference for fresh snow. Additionally, when an arbitrary target is considered, ϕ_{CPD} contains the superimposed information about all these three scatterings. Also, the co-cross-polar phase differences (e.g., $\phi_{VV} - \phi_{VH}$) are inapplicable because they fail to describe a target (such as snow) having a dielectrically anisotropic microstructure (Leinss et al., 2014).

ϕ_{CPD} can be alternatively defined as the phase angle of the complex copolar coherence, $\tilde{\gamma_c}$ (since γ is the standard notation for coherence amplitude, $\tilde{\gamma}$ is used for the complex coherence), defined in Eq. (3). In this case, the copolar coherence amplitude ($\gamma_c = |\tilde{\gamma_c}|$) is a measure of the radar backscattering mechanism where low values close to zero (ideally $\gamma_c = 0$) indicate the presence of volume scattering and high values (ideally $\gamma_c = 1$) represent surface scattering (Lee & Pottier, 2009; Leinss et al., 2014; Singh et al., 2014).

$$\tilde{\gamma_c} = \frac{\langle S_{VV} S_{HH}^* \rangle}{\sqrt{\langle S_{VV} S_{VV}^* \rangle \langle S_{HH} S_{HH}^* \rangle}} = \gamma_c e^{j\phi_{CPD}}, \gamma_c \in [0, 1] \tag{3}$$

In order to model this snow anisotropy, an ice particle needs to be associated with a specific shape. It has been observed that fresh snow and old snow exhibit horizontally aligned (oblate) and vertically aligned (prolate) spheroidal structures respectively (Leinss et al., 2014). Moreover, a shape parameter, known as the depolarisation factor, also has to be considered in this context (Leinss et al., 2014; Sihvola, 1999). In principle, a single spheroidal particle is characterised by three dipoles corresponding to the three orthogonal axes (a_x, a_y, and a_z) represented using a 3D (x, y, z) Cartesian coordinate system. This is depicted in Figure 4, where the prolate shaped ice grain is linked with the radar reference frame (h, k, v) following the radar backscattering alignment (BSA) convention, k being the propagation vector, h and v are the wave components of the horizontal and vertical polarisations respectively. Also, θ is the mean incidence angle with respect to the surface normal (Leinss et al., 2014; Parrella, Hajnsek, & Papathanassiou, 2013).

So, by fixing a particle shape, the three depolarisation factors, N_i ($\forall i \in \{x, y, z\}$), can be obtained by solving the surface integral (s is the ellipsoidal surface) as shown in Eq. (4).

$$N_i = \frac{a_x a_y a_z}{2} \int_0^{\infty} \frac{ds}{(s + a_i^2)\sqrt{(s + a_x^2)(s + a_y^2)(s + a_z^2)}} \tag{4}$$

$$\text{where, } N_x + N_y + N_z = 1$$

For a perfectly spherical shape, all three depolarisation factors are equal to $1/3$. The two other special cases include disk (1, 0, 0) and needle (0, 1/2, 1/2). In cases of prolate and oblate spheroids, the closed form expressions are already available as shown in Eq. (5) (Sihvola, 1999). Here, the shape is dependent on the axial ratio (a_x/a_z) which is used for calculating the prolate eccentricity, $e_1 = \sqrt{1 - (a_x/a_z)^2}$, and oblate eccentricity, $e_2 = \sqrt{(a_x/a_z)^2 - 1}$ respectively, i.e., for prolate, $a_x/a_z < 1$, whereas for oblate, it is the reverse. However, for general ellipsoids having different axes, the above surface integration needs to be explicitly solved.

$$N_z = \begin{cases} \frac{1 - e_1^2}{2e_1^3}\left(\ln\frac{1 + e_1}{1 - e_1} - 2e_1\right), & a_z > a_x = a_y \\ \frac{1 + e_2^2}{e_2^3}(e_2 - \tan^{-1} e_2) \quad , & a_z < a_x = a_y \end{cases} \tag{5}$$

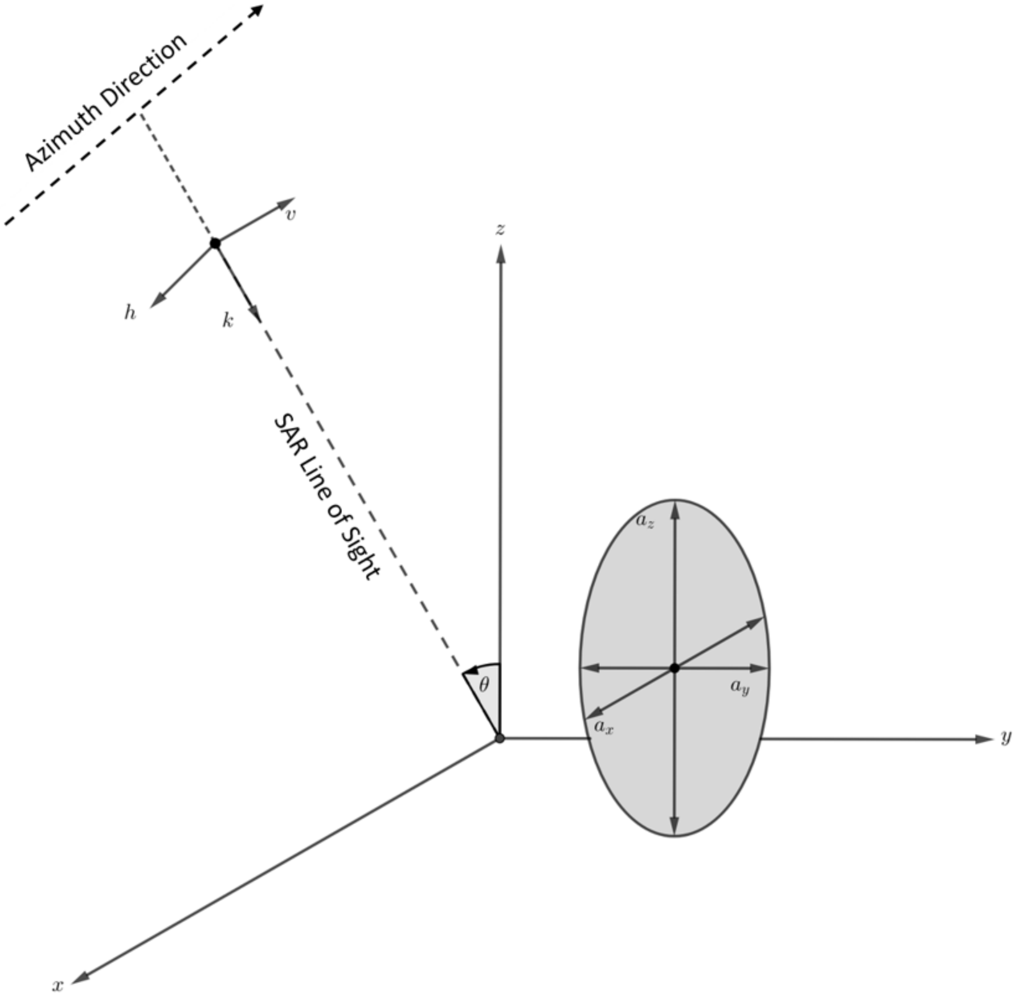

Figure 4: Orientation of a single prolate ice particle linked with the radar reference frame. Adapted from Leinss et al. (2014).

Evidently, the Maxwell-Garnett theory related to electromagnetic mixing models can be applied to a medium consisting of both air and ice as in the case of snow. Therefore, the effective permittivity of this mixed medium, $\epsilon_{eff,i}$, is anisotropic and is given by Eq. (6) (Leinss et al., 2014; Sihvola, 1999). Here, the particle volume fraction (f_{vol}) is dependent on the snow and ice densities ρ_{snow} and ρ_{ice} respectively.

$$\epsilon_{eff,i} = \epsilon_{air}\left[1 + f_{vol}\frac{\epsilon_{ice} - \epsilon_{air}}{\epsilon_{air} + (1 - f_{vol})N_i(\epsilon_{ice} - \epsilon_{air})}\right] \tag{6}$$

where, $f_{vol} = \frac{\rho_{snow}}{\rho_{ice}}$, $\rho_{ice} = 0.917\ \mathrm{g/cm^3}$, and $i \in \{x, y, z\}$

Furthermore, the refractive indices of this birefringent (or birefractive) medium, n_H and n_V corresponding to the HH and VV polarisations respectively, are dependent on this anisotropic effective permittivity (Leinss et al., 2014). In addition to this, since the snow anisotropy is assumed to be oriented along the Earth's gravitational field, n_H remains constant whereas n_V is dependent on the incidence angle θ as given by Eq. (7) (Leinss, 2015). Also, the imaginary part of the effective permittivity is negligible in the case of dry snow (fresh snow is also dry), and therefore, it is not used in the model developed by Leinss et al. (2014).

$$n_H^2 = \epsilon_{eff,x}$$
$$n_V^2 = \epsilon_{eff,y} \cos^2\theta + \epsilon_{eff,z} \sin^2\theta \tag{7}$$

where, $\epsilon_{eff,x}$, $\epsilon_{eff,y}$, and $\epsilon_{eff,z}$ represent the effective permittivities of fresh snow in x, y, and z directions of a 3D Cartesian co-ordinate system (Leinss et al., 2014).

Once all these aforementioned parameters are calculated, the CPD based inversion model which is given by Eq. (8), can be applied to estimate the depth of fresh snow, denoted by ΔZ_f (Leinss et al., 2014). In this equation, -1 is introduced as per the BSA convention which is followed for all radar systems. Here, λ_0 is the radar wavelength and $\Delta\zeta$ is the relative path length difference which is dependent on $\epsilon_{eff,i}$, θ, and ρ_{snow} (Leinss, 2015). Moreover, the horizontally aligned microstructure of fresh snow reduces the propagation speed for the HH channel and hence, in this case, $n_H > n_V$ always holds. However, for recrystallised snow having vertically aligned structures, the reverse condition is true (Leinss, 2015). One important fact in this regard is that, only side looking radar systems such as the real aperture radar (RAR) and SAR have the capability to measure the anisotropy of snow, whereas the usage of nadir looking ground penetrating radars (GPR) are impracticable to model this anisotropy (Leinss, 2015).

$$\Delta Z_f = (-1)\frac{\lambda_0 \phi_{CPD}}{4\pi\Delta\zeta} \tag{8}$$

where, $\Delta\zeta = \sqrt{n_V^2 - \sin^2\theta} - \sqrt{n_H^2 - \sin^2\theta}$, $\phi_{CPD} > 0$ and $n_H > n_V$

It should be noted that in their original work, Leinss et al. (2014) have excluded forested areas from the analysis using backscatter intensity thresholding. Furthermore, the CPD of the valid pixels solely contributing to the fresh snowfall events has been chosen after appropriate ground-truth surveys. Hence, suitable preprocessing steps need to be carried out before applying this model.

Dry Snow Depth

Dry snow refers to fresh, old, wind-compressed snow including depth hoar and firn and acts as a transparent medium for microwave frequencies up to about 10 GHz (Matzler, 1996). The term 'dry' is used because the temperature of such snow is below 0°C and hence, the moisture content is low (Leinss, 2015). In order to estimate the depth of dry snow, repeat-pass InSAR (rp-InSAR) is the standard technique which is currently in practice (Guneriussen et al., 2001; Li et al., 2017; Liu et al., 2017) since single pass interferometry (sp-InSAR) fails to detect dry snow (Leinss, 2015). The underlying principles of this approach in the context of DSD retrieval are described in the subsequent paragraphs.

In the case of dry snow as a homogeneous medium, the snow-ground surface is the primary source of the radar backscattering, and the volume scattering is generally neglected (Figure 1). However, in certain cases where the radar signal is able to penetrate several meters deep, such as the percolation zones of the Greenland ice sheets, volume scattering is predominant even for dry snow (Hoen & Zebker, 2000). As a result, the microwave interaction of snow is an essential component which needs to be investigated for estimating dry snow depth.

When a polarised microwave signal interacts with the snow-air surface, a significant phase shift occurs due to the change in the dielectric properties of the two media. This is depicted in Figure 5 which highlights the propagation path followed by the radar pulses during the snow-free and snow-covered periods. In this, the range distance for a non-moving target during the snow-free time is ΔR_s. However, in the presence of snow, the range distance for this particular target becomes $\Delta R_a + \Delta R_r$ owing to the refraction at the snow-air interface (θ_r is the refraction angle). Thus, the slant range difference (ΔR) is actually the difference between these two range distances corresponding to the snow and non-snow seasons (Guneriussen et al., 2001; Leinss, 2015; Li et al., 2017).

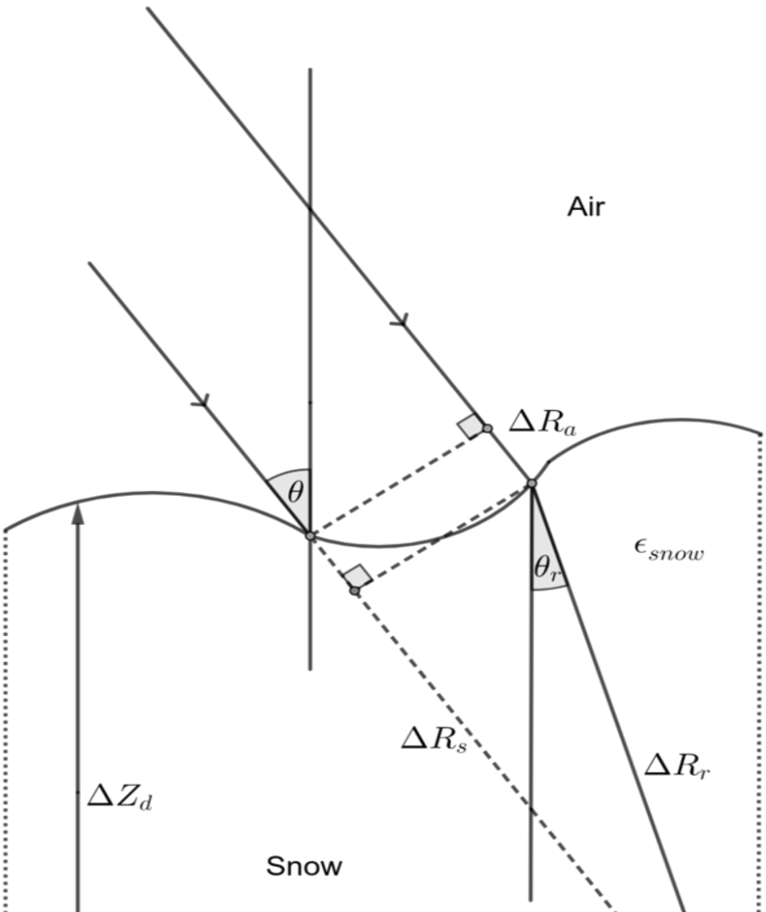

Figure 5: Geometry of microwave in snow. Adapted from Li et al. (2017).

Moreover, the real part of the effective permittivity of dry snow ($\Re(\epsilon_{snow})$) quantifies the backscatter signal delay and is composed of ϵ_{ice} and ϵ_{water}. In addition to this, it has been experimentally verified that $\Re(\epsilon_{snow})$ exhibits a slight non-linear dependency purely on the snow density (ρ_{snow}) in the range of 10 MHz and 100 GHz as shown in Eq. (9) (Bohleber et al., 2012; Leinss et al., 2015; Warren & Brandt, 2008).

$$\Re(\epsilon_{snow}) = \begin{cases} 1 + \alpha_s \rho_{snow} + \beta_s \rho_{snow}^3 & , \quad 0 < \rho_{snow} \leq 0.4 \text{ g/cm}^3 \\ \left[(1 - f_{vol})\epsilon_{air}^{\frac{1}{3}} + f_{vol}\epsilon_{ice}^{\frac{1}{3}}\right]^3 & , \quad \rho_{snow} > 0.4 \text{ g/cm}^3 \end{cases} \tag{9}$$

where, $\alpha_s = 1.5995 \text{ cm}^3/\text{g}$, and $\beta_s = 1.861 \text{ cm}^9/\text{g}^3$ are empirically derived constants (Leinss, 2015).

Apart from this, the volumetric water content (m_v) is a major factor responsible for the microwave absorption within the snowpack. The presence of liquid water significantly reduces the penetration capacity of the radar pulses, from several metres ($m_v = 0\%$) to a few centimetres ($m_v = 1\%$) at 16 GHz (Wiesmann & Mätzler, 1999). In this scenario, the total unwrapped (absolute) InSAR phase ($\phi_{total}^u \in \mathbb{R}$) is given by Eq. (10).

$$\phi_{total}^u = \phi_{atm}^u + \phi_{flat}^u + \phi_{topo}^u + \phi_{snow}^u + \phi_{noise}^u \tag{10}$$

where,

ϕ_{atm}^u : Phase contributed by the satellite orbital elevation, $\phi_{atm}^u \in \mathbb{R}$

ϕ_{flat}^u : Phase caused by the flat earth effect, $\phi_{flat}^u \in \mathbb{R}$

ϕ_{topo}^u : Topographical phase occurring due to terrain height, $\phi_{topo}^u \in \mathbb{R}$

ϕ_{snow}^u : Phase caused by snow depth, $\phi_{snow}^u \in \mathbb{R}$

ϕ_{noise}^u : Random phase noise, $\phi_{noise}^u \in \mathbb{R}$ (Hanssen, 2001)

u denotes the unwrapped (absolute) phase.

Accordingly, after subsequent removal of the other phases, ϕ_{snow}^u which represents the two-way propagation (with and without snow), can be mathematically defined in terms of the DSD (ΔZ_d), mean incidence angle (θ), $\Re(\epsilon_{snow})$ and the radar wavelength (λ_0) as given by Eq. (11) (Guneriussen et al., 2001; Leinss, 2015; Li et al., 2017; Liu et al., 2017).

$$\Delta Z_d = -\frac{\lambda_0 \phi_{snow}^u}{4\pi \Delta\xi}, \Delta\xi = \cos\theta - \sqrt{\Re(\epsilon_{snow}) - \sin^2\theta} \tag{11}$$

However, it should be noted that with InSAR, only relative snow depth can be measured. Furthermore, the estimated DSD is significantly affected by the complex correlation or coherence between the InSAR pairs. In essence, the low coherence regions which mostly arise from wet snow (temporal decorrelation) or forested areas (volume decorrelation) need to be masked out for accurate analysis purposes (Hoen & Zebker, 2000; Leinss, 2015; Li et al., 2017).

Wet Snow Depth

Although X-band sp-InSAR is a well-known technique for producing highly accurate DEMs, its applicability on snow depth estimation has been recently verified (Leinss et al., 2018). However, due to the high penetration depth in dry snow conditions, sp-InSAR can only be used to estimate wet snow depth (WSD). Essentially, wet snow having high water content absorbs the incoming microwave radiation, and thus only surface scattering takes place (Figure 1). In this regard, two approaches can be adopted for the WSD estimation.

One possible way to determine the WSD is to compute the radar penetration depth change owing to snow melt. The high transparency of dry snow at X-band and the low penetration depth in case of wet snow at the same frequency make it feasible to estimate the WSD. However, this technique poses a lot of difficulty as ensuring sufficient dryness and wetness of snow is quite challenging (Leinss, 2015).

Another approach is to compute the difference between the two DEMs— one acquired during the snow-free time and the other during the snow-covered season. This is known as the DEM differencing technique wherein the summer and winter season DEMs are compared (Leinss et al., 2018). Although straightforward, confirming that the reference summer time DEM is actually snow free and not acquired too early in the summer, may be difficult based on the study area. Otherwise, it could lead to the addition of a significant bias due to ice melting in late summer (Leinss, 2015; Leinss et al., 2018).

In order to apply either of the aforementioned techniques, the wet and dry snow types need to be segregated, for which straightforward but accurate radar backscattering and coherence based thresholding is sufficient. This is because wet snow exhibits low backscatter and low coherence, whereas dry snow displays significantly high backscattering and coherence values (Leinss et al., 2018). Moreover, additional mask layers which include forests, layover and shadow regions (in case of complex mountainous terrains) should be considered for subsequent analysis steps.

Standing Snow Depth

Standing or old snow refers to the deposited snow on the ground which has accumulated over time (Reynolds, 1983). Typically, old snow due to the presence of impurity and temperature-gradient induced recrystallisation process consists of snow particles larger than the microwave wavelength and results in volume scattering (Leinss, 2015; Riche et al., 2013). This volume decorrelation can be quantitatively analysed with the help of the Pol-InSAR technique to obtain the volumetric SSD (ΔZ_s). In the following paragraphs, initially, an overview of the Pol-InSAR principle is provided, following which the existing Pol-InSAR based volumetric height inversion models are discussed. These generic models can be applied on any volume scatterer including tree, snow and ice (Cloude, 2010).

Pol-InSAR principle: The single baseline Pol-InSAR algorithm works on the basis of the complex coherence, $\tilde{\gamma}(\overrightarrow{w_1}, \overrightarrow{w_2})$, defined in Eq. (12) where $I_i(\overrightarrow{w_1}, \overrightarrow{w_2})$ denotes the i^{th} pixel coordinate value of the wrapped Pol-InSAR interferogram, $I(\overrightarrow{w_1}, \overrightarrow{w_2})$ obtained from Eq. (13) (Cloude, 2005, 2010). This interferogram is calculated from Eq. (14) and Eq. (15) where the coregistered master (s_1) and slave (s_2) images are acquired at a given polarisation vector ($\vec{w}$) respectively. Here, the weight vectors, $\overrightarrow{w_1}$ and $\overrightarrow{w_2}$ are selected by the user based on the scattering mechanisms at ends 1 and 2 of the interferometric baseline. If $\overrightarrow{w_1} = \overrightarrow{w_2}$, $\tilde{\gamma}(\overrightarrow{w_1}, \overrightarrow{w_2})$ can be alternatively specified as $\tilde{\gamma}(\overrightarrow{w_1})$ (Cloude, 2005, 2010). Moreover, L is the total number of pixels averaged in the range and azimuth directions which can be replaced by the ensemble averaging operation following the statistical ergodicity assumption (Hanssen, 2001; Hoen & Zebker, 2000; Kugler et al., 2015; S. Kumar et al., 2017; Papathanassiou & Cloude, 2001) Additionally, $\phi_{flat}^{w} \in [0, 2\pi)$ is the wrapped flat-earth phase obtained from the estimated absolute flat-earth phase (ϕ_{flat}) and has to be removed from $I(\overrightarrow{w_1}, \overrightarrow{w_2})$ as shown in Eq. (13). Also, the calculation of the generalised weight vector ($\vec{w}$) is given by Eq. (16).

$$\tilde{\gamma}(\overrightarrow{w_1}, \overrightarrow{w_2}) = \frac{\sum_{i=1}^{L} I_i(\overrightarrow{w_1}, \overrightarrow{w_2})}{\sqrt{\sum_{i=1}^{L}|s_{1i}(\overrightarrow{w_1})|^2 \sum_{i=1}^{L}|s_{2i}(\overrightarrow{w_2})|^2}}, |\tilde{\gamma}(\overrightarrow{w_1}, \overrightarrow{w_2})| \in [0, 1] \quad (12)$$

$$I(\overrightarrow{w_1}, \overrightarrow{w_2}) = s_1(\overrightarrow{w_1}) s_2^*(\overrightarrow{w_2}) e^{-j\phi_{flat}^{w}} \quad (13)$$

$$s_1 = w_1^1 \frac{s_{hh}^1 + s_{vv}^1}{\sqrt{2}} + w_1^2 \frac{s_{hh}^1 - s_{vv}^1}{\sqrt{2}} + w_1^3 \sqrt{2} s_{hv}^1 \quad (14)$$

$$s_2 = w_2^1 \frac{s_{hh}^2 + s_{vv}^2}{\sqrt{2}} + w_2^2 \frac{s_{hh}^2 - s_{vv}^2}{\sqrt{2}} + w_2^3 \sqrt{2} s_{hv}^2 \quad (15)$$

$$\vec{w} = [w^1 \quad w^2 \quad w^3]^T = [\cos\alpha \quad \sin\alpha\cos\beta e^{j\delta} \quad \sin\alpha\sin\beta e^{j\mu}]^T \quad (16)$$

where, s_{pp}^1 and s_{pp}^2 correspond to the master (1) and slave (2) images respectively, $pp \in \{hh,\ hv,\ vv\}$, and * denotes the complex conjugate operator.

In this case, the parameters, scattering alpha angle (α), target orientation angle (β), phase terms (δ and μ), are chosen according to the selected polarisation given by Table 1. Here, LL, LR and RR correspond to the left circular, left-right circular and right circular polarisations (Cloude, 2010). However, it is possible to optimise these parameters specific to the data, the details of which are provided by Cloude (2010).

Table 1: Pol-InSAR scattering mechanisms (Cloude, 2005).

Polarisation Selection	$\boldsymbol{\alpha}$ **(°)**	$\boldsymbol{\beta}$ **(°)**	$\boldsymbol{\delta}$ **(°)**	$\boldsymbol{\mu}$ **(°)**
HH	45	0	0	0
HV	90	90	0	0
VV	45	180	0	0
HH+VV	0	0	0	0
HH-VV	90	0	0	0
LL	90	45	0	90
LR	0	0	0	0
RR	90	45	0	-90

Height Inversion Algorithms: The three primary approaches for estimating the height of the volume scatterers are based on DEM differencing, general Random Volume over Ground (RVoG) model (considers extinction coefficient variation) and the coherence amplitude inversion (simplified RVoG) (Cloude, 2005). Among these, the two-layer RVoG model has been widely used for forest height and above ground biomass estimation (Hajnsek et al., 2009; Kugler et al., 2015; S. Kumar et al., 2017). The model descriptions in the context of SSD retrieval are summarised below:

a) DEM Differencing: This is the most straightforward algorithm wherein the difference between the top of the volume layer ($\overrightarrow{w_v}$ denoting the HV polarisation vector obtained from Table 1) and the estimated wrapped ground or topographical phase ($\phi_{topo}^{w} \in [0, 2\pi)$) is considered for height inversion (Cloude, 2005, 2010). The height estimate (ΔZ_s) is given by Eq. (17) where k_z is the vertical wavenumber (rad/m) and the function $\arg(\ldots)$ is defined in the interval $[0, 2\pi)$. The parameter m is set to 1 for bistatic acquisition and 2 in the monostatic case. Here, $\Delta\theta$ is the change in the incidence angle occuring due to the spatial baseline, θ is the mean incidence angle which can be replaced by the local incidence angle (LIA), and λ_0 is the radar wavelength (Cloude, 2010; Hajnsek et al., 2009).

$$\Delta Z_s = \frac{\arg\left(\tilde{\gamma}(\overrightarrow{w_v})e^{-j\phi_{topo}^{w}}\right)}{k_z}, k_z = m\frac{2\pi\Delta\theta}{\lambda_0 \sin\theta} \tag{17}$$

In this regard, ϕ_{topo}^{w} can either be estimated from a reference DEM or by solving the Eq. (18) wherein a surface dominated channel (e.g., HH-VV in Table 1), $\tilde{\gamma}(\overrightarrow{w_s})$ is used. However, this model generally results in underestimated values because of the dependence on the exact phase centre (Cloude, 2005, 2010).

$$\phi_{topo}^{w} = \arg\left(\tilde{\gamma}(\overrightarrow{w_v}) - \tilde{\gamma}(\overrightarrow{w_s})\left(1 - L_{\overrightarrow{w_s}}\right)\right) \tag{18}$$

where,

$$L_{\overrightarrow{w_s}} = \frac{-B - \sqrt{B^2 - 4AC}}{2A}, L_{\overrightarrow{w_s}} \in [0, 1]$$

$$A = |\tilde{\gamma}(\overrightarrow{w_v})|^2 - 1, B = 2\Re\left(\tilde{\gamma}(\overrightarrow{w_v}) - \tilde{\gamma}(\overrightarrow{w_s})\tilde{\gamma}^*(\overrightarrow{w_s})\right), \text{and } C = |\tilde{\gamma}(\overrightarrow{w_v}) - \tilde{\gamma}(\overrightarrow{w_s})|^2$$

b) Height using Extinction Coefficient: This algorithm is based on the two-layer (volume and surface) RVoG model and incorporates the extinction coefficient (σ_e) for height inversion. However, knowledge about the surface to volume scattering ratio ($\chi \in [0, 1]$) is required for the full RVoG model (Cloude, 2005, 2010) given by Eq. (19) where G is the objective function to be minimised. Here, $L_{\overrightarrow{w_v}} \in [0, 1]$ is a free parameter with $\phi_0^{w} \in [0, 2\pi)$ corresponding to the top of the volume layer phase (Cloude, 2010).

Hence, for resolving this multi-solution problem, the user needs to fix the value of χ. Generally, $\chi = 0$ is the usual choice for which $\vec{w} = \overrightarrow{w_v}$ (i.e., weight vector for HV channel should be used). This modification is shown in Eq. (20) wherein the minimisation function G involving the Euclidean norm ($\|\ldots\|$) can be computed either through iterative procedures (simplex method) or by using lookup tables (LUT). Still, optimising σ_e is not a trivial task as it represents the density and structure variations of the concerned volume scatterer and should be chosen after appropriate assessment (Cloude, 2005, 2010).

$$\min_{\Delta Z_s, \sigma_e} G(\chi, \vec{w}) = \left\|\tilde{\gamma}(\vec{w}) + \chi\left(e^{j\phi_0^{w}} - \tilde{\gamma}(\vec{w})\right) - e^{j\phi_{topo}^{w}}\widetilde{\gamma_v}\right\| \tag{19}$$

where,

$$\widetilde{\gamma_v} = \frac{p_1}{p_2}\frac{e^{p_2\Delta Z_s} - 1}{e^{p_1\Delta Z_s} - 1}$$

$$p_1 = 2\sigma_e/\cos\theta, p_2 = p_1 + jk_z, \text{and } \phi_0 = \arg\left(\tilde{\gamma}(\overrightarrow{w_v}) - \tilde{\gamma}(\overrightarrow{w_s})\left(1 - L_{\overrightarrow{w_v}}\right)\right)$$

$$\min_{\Delta Z_s, \sigma_e} G(\chi = 0) = \left\|\tilde{\gamma}(\overrightarrow{w_v}) - e^{j\phi_{topo}^{w}}\widetilde{\gamma_v}\right\| \tag{20}$$

c) Coherence Amplitude Inversion: The ground phase ambiguities caused by low coherence regions constitute a key issue for both the algorithms discussed above. One feasible way to resolve this issue is by incorporating only the coherence amplitude ($\gamma(\overrightarrow{w_v}) = |\tilde{\gamma}(\overrightarrow{w_v})|$) thereby discarding the phase information. In this model given by Eq. (21), a polarisation channel with expected low χ is required (e.g. HV). Since, the phase is ignored, it is sensitive to the density of the volume medium. As a result, two possible workarounds are to consider the zero extinction sinc model or use a regressed mean extinction coefficient

($\overline{\sigma_e}$) (Cloude, 2005, 2010). However, this is the least robust among the other two models and therefore, it should be used as a backup when other approaches fail to work (Cloude, 2005).

$$\min_{\Delta Z_s} G = \left\| \gamma(\overrightarrow{w_v}) - e^{j\phi_{topo}^{w}} \widetilde{\gamma_v} \right\|, \gamma(\overrightarrow{w_v}) \in [0, 1] \tag{21}$$

d) Hybrid Height Inversion Model: In order to improve the height accuracy, the coherence amplitude ($\gamma(\overrightarrow{w_v})$) and the ground phase ($\phi_{topo}^{w}$) can be related with the structure height (ΔZ_s) by using the Fourier-Legendre expansion of the structure function, $f(z)$, given by the infinite series Eq. (22) wherein a_{i0} are the coefficients (Cloude, 2010).

$$\tilde{\gamma}(\vec{w}) = e^{(k_v + \phi_{topo}^{w})} \left(f_0 + \sum_{i=1}^{\infty} a_{i0} f_i \right) \tag{22}$$

where,

$$a_{i0} = \frac{a_i}{1 + a_0}, k_v = \frac{k_z \Delta Z_s}{2}$$

The second-order Legendre model is given by Eq. (24) where $R_2 \approx |f_3| / |f_0|$ is the truncation error which is significantly smaller than that of the first order model, $R_2 \ll R_1$ as in Eq. (23). Although it will provide better height accuracy, the increased number of parameters poses difficulty while inverting (Cloude, 2010).

$$\tilde{\gamma}(\vec{w}) = e^{(k_v + \phi_{topo}^{w})} \left[\underbrace{\frac{\sin k_v}{k_v}}_{f_0 = \operatorname{sinc} k_v} + a_{10}(\vec{w})\, j \underbrace{\left(\frac{\sin k_v}{k_v^2} - \frac{\cos k_v}{k_v} \right)}_{f_1} \right] + R_1 \tag{23}$$

$$\begin{aligned} \tilde{\gamma}(\vec{w}) = e^{(k_v + \phi_{topo}^{w})} \Bigg[& \operatorname{sinc} k_v + a_{10}(\vec{w}) j \left(\frac{\sin k_v}{k_v^2} - \frac{\cos k_v}{k_v} \right) \\ & + a_{20}(\vec{w}) \underbrace{\left(\frac{3\cos k_v}{k_v^2} - \left(\frac{6 - 3k_v^2}{2k_v^3} + \frac{1}{2k_v} \right) \sin k_v \right)}_{f_2} \Bigg] + R_2 \end{aligned} \tag{24}$$

Intriguingly, this second-order model can be approximated by combining the DEM differencing approach in Eq. (17), and the sinc or f_0 coherence amplitude ($\overline{\sigma_e} = 0$) inversion model (Eq. (21)) (Cloude, 2010). This is defined in Eq. (25) wherein $\eta \in [0, 1]$ is a scaling parameter which effectively controls the volume structure variations. Moreover, this approach provides robustness to the height estimation and also offers a balance between the accuracy and computational complexity (Cloude, 2005, 2010). Here, the inverse of the sinc function ($\operatorname{sinc}_{\mathrm{C}}^{-1}$) can be approximated from Eq. (26) where $\gamma(\overrightarrow{w_v}) \in [0, 1]$ always hold (Cloude, 2010). Also, the subscript C denotes the Cloude (2010) approximation.

$$\Delta Z_s = \frac{\arg\left(\tilde{\gamma}(\overrightarrow{w_v}) e^{-j\phi_{topo}^{w}} \right)}{k_z} + \eta \frac{\operatorname{sinc}_{\mathrm{C}}^{-1}\left(\gamma(\overrightarrow{w_v}) \right)}{k_z} \tag{25}$$

$$\operatorname{sinc}_{\mathrm{C}}^{-1}\left(\gamma(\overrightarrow{w_v}) \right) = \pi - 2\sin^{-1}\left(\gamma(\overrightarrow{w_v})^{0.8} \right) \tag{26}$$

The sinc or the “sine cardinal” function is frequently used in the domain of signal processing and has two definitions which are commonly used (Weisstein, 2019). These are given by Eq. (27) and Eq. (28) where ψ is the angle (rad) which belongs to the set of complex numbers ($\mathbb{C}$). In this regard, it is noteworthy that Eq. (23), Eq. (24), and Eq. (26) use the traditional sinc function as in Eq. (27). However, the normalised sinc function (sinc_π) in Eq. (28) is adopted by most programming language libraries including SciPy (Jones, Oliphant, & Peterson, 2001; Weisstein, 2019).

$$\mathrm{sinc}\,\psi = \begin{cases} 1 & , \quad \psi = 0 \text{ rad} \\ \dfrac{\sin\psi}{\psi} & , \quad \text{otherwise} \end{cases} \tag{27}$$

$$\mathrm{sinc}_\pi\,\psi = \begin{cases} 1 & , \quad \psi = 0 \text{ rad} \\ \dfrac{\sin(\pi\psi)}{\pi\psi} & , \quad \text{otherwise} \end{cases} \tag{28}$$

2.2.2. Snow Water Equivalent Measurement

SWE, which is essentially the mass of snow on the ground, can be defined in terms of the snow density (ρ_{snow}) and snow depth (ΔZ_{snow}) as shown in Eq. (29). Here, the $\langle \ldots \rangle$ operator indicates ensemble averaging as before (Li et al., 2017) and $\Delta Z_{snow} \in \{\Delta Z_f,\ \Delta Z_d, \Delta Z_s\}$, i.e., either of the FSD (ΔZ_f), DSD (ΔZ_d) or SSD (ΔZ_s) can be used for SWE estimation.. Similarly, ρ_{snow} can be set as the fresh snow density (ρ_f), dry snow density (ρ_d), or the standing snow density (ρ_s). Evidently, the snow density plays a key role in the estimation of SWE (Leinss et al., 2015) and hence, a specific discussion on ρ_{snow} is put forward in the following subsection.

$$\mathrm{SWE} = \langle \rho_{snow} \rangle \Delta Z_{snow} \tag{29}$$

Snow Density as a Governing Factor

The microwave propagation speed depends on the dry snow density which again governs the backscatter signal delay particularly in the 10 MHz to 1 THz range (Leinss et al., 2015). As discussed earlier, $\Re(\epsilon_{snow})$ is also dependent on ρ_{snow} given by Eq. (9). Thus, in order to accurately estimate SD or SWE, the snow density needs to be properly measured.

In case of fresh snow, the density lies in between 0.03 and 0.12 g/cm^3, which then increases for vertical structures (depth hoar and firn) due to the occurrence of gradual snow metamorphosis (Judson & Doesken, 2000; Leinss et al., 2015; Roebber, Bruening, Schultz, & Cortinas, 2003). As a result, $\rho_{snow} =$ 0.5 g/cm^3 is common for dry or standing snow prior to the onset of snow melting. However, the seasonal snow density ($\rho_{critical}$) rarely exceeds 0.55 g/cm^3. Typically, $\rho_{snow} = 0.83$ g/cm^3 is observed for firn located deep underneath glaciers and ice sheets (Leinss et al., 2015). Moreover, the density of solid ice (ρ_{ice}) has been experimentally found to be 0.917 g/cm^3 (Spencer, Alley, & Creyts, 2001).

SWE Estimation using Multiple Differential Interferograms

Recently, a temporal integration based approach incorporating a stack of differential interferograms have been developed by Leinss et al. (2015). Although limited to dry snow, it avoids the phase unwrapping problem (Chen & Zebker, 2002), reduces decorrelation and is insensitive to orbit and atmospheric disturbances. However, the prerequisites for applying this method include sufficiently high radar wavelength (results in negligible volume decorrelation) and a high temporal resolution (Leinss et al., 2015).

Essentially, by summing up the absolute dry snow phase differences (ϕ_{snow}^{u}) obtained from a dense differential interferogram time-series, it is possible to isolate the phase fluctuations attributing to the temporal decorrelations, thereby improving the signal-to-noise ratio (SNR) (Leinss et al., 2015). Accordingly, the relation between this integrated or summed up phase ($\Delta\phi_{snow}^{u}$) and the change in SWE (ΔSWE) from time t_m to t_s (m and s representing the master and slave images respectively) can be well approximated by Eq. (30). Moreover, the optimal value of the free parameter $\vartheta \approx 1$ is dependent on the incidence angle and the maximum expected snow density (Leinss et al., 2015).

$$\Delta\mathrm{SWE} = \mathrm{SWE}(t_s) - \mathrm{SWE}(t_m) = \frac{\lambda_0 \Delta\phi_{snow}^{u}}{2\pi\vartheta\left(1.59 + \theta^{\frac{5}{2}}\right)} \tag{30}$$

Empirically, it has been observed that this approximation yields inaccurate results having root mean square error (RMSE) values more than 10% for $\theta \geq 60°$ which further increases with increasing values of θ (Leinss et al., 2015). Another important factor responsible for accurate SWE estimation is coherence which should be maintained between consecutive acquisitions. Otherwise, there is a significant degradation of the overall SNR and hence, low frequency and high repeat time airborne and spaceborne SAR systems are the most promising candidates in this regard (Leinss et al., 2015).

2.3. Chapter Summary

In this chapter, the physical and electromagnetic properties of snow have been discussed with microwave remote sensing of snow being the key focus. The state of the art models concerning snow depth and snow water equivalent estimation have been succinctly described along with their advantages and drawbacks. Moreover, several relevant literatures are cited for referring the reader to more advanced in-depth concepts that have been summarised in this chapter. Additionally, the symbologies or notations used in the equations and figures have been adopted from the existing literatures and in some cases, have been modified accordingly to remove any ambiguity. Starting from the next chapter, the thesis specific discussions are provided.

3. STUDY AREA, DATASETS AND SOFTWARE

In this chapter, at first, the geographical location of the study area and the terrain characteristics are discussed in section 3.1. Following this, the dataset, software tools and programming languages which have been used are provided in sections 3.2 and 3.3 respectively.

3.1. Chosen Study Area

3.1.1. Geographical Situation

The Beas river watershed near Manali, India is part of the north-western Himalayas. Naturally, steep slopes and dense forests are prominent in this region. The elevation typically varies from nearly 2500 m to more than 5000 m in some places as observed in the reference ALOS PALSAR DEM (Figure 6). In this work, a small region (~96 km^2) of the Beas basin is chosen which starts a few kilometres uphill from Dhundi up to Kothi (shown in Figure 6). These areas receive substantial seasonal snowfall which begins in December and lasts till late March. However, the cold, dry season usually commences from late September or early October. The coldest period is in January during which the temperatures reach a daily minimum of -15°C on an average. The summers are mild to occasionally warm with June being the hottest month (mean and maximum temperatures of 20°C and 30°C respectively are common). Apart from this, significant rainfall occurs between late June and September (monsoon season) with August receiving the maximum precipitation (Majumdar, Thakur, Chang, & Kumar, 2019; Thakur et al., 2012).

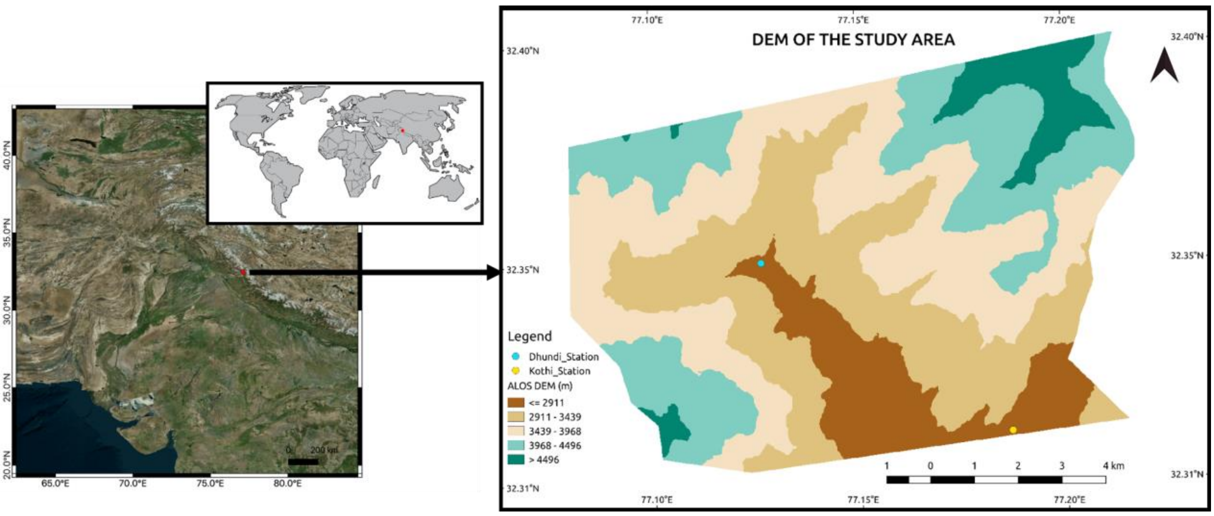

Figure 6: Overview map of the study area showing the ALOS PALSAR DEM. The original DEM of 12.5 m spatial resolution (generated in 2011) has been resampled to 3 m using bilinear interpolation to match the high resolution SAR data. Moreover, the vertical resolution as per the product specification is 5 m.

3.1.2. Field Visit

Intensive fieldwork had been conducted from October 14-21, 2018 in the Dhundi and Kothi areas where several Differential Global Positioning System (DGPS) measurements were acquired using the Leica Viva GS 10 (Leica Geosystems AG, 2012) with adequate horizontal positional accuracies (~7 cm) (Majumdar et al., 2019). Due to the complex terrains, most of the DGPS readings had been obtained through the kinematic mode (Luo, Richter, & Cole, 2014). However, in some of the convenient places such as the Dhundi base station and near the Kothi Automatic Weather Station (AWS), the static mode was used (Leica Geosystems AG, 2012). Eventually, elevation information from these DGPS points have been compared with the ALOS PALSAR DEM, the details of which are provided in section 5.2.4. Furthermore, the manual snow readings from 2014-2018 (snow depth, density, weather profile and other relevant data) which are maintained by the security personnel daily at Dhundi had been pagewise photographed using a smartphone camera. In order to properly understand and visualise the characteristics of the study area, selected field photographs and their brief description are shown from Figure 7(a)-Figure 7(i).

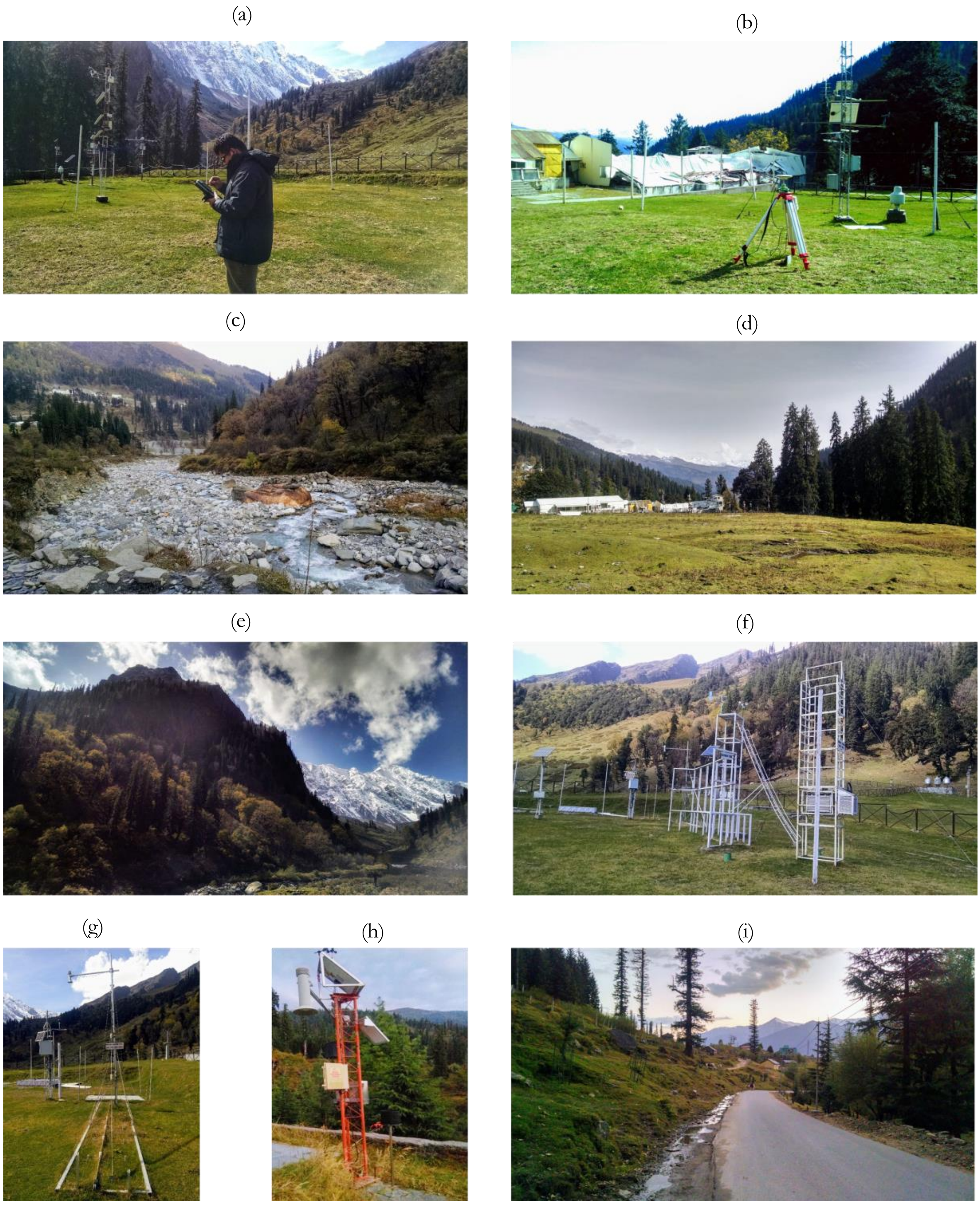

Figure 7: Field photographs showing (a) the positional accuracy checking of the (b) Leica DGPS base at Dhundi, (c) the Beas river bed, (d) human settlements, (e) mountains and forests, (f) weather instruments, (g) the installed SPA at Dhundi (h) AWS, and (i) surrounding landscape and forests at Kothi.

3.2. Datasets Used

Overall twelve Coregistered Single look Slant range Complex (CoSSC) TerraSAR-X (TSX)/TanDEM-X (TDX) bistatic X-band SAR images acquired between December 2015 and August 2017 in stripmap (SM) mode were available over this study area (Balss, Breit, Duque, Fritz, & Rossi, 2012). The relevant metadata for the InSAR and Pol-InSAR processing, such as the acquisition time, orbital direction, perpendicular baseline ($B_{\perp}$), height of ambiguity ($h_{2\pi}$), and the Doppler centroid frequency difference (Δf_{DC}) (Hanssen, 2001) are provided in Table 2. As seen from Table 2, there are six Quad-pol data pairs, from which the descending orbital pass acquisition at 00:53 hrs Universal Time Coordinated (UTC), January 8, 2016, has been selected considering the occurrence of fresh snowfall before, during and after the satellite flyby.

Table 2: Bistatic TerraSAR-X/TanDEM-X dataset metadata.

Date	Time (UTC)	Polarisations	Orbital Direction	$B_{\perp}$(m)	$h_{2\pi}$ (m)	Δf_{DC} (Hz)
29/12/2015	12:46	Quad	Ascending	273.51	18.54	5.58
08/01/2016	00:53	Quad	Descending	96.34	63.18	11.83
09/01/2016	12:46	Quad	Ascending	288.29	17.61	8.6
19/01/2016	00:53	Quad	Descending	96.10	63.34	4.11
20/01/2016	12:46	Quad	Ascending	289.68	17.53	12.53
30/01/2016	00:53	Quad	Descending	98.15	62.02	25.75
06/01/2017	12:46	HH	Ascending	230.17	22.18	20.96
24/03/2017	12:46	Dual	Ascending	377.97	13.44	10.82
15/04/2017	12:46	Dual	Ascending	327.53	15.52	2.58
26/04/2017	12:46	Dual	Ascending	286.69	17.73	10.11
08/06/2017	00:53	Dual	Descending	93.09	65.37	8.57
24/08/2017	00:53	Dual	Descending	17.51	347.49	0.08

Moreover, the in-situ snow physical parameters' data (standing and fresh snow depths, snow density) along with the relevant weather data had been transferred to a PostgreSQL database (DB) (PostgreSQL, 2019) from the photographs of the manual recordings through spreadsheets. Apart from this, the high frequency data (two-minute interval measurements) obtained from the snowpack analyser (SPA) device (installed at Dhundi) had been downloaded and were added to the database as a separate table. Accordingly, the SSDs at 06:22 hrs (00:52 hrs UTC) Indian Standard Time (IST) on January 7, 2016, and 06:22 hrs January 8, 2016 morning were 36.2 cm and 54.9 cm respectively signifying a heavy fresh snowfall event of 18.7 cm within 24 hrs. The manual recordings also showed an FSD of 18 cm on January 8, 2016 morning though the exact measurement time is unspecified in the record book. Apart from this, a forest mask used in the earlier studies of this area (Thakur et al., 2017, 2012) has been obtained from the Water Resources Department (WRD), Indian Institute of Remote Sensing (IIRS).

3.3. Software Tools/ Programming Languages

The Sentinel Application Platform (SNAP) 6.0.5 (ESA, 2018) has been used for basic SAR processing. Initially, the DEM generation steps had been carried out through the Delft object-oriented radar interferometric software (Doris) v5.0.3Beta (Kampes & Usai, 1999) for testing purposes. In addition to this, the FSD and SSD inversion models have been implemented using Python 3 wherein PyCharm Community Edition 2018.1 (JetBrains, 2018) was used as the Integrated Development Environment (IDE). Moreover, the final SD and SWE maps have been prepared using QGIS 2.18 (QGIS, 2016). Furthermore, some of the computationally intensive tasks have been carried out using the High-Performance Computing (HPC) infrastructure installed at IIRS.

3.4. Chapter Summary

The primary focus of this chapter is to highlight the characteristics of the study area which are discussed in section 3.1. In chapters 5 and 6, the effect of these terrain features (acting as uncertainty sources) on the SAR backscattering mechanisms are discussed. Moreover, the metadata and a brief overview of the available datasets have been mentioned. Also, a discussion on the measurement of the relevant in-situ data is put forward to better understand their reliability. Furthermore, a short description of the software tools which have been used for data processing is provided. The next chapter deals with the methodological context consisting of the complete workflows which in turn, incorporate the aforementioned datasets (section 3.2).

4. METHODOLOGY

This chapter deals with the methodological framework which has been followed to generate the SD and SWE results. In order to briefly put the overall workflow, a flowchart is shown in Figure 8 which highlights the main process blocks.

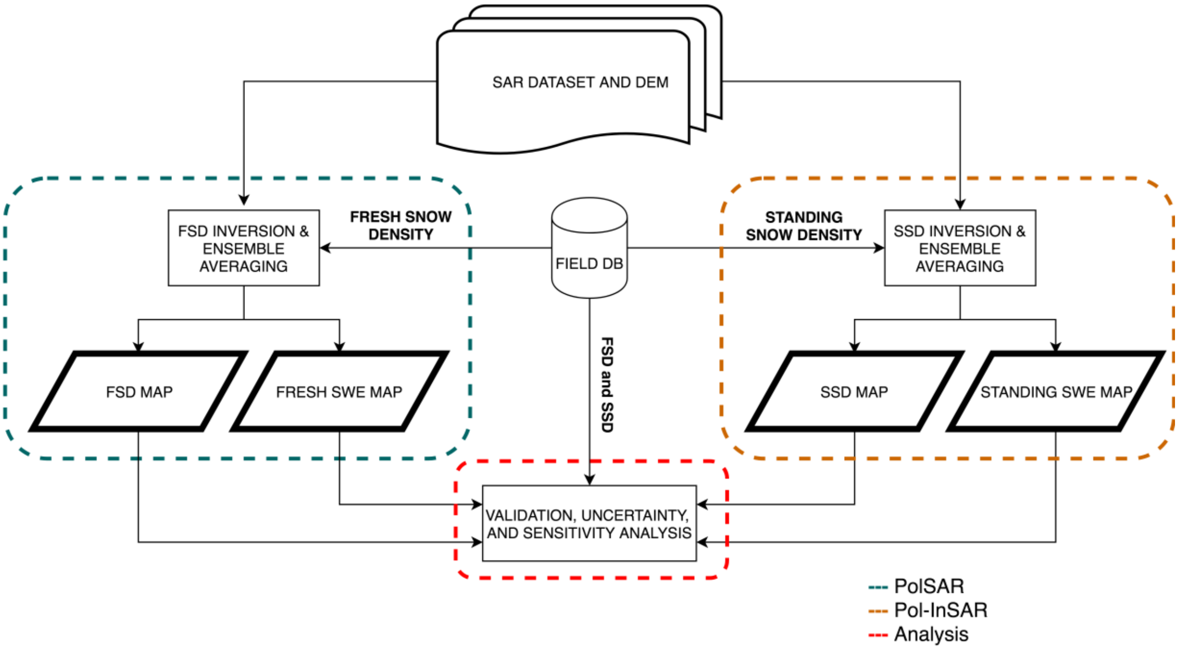

Figure 8: Overview of the main processing blocks.

Here, the preprocessing steps are discussed in section 4.1. Moreover, the PolSAR CPD and Pol-InSAR based approaches used for the FSD and SSD estimation respectively are individually addressed in sections 4.2 and 4.3. Finally, the uncertainty assessment, validation and sensitivity tasks are described in section 4.4.

4.1. Data Preprocessing

Since the SAR dataset is already coregistered, separate coregistration step has not been performed. In case of the FSD estimation model, the geocoded or terrain-corrected data (3 m spatial resolution) consists of the HH and VV scenes along with the LIA computed from the ALOS PALSAR DEM. As for the Pol-InSAR scenario, all the SAR channels, i.e., HH, HV, VH and VV along with the LIA are present in the geocoded data. It should be noted that, for the Pol-InSAR, processing both the master, TDX (master) and TSX (slave) images are required to generate the interferogram. However, the FSD estimation model can be used using any one of these images, though the average of the TDX and TSX CPDs can potentially improve the SNR (Leinss et al., 2014).

4.2. CPD based Fresh Snow Depth Estimation

The FSD is estimated using the CPD method developed by Leinss et al. (2014). At first, ϕ_{CPD} for the TDX data ($\phi_{CPD,TDX}$) acquired on January 8, 2016, is computed using Eq. (2) and then an ensemble averaging operation is applied over a 21×21 window. Similarly, ϕ_{CPD} for the TSX data ($\phi_{CPD,TSX}$) is calculated following which the average CPD, $\overline{\phi_{CPD}}$ is obtained using Eq. (31).

$$\overline{\phi_{CPD}} = \frac{\phi_{CPD,TDX} + \phi_{CPD,TSX}}{2} \tag{31}$$

Next, the depolarisation factors, N_x, N_y, and N_z are calculated by setting the axial ratio, $a_x/a_z = 1.5$ in Eq. (5) and choosing the snow particle shape as an oblate (Leinss et al., 2014). After this, the anisotropic effective permittivities, $\epsilon_{eff,i}\ \forall_i \in \{x, y, z\}$, are computed using Eq. (6). Finally, the FSD and FSWE are calculated from Eq. (8) and Eq. (29) respectively wherein an ensemble averaging filter of size 65×65 is applied. Also, the fresh snow density ($\rho_f = 0.07$ g/cm^3) which is manually measured at Dhundi, is kept constant for the entire study area along with the copolar coherence threshold, $\tau_c = 0$ ($\tau_c \in [0, 1]$), i.e., no thresholding has been applied, but the provision for it is built-in to the implementation. Moreover, as per the TSX/TDX metadata, the radar wavelength, $\lambda_0 \approx 3.11$ cm. In this context, the adopted workflow is depicted in Figure 9.

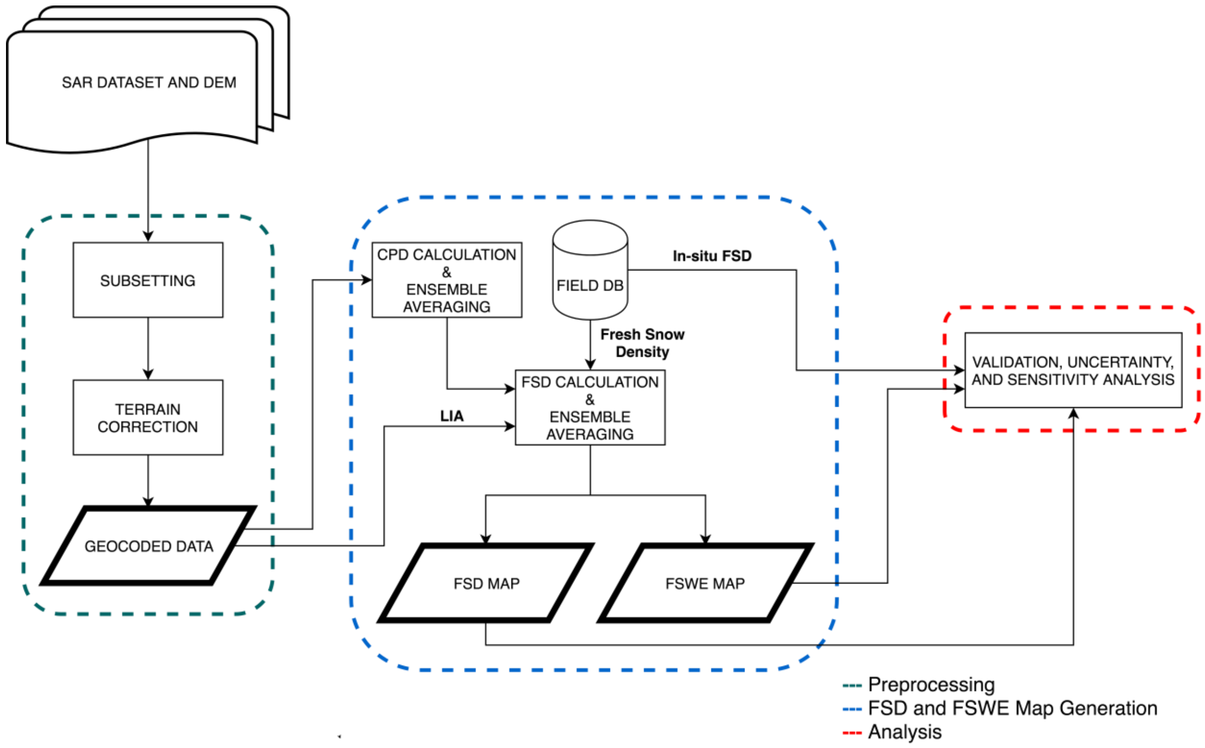

Figure 9: FSD and FSWE estimation workflow using PolSAR CPD.

4.3. Pol-InSAR based Standing Snow Depth Estimation

The hybrid DEM differencing and coherence amplitude based Pol-InSAR volumetric height inversion model as given by Eq. (25) is used for the SSD estimation. Firstly, the volume scattering dominant channels, HV and VH, are averaged to fully utilise the quad-pol data (Cloude, 2005). Next, the Pol-InSAR interferogram, $I(\vec{w_v})$, has been computed using Eq. (13) wherein $\vec{w_v}$ is obtained from Table 1 for the HV polarisation. Thereafter, the complex volume coherence, $\tilde{\gamma}(\vec{w_v})$, is calculated from Eq. (12) with $L = 3$. Similarly, the complex surface or ground coherence, $\tilde{\gamma}(\vec{w_s})$, is computed by choosing $\vec{w_s}$ as the HH-VV weight vector (Table 1). The volume and surface coherences are then used to estimate the wrapped ground phase, ϕ_{topo}^{w}, from Eq. (18). Additionally, a median ensemble filter of 21×21 is applied on the obtained ϕ_{topo}^{w} following the processing steps provided by Cloude (2005).

Moreover, the vertical wavenumber, k_z, when varied with the LIA in Eq. (17), is in the order of 0.1 rad/m with the ambiguity height, $h_{2\pi} = 2\pi/k_z \approx 63.18$ m (Table 2), $\lambda_0 \approx 3.11$ cm and $m = 1$ (single-pass acquisition). Since the maximum height of the distributed volume scatterer (in this case, standing snow), $\Delta Z_{s,max}$, should be similar to $h_{2\pi}$ (Kugler et al., 2015; S. Kumar et al., 2017), k_z has to be rescaled to an optimum range for effectively estimating the SSD. Hence, the modified vertical wavenumber, k_z', is given by Eq. (32) where η' is a free scaling parameter which has to be set according to the known $\Delta Z_{s,max}$ in the study area. Here, $h_{2\pi}'$ is the scaled height of ambiguity which like that of $h_{2\pi}$ determines the height changes in modulo 2π (Hanssen, 2001). Also, $\mathbb{R}_{>0}^{+}$ denotes the set of all positive real numbers in the interval (0, ∞). In this work, due to the limited ground-truth data availability and the subsequent ensemble averaging operation (window size of 21×21) on k_z', $\Delta Z_{s,max} = 12$ m has been assumed for which $\eta' = 5$ is used.

$$k_z' = \langle \eta' k_z \rangle \quad (32)$$
$$\text{where, } \eta' \in \mathbb{R}_{>0}^{+} \,\big|\, \Delta Z_{s,max} \approx h_{2\pi}' = 2\pi/k_z'$$

Eventually, the SSD and SSWE are estimated using Eq. (25) and Eq. (29) respectively wherein the standing snow density ($\rho_s = 0.315$ g/cm^3) measured by the Dhundi SPA at 06:22 hrs IST on January 8, 2016, has been used. Here, $\eta = 0.65$, the volume coherence threshold, $\tau_v = 0.6$ (pixels having $\tau_v < 0.6$ are neglected $\forall \tau_v \in [0, 1]$), and the SSD values are averaged based on a 57×57 ensemble filter window. The entire Pol-InSAR workflow is summarised in Figure 10 which shows the main processing blocks.

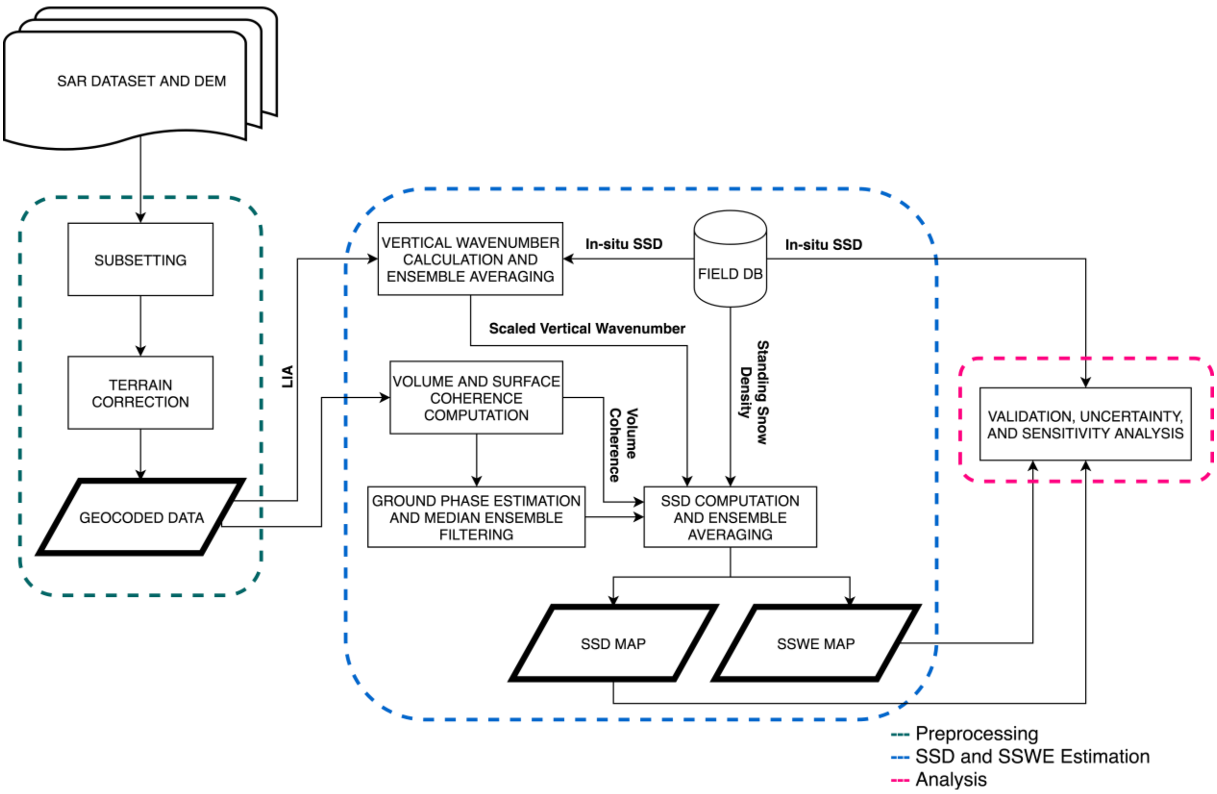

Figure 10: SSD and SSWE estimation workflow using Pol-InSAR.

However, in order to compute the inverse sinc function in Eq. (25), the approximation in Eq. (26) is replaced by Eq. (33) where the secant method (Cheney & Kincaid, 2012) has been applied to find $\alpha_r \in \mathbb{R}$

(rad), the desired root or inverse. Still, in the Python implementation, this approximation given by Cloude (2010) is used as an initial guess to the secant method for fast convergence. It is also used as a fallback option if the secant method is unable to converge within 50 iterations or the default convergence threshold of 1.4E-8 (Jones et al., 2001). This root finding technique has been deployed as it is more accurate than the given approximation in Eq. (26), the analysis of which is described in page 40.

$$\operatorname{sinc}_{\pi} \alpha_r - \gamma(\overrightarrow{w_v}) = 0 \tag{33}$$

In order to make the Cloude (2010) approximation compliant with the scientific computing libraries (such as SciPy) which use the $\operatorname{sinc}_{\pi}$ function, Eq. (26) can be replaced by Eq. (34) where $\operatorname{sinc}_{\pi_C}^{-1}$ denotes the inverse of the $\operatorname{sinc}_{\pi}$ function computed using the Cloude (2010) approach. Similarly, $\operatorname{sinc}_{\pi_S}^{-1}$ represents the inverse of the $\operatorname{sinc}_{\pi}$ function obtained by applying the secant method (Cheney & Kincaid, 2012; Jones et al., 2001).

$$\operatorname{sinc}_{\pi_C}^{-1}\left(\gamma(\overrightarrow{w_v})\right) = 1 - \frac{2\sin^{-1}\left(\gamma(\overrightarrow{w_v})^{0.8}\right)}{\pi} \tag{34}$$

4.4. Validation, Uncertainty Assessment, and Sensitivity Analysis

4.4.1. Validation Process

One of the significant challenges in this work has been the limited ground-truth data availability. Since, in-situ data from only two ground stations are available, the conventional way of accuracy assessment through regression plots (Kugler et al., 2015; Leinss et al., 2014) is infeasible in this context. Moreover, the Kothi AWS area falls in the layover region for the descending pass acquisitions and hence, only the Dhundi region which is free from layover, shadow and foreshortening effects, is used for validation. In this case, a neighbourhood window of size 3×3 (81 m^2 ground area) surrounding the Dhundi SPA is selected for validating the processed SD and SWE results by considering only the statistical mean and standard deviation.

4.4.2. Uncertainty Assessment

Due to the complex terrain characteristics there exist significant uncertainty sources which could potentially lead to the overall degradation of the output accuracy. Although the winter-time data (January 8, 2016) is fully polarimetric, the summer-time data (June 8, 2017) is dual-pol. So, in order to comparatively understand the backscattering mechanisms in these two scenes, the dual-pol entropy (H $\in$ [0, 1]) and the scattering alpha angle ($\alpha \in$ [0°, 90°]) or H-α decomposition (5×5 window size) is used (Cloude, 2010; Lee & Pottier, 2009; Singh et al., 2014). This is carried out through the H-α plane plot which demarcates eight feasible zones (Z9 being the unclassified pixels) based on the different scattering classes as shown in Figure 11 . It should be noted that, this diagram which follows the SNAP style (ESA, 2018), uses slightly different labels as compared to the Lee & Pottier (2009) H- α plane convention where the labels Z1, Z2, Z3 are denoted as Z7, Z8, Z9 and vice-versa respectively. However, the scattering mechanisms are exactly the same in both these conventions. Here, the blue curve acts as a boundary to the plane which essentially denotes the reliability of the classification in high entropy conditions (Brunner, 2009).

The dual-pol H-α decomposition is further used by the unsupervised Wishart classifier (ten iterations) which classifies the SAR data based on these scattering mechanisms and a quantitative estimate of the number of pixels in each such class can be obtained (Cloude, 2010; Lee & Pottier, 2009). Therefore, by knowing the scattering properties, the terrain features present in the study area can be understood along with their changes during the snow season. In turn, these ground features which include rough surfaces, shrubs, boulders, and human settlements reduce the copolar coherence amplitude (γ_c) thereby leading to underestimated FSD results (Leinss et al., 2014). In addition to this, the decrease in the Pol-InSAR surface coherence amplitude ($\gamma(\overrightarrow{w_s}) = |\tilde{\gamma}(\overrightarrow{w_s})|$) may result in overestimated volumetric height (Cloude, 2010; Hajnsek et al., 2009; Kugler et al., 2015), in this case, SSD. Thus, the uncertainty assessment by means of the identification of the backscattering mechanisms constitutes a key role in this work.

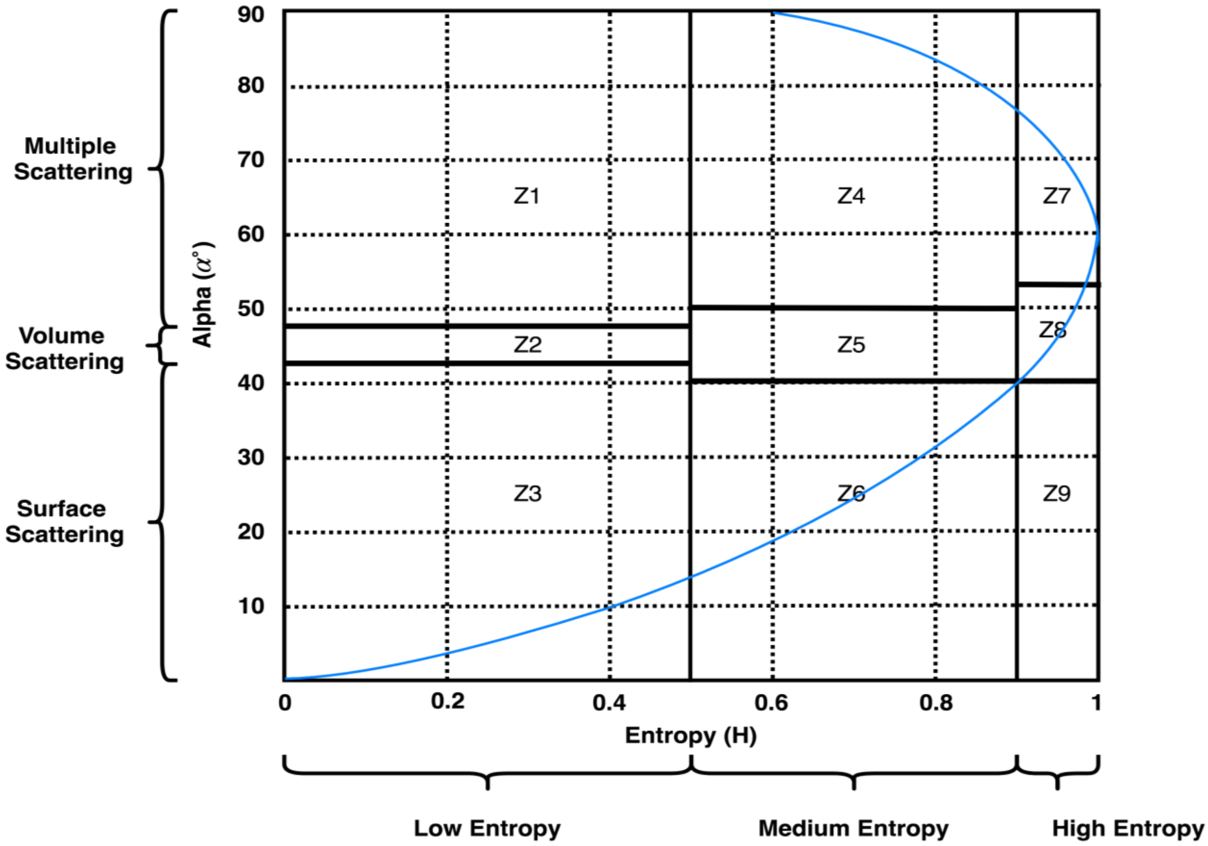

Figure 11: H-α plane showing different scattering zones. Z1: Dihedral, Z2: Dipole, Z3: Bragg Surface, Z4: Double bounce, Z5: Anisotropic, Z6: Random surface, Z7: Complex structures, Z8: Random anisotropic, Z9: Non-feasible.

Apart from this, the forest cover (obtained from WRD, IIRS) along with the layover and shadow regions computed using SAR simulation are used to mask out the pixels which degrade the quality of the results. This is a standard approach used in the studies focusing on snow property estimation in forested or alpine terrains (Leinss et al., 2014, 2015; Singh et al., 2017; Thakur et al., 2012; Usami et al., 2016).

4.4.3. Sensitivity Analysis

The variation of the SD and SWE values corresponding to the changes in the free parameters in the FSD and SSD inversion models (window size, coherence threshold, scaling factors) are observed by iteratively running the algorithms and computing the statistical mean and standard deviation using the neighbourhood window discussed earlier in this chapter (section 4.4.1). This helps in deciding the window shape and sizes and also choosing the optimum values for the several free parameters. Moreover, the accuracy of the root finding algorithm discussed in section 4.4.2 is also checked for some possible coherence values.

Additionally, the slope and aspect maps prepared from the ALOS PALSAR DEM along with the elevation values are used to observe the sensitivity of the obtained SD and SWE results toward these parameters. In this regard, it should be noted that snow accumulation is highly susceptible to the elevation, slope, aspect, wind speed, air temperature and various other hydrometeorological factors (Anderton, White, & Alvera, 2004; Grünewald, Bühler, & Lehning, 2014; Thakur et al., 2012; Zheng, Kirchner, & Bales, 2016) However, for simplicity, only these three variables are considered in this context.

In addition, the ground elevation measurements acquired during the field visit to Dhundi and Kothi have been compared with the ALOS PALSAR DEM elevations (z). The effect of the DEM errors on the LIA, θ_l, is then checked for performing SA using Eq. (35) which incorporates the slope angles in x (ω_x) and y (ω_y) directions (pixel co-ordinate system where z is the corresponding elevation value) derived from the DEM elevation values along with the radar incidence angle (θ) (Lee & Pottier, 2009; Lee, Schuler, & Ainsworth, 2000). Here, the terms dz/dx and dz/dy refer to the rate of elevation (z) change in the x and y directions respectively. The workflow which has been adopted for the uncertainty assessment and SA is shown in Figure 12.

$$\theta_l = \cos^{-1} \frac{\cos \omega_x \cos(\omega_y - \theta)}{\sqrt{\cos^2 \omega_y \sin^2 \omega_x + \cos^2 \omega_x}} \tag{35}$$

where,

$$\omega_x = \tan^{-1} \frac{dz}{dx}, \omega_y = \tan^{-1} \frac{dz}{dy}$$

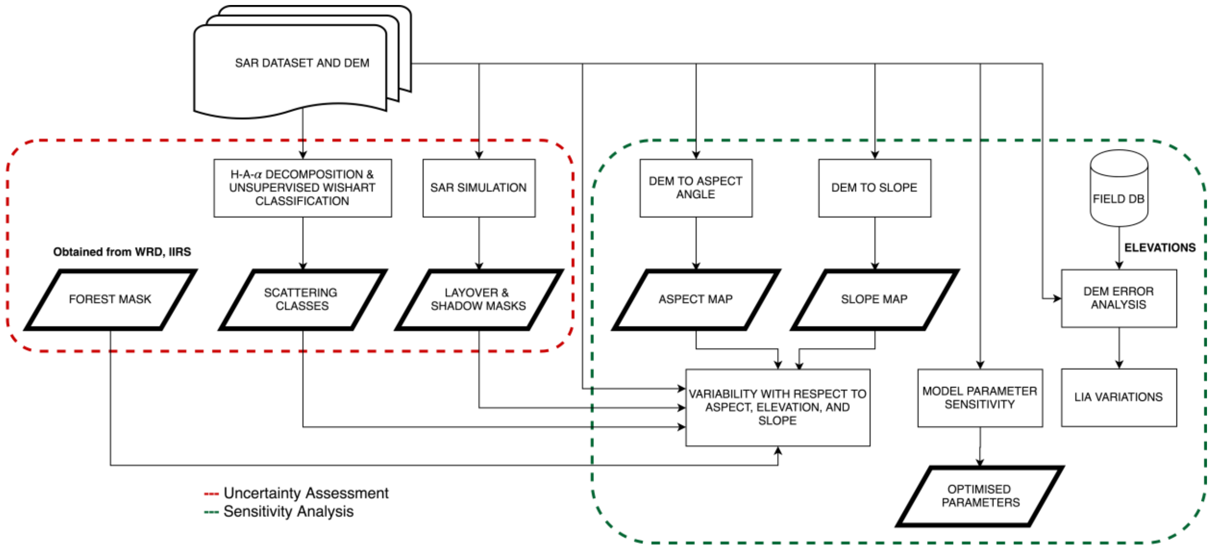

Figure 12: Workflow adopted for carrying out uncertainty assessment and sensitivity analysis.

4.5. Chapter Summary

This chapter begins with a brief overview of the SAR techniques adopted for the FSD, SSD, FSWE and SSWE estimations. Thereafter, the methodological steps, parameter values and the necessary preprocessing tasks are discussed. Moreover, the validation process, uncertainty assessment and SA methods which are used in this study are also addressed. In the next chapter, the obtained results and the relevant analysis are described.

5. RESULTS AND ANALYSIS

In this chapter, the FSD, FSWE, SSD, and SSWE results are shown for the TSX/TDX acquisition on January 8, 2016. Additionally, the SA graphs along with the uncertainty assessments are provided.

5.1. Scattering Mechanisms

The winter (January 8, 2016) and summer-time (June 8, 2017) dual-pol H-α decomposition (Figure 15) and unsupervised Wishart classification (Figure 13) results combined with the derived class percentage statistics (Figure 14) show that, in the presence of snow, the high entropy anisotropic volume scattering (Z8) increases by 5.11% whereas the medium entropy volume scattering (Z5) decreases by 7.01% for the entire study area. This reduction in the Z5 volume scattering could be attributed to the partially snow covered forests and shrubs which exhibit higher volume scattering at X-band during the snow-free season (Figure 7(e)). The corresponding dual-pol Wishart classified maps are displayed along with the zoomed views in Figure 13(a) and Figure 13(b) respectively.

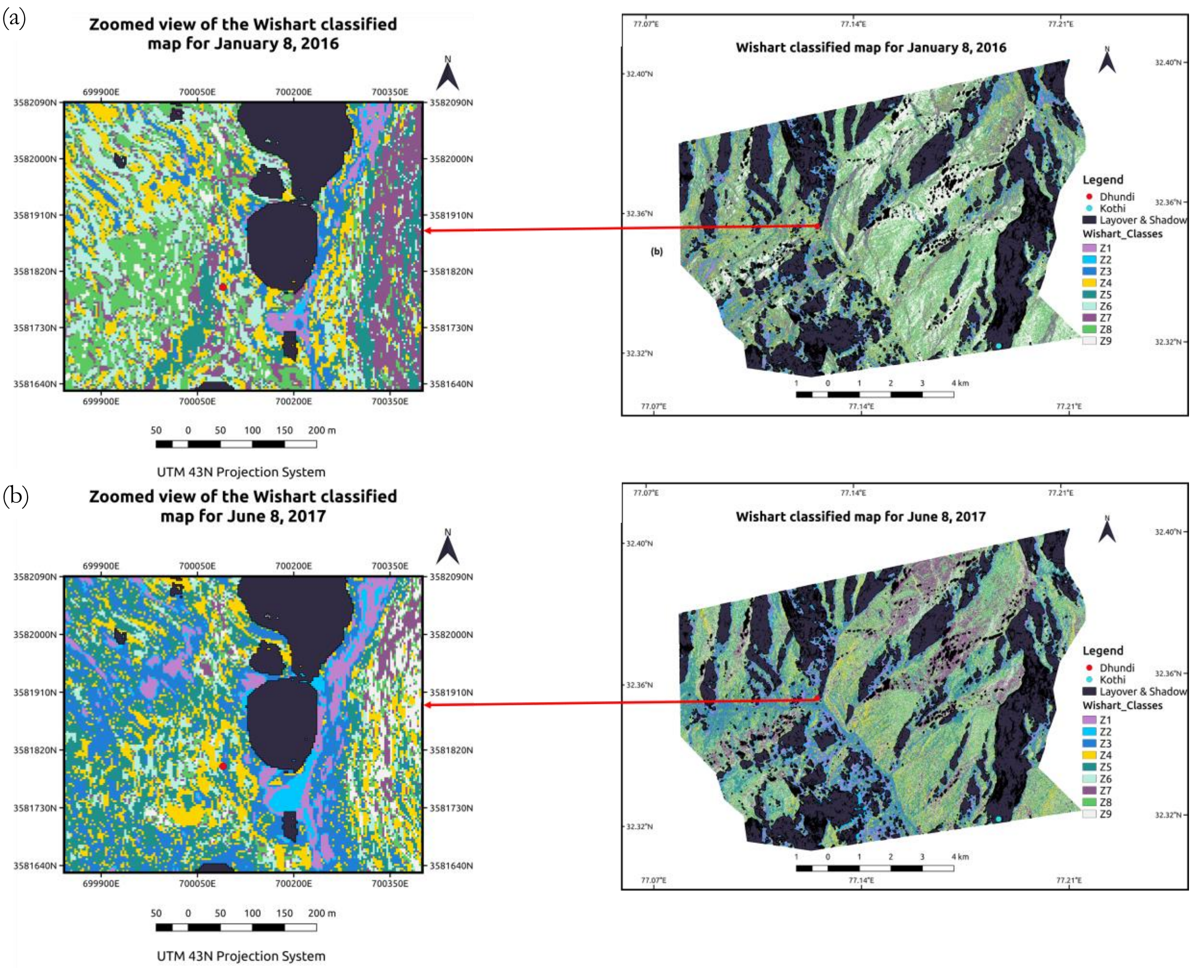

Figure 13: Zoomed views (over Dhundi) of the Wishart classified maps for the (a) January 8, 2016 data, and (b) the June 8, 2017 data. Here, only the layover and shadow mask has been applied. Also, the Kothi area is excluded from the analysis since it lies in the layover region.

Moreover, the Bragg surface scattering (Z3) is slightly higher in summer (10.88%) as compared to the winter (10.38%). One plausible reason for this is the 20 mm rainfall which occurred on June 7, 2017, evening (data retrieved from the Dhundi record book). Also, the occurrence of fresh snowfall in areas which did not have prior standing or old snow could result in surface scattering from the ground (Leinss et al., 2014). Apart from this, the asbestos gable roofs used in the human settlements (Figure 7(b) and Figure 7(d)) are strong single-bounce surface scatterers (Brunner, 2009). However, with snow accumulation on these materials, the surface scattering could be reduced. Another prominent feature noticeable in Figure 13(b) is the high amount of surface scattering from the river bed (Figure 7(c)) during the summer season. This is caused by both the boulders and the increasing flow of snow-melt water in the river (Figure 7(c)).

Furthermore, the human settlements result in double-bounce scattering (Z4) (Brunner, 2009), which in the winter-time scenario reduces by 0.34%. Also, the random surface scattering (Z6) increases by 0.66% which could be caused by the presence of small snow patches on the ground. Other than this, there is a strong decrease in the low entropy multiple (dihedral) scattering from 8.23% to 5.17% in the snow-covered season which could be caused by the added snow layer on the buildings and also boulders.

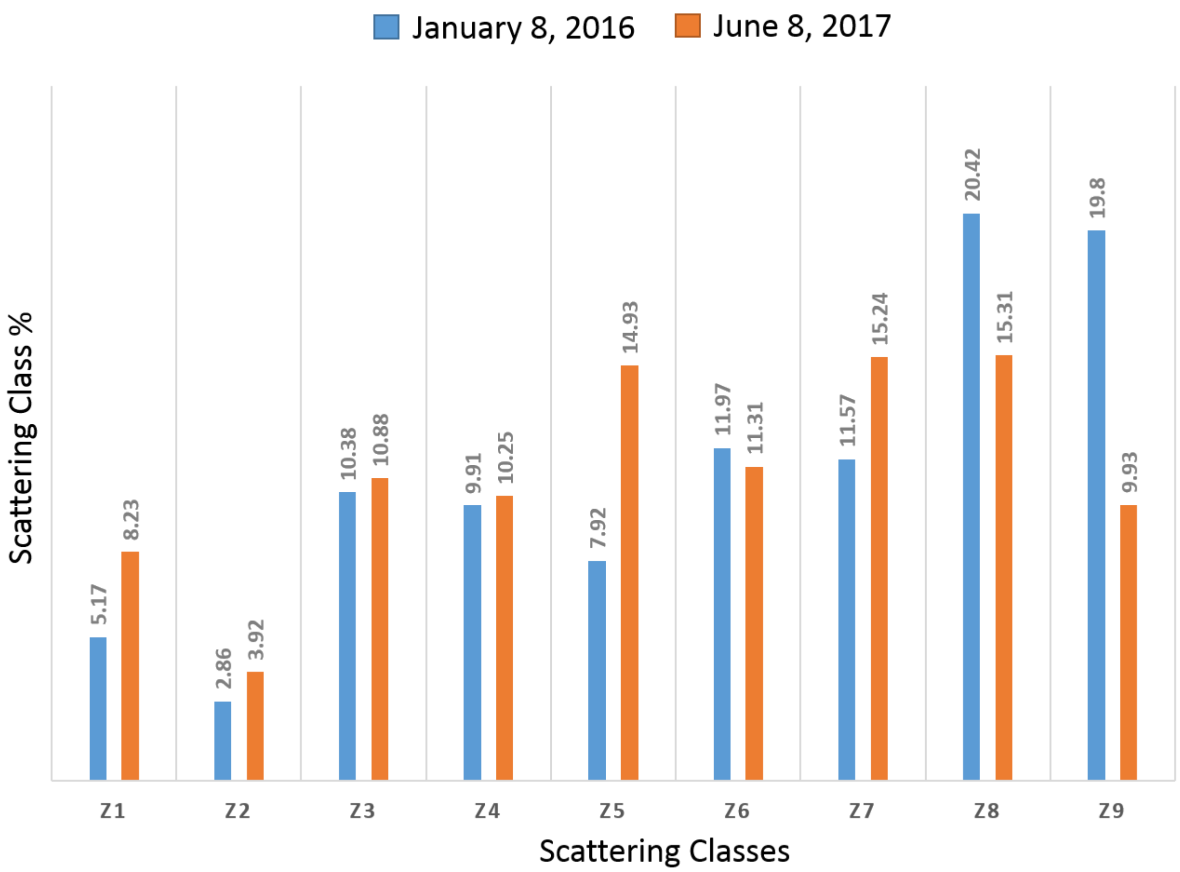

Figure 14: Scattering class percentages (rounded to 2 decimal places) from the unsupervised Wishart classification. The different zone labels are described in Figure 11.

Another interesting aspect in this context is the increase (from 9.93% to 19.8%) in the number of unclassified or non-feasible pixels (Z9) for the winter-time image (Figure 14) which is also depicted through the H-α plane plots in Figure 15(a) and Figure 15 (b). This is primarily resulting from the added terrain complexity owing to the snow accumulation. In order to resolve this issue, the quad-pol entropy

(H), anisotropy (A ∈ [0, 1]), alpha (α), H-A-α decomposition have been applied on the January 8, 2016 data. The corresponding H- α plane plot in Figure 15 (c) shows that the quad-pol approach is able to fully classify the winter-time image. However, since the summer-time image is having only HH and VV channels, the dual-pol method has been used to properly compare the respective scattering mechanisms.

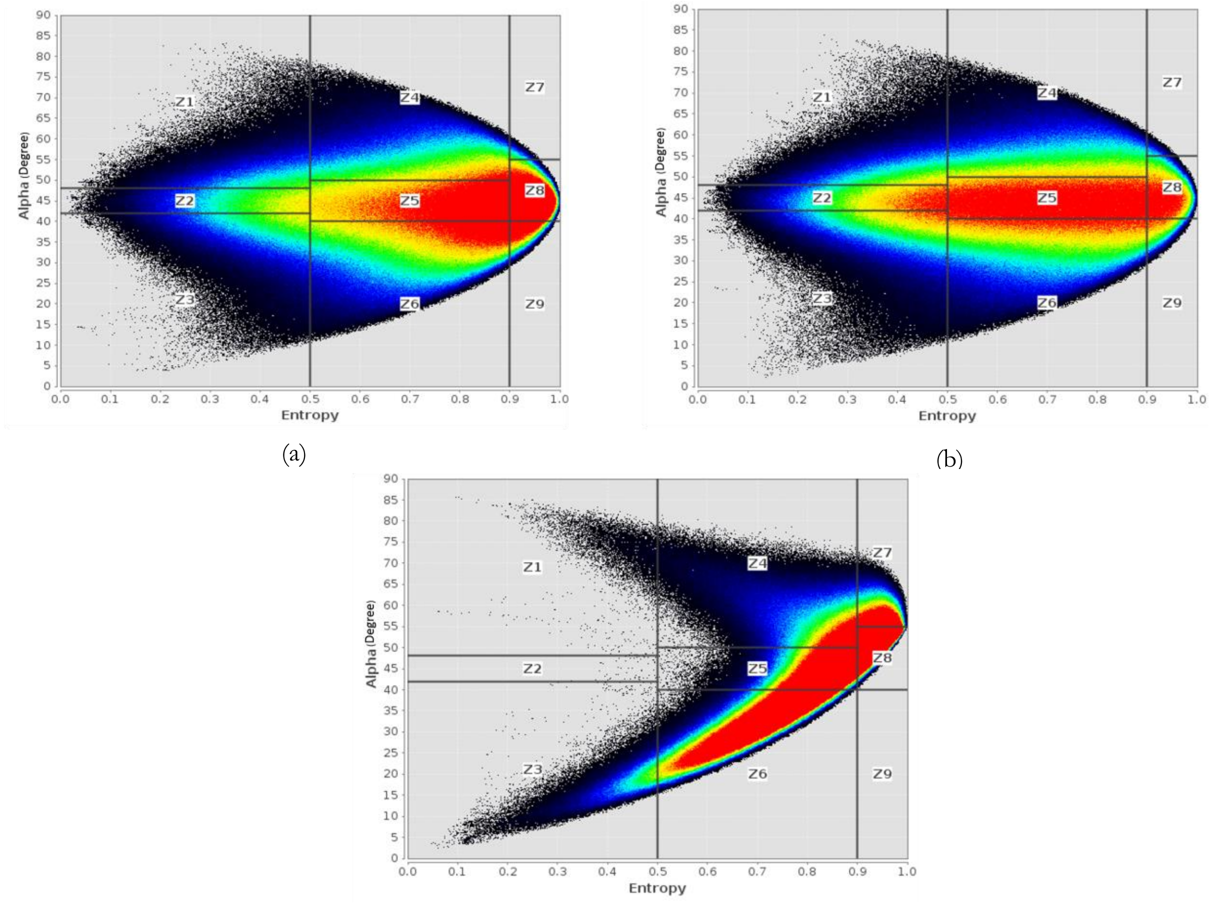

(a)

(b)

(c)

Figure 15: Dual-pol H-α plane plots for the (a) January 8, 2016, and (b) June 8, 2017 data, (c) Quad-pol H-α plane plot for the January 8, 2016 data. The colours red, green, and blue indicate the point density with red being the highest, and blue as the lowest. These plots have been made using SNAP (ESA, 2018).

Thus, from this discussion, it is clearly observed that the presence of snow causes a substantial change of the scattering patterns in the study area resulting in significant uncertainty sources. In turn, the optimisation of the model parameters along with the sensitivity analysis of the FSD and SSD values depend on these scattering types. As an example, if there is low surface scattering then the FSD inversion model leads to underestimated values (Leinss et al., 2014) whereas for low volume scattering, the SSD results are generally underestimated (Cloude, 2005; Hajnsek et al., 2009; Kugler et al., 2015; S. Kumar et al., 2017). Therefore, the uncertainty assessment by means of the scattering mechanism classification is one of the key aspects of this research.

5.2. Sensitivity Analysis Results

The SA has been extensively performed for the various free parameters in the FSD and SSD inversion models. Moreover, the effects of the terrain aspect, elevation and slope have been considered to analyse the variations of the FSD, SSD, and also the different scattering mechanisms with respect to these topographical variables. However, since the SWEs are computed by multiplying a constant snow density ($\rho_s = 0.315$ g/cm^3, and $\rho_f = 0.07$ g/cm^3), the terrain-specific SA is only carried out for the FSD and SSD values. Also, the Kothi area is falling in the layover zone, and hence, it is not used as a validation point.

5.2.1. FSD Model Parameters

The FSD inversion model discussed in sections 2.2.1 and 4.2 apply the ensemble averaging operation twice— once on the computed CPD and then subsequently on the output FSD values. As a result, the selection of an optimal window size in both these cases is critical in obtaining reliable estimates. At first, the mean (μ_{γ_c}) and standard deviation (σ_{γ_c}) of the copolar coherence amplitude (γ_c) are checked over the Dhundi area based on a 3×3 neighbourhood window (same as the validation window in section 4.4.1). The ensemble window for which the maximum μ_{γ_c} occurs is subsequently used for estimating the FSD following the methodology described in section 4.2. This selection procedure concerning the maximisation of μ_{γ_c} is depicted in Figure 16 wherein the ensemble window of size 3×3 is found to be suitable even though $\sigma_{\gamma_c} \approx 0.06$ of this window is slightly higher than that ($\sigma_{\gamma_c} \approx 0.02$) of the 5×5 window.

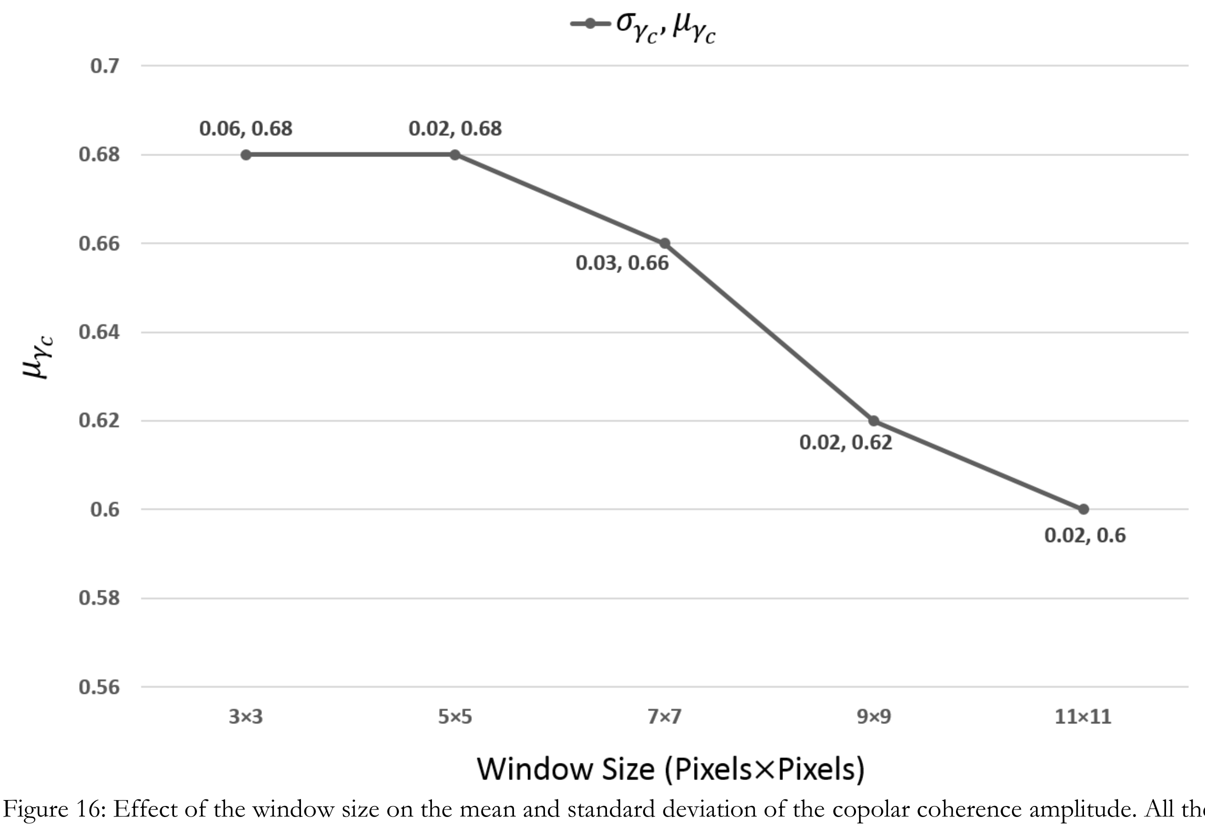

Figure 16: Effect of the window size on the mean and standard deviation of the copolar coherence amplitude. All the values are rounded to 2 decimal places. Here, only odd window sizes are considered because these have been previously used in prior studies (V. Kumar & Venkataraman, 2011; Leinss et al., 2018, 2014).

Next, the sensitivity of the FSD values with respect to the ensemble window size is taken into account. This is shown in Figure 17 where the analysis starts from the window size 45×45 and continues till 65×65 with an increment of two pixels in each direction. In this context, smaller window sizes (<45×45) are not considered following the work of Leinss et al. (2014) where a 45×35 window size has been chosen.

Similarly, higher window sizes are not used because of the varying topography in the study area. Another reason is that, since the Dhundi region exhibits moderate undulating terrains, so from the validation perspective, window sizes which cover ground areas of more than 0.4 km² are excluded from the analysis.

In this regard, the SPA measured FSD ground-truth data at 06:22 hrs January 8, 2016 (IST) was 18.7 cm, and that of the manual record book was 18 cm (section 3.2). Assuming the SPA sensor bias to be 5 cm for the SD, the FSD ground observation of 18 cm is taken as the true value. Accordingly, it is observed from Figure 17 that the 65×65 window leads to the most accurate (94.83%) mean FSD ($\mu_f \approx 18.93$ cm) with a low FSD standard deviation ($\sigma_f \approx 0.1$ cm). The corresponding mean FSWE ($\mu_{fs} \approx 13.25$ mm) and FSWE standard deviation ($\sigma_{fs} \approx 0.07$ mm) are also in concordance (94.84% accuracy) with the ground-truth FSWE of 12.6 mm. However, it should be noted that the axial ratio for the fresh snow particle, $a_x/a_z = 1.5$ is kept as an invariant throughout the entire FSD workflow (Figure 9) and its SA has not been carried out.

Here, the FSD and γ_c values are significantly influenced by the mixed scattering mechanisms exhibited by the ground features (Figure 13(a)) which are being considered for the averaging operation. Moreover, the underlying assumption of a smooth surface in the FSD inversion model does not hold for such rough terrains and consequently, γ_c is reduced (Leinss et al., 2014). Therefore, the FSD SA concludes that even though a sufficiently reliable FSD estimate has been achieved in the Dhundi area, the window sizes need to be adequately adjusted for different multi-temporal SAR images acquired over the same region thereby leading to a more robust parameter optimisation process.

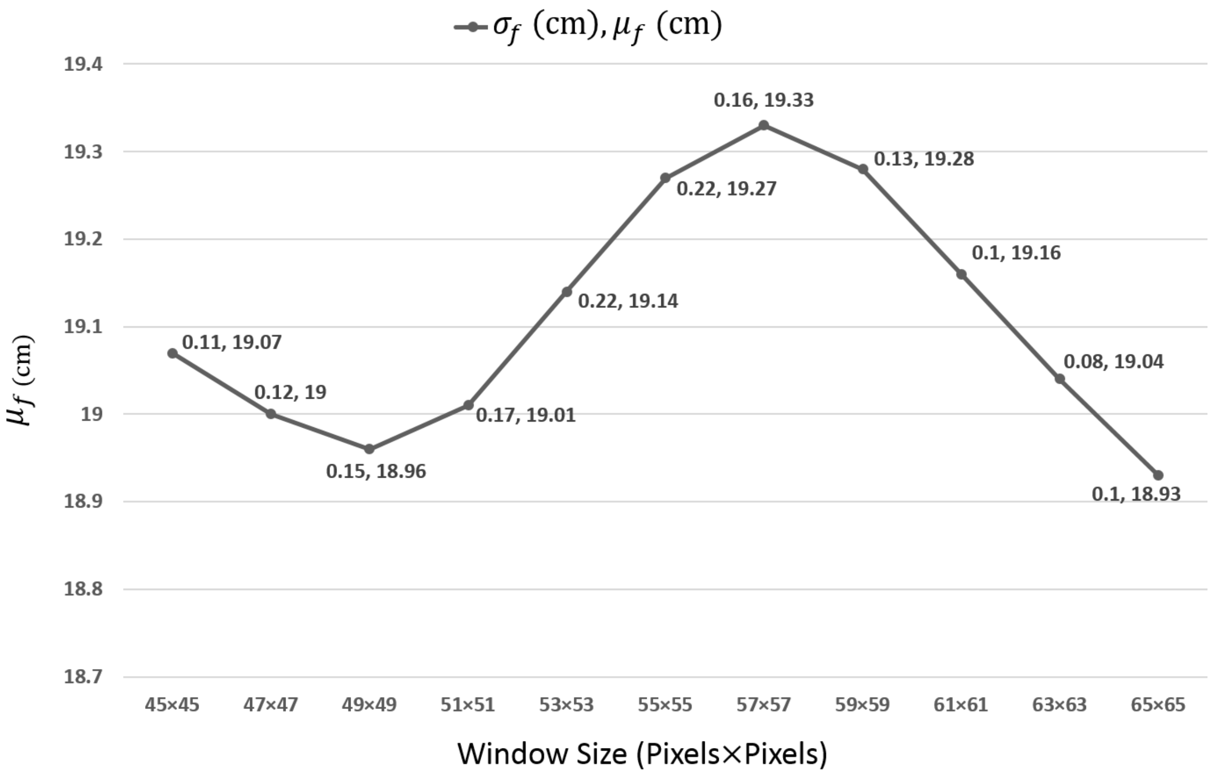

Figure 17: Effect of the window size on the mean and standard deviation of the FSD estimates (rounded to 2 decimal places).

5.2.2. SSD Model Parameters

The SSD inversion model as described from the implementation or methodological perspective in section 4.3 incorporates several user-defined free parameters. Thus, it is necessary to conduct an appropriate SA for the hybrid Pol-InSAR based volumetric height (SSD) retrieval algorithm (Cloude, 2005). In this context, the various model parameters and their optimisation are discussed below.

Volume and Surface Coherence Ensemble Window

The ensemble windows corresponding to the number of looks (L) in Eq. (12) must be suitably chosen so as to maximise both the volume coherence amplitude, $\gamma(\overrightarrow{w_v})$, and the surface coherence amplitude, $\gamma(\overrightarrow{w_s})$. As a result, the SA for these window sizes is an important aspect of this work.

The effects of L on the mean volume coherence amplitude, $\mu_{\gamma(\overrightarrow{w_v})}$, and the mean surface coherence amplitude, $\mu_{\gamma(\overrightarrow{w_s})}$ which are measured by applying the same 3×3 neighbourhood window over Dhundi (section 5.2.1) along with the respective standard deviations, $\sigma_{\gamma(\overrightarrow{w_v})}$ and $\sigma_{\gamma(\overrightarrow{w_s})}$, are displayed in Figure 18. It can be seen that for the executed test cases, with increasing L, there is a general decreasing trend for both these coherences. So, for the SSD estimation, $L = 3$ is chosen even though Cloude (2005) suggests the usage of higher values of L. This is because, $\sigma_{\gamma(\overrightarrow{w_v})} \approx 0.1$ and $\sigma_{\gamma(\overrightarrow{w_s})} \approx 0.18$ are sufficiently small with adequately high $\mu_{\gamma(\overrightarrow{w_v})} \approx 0.67$ and $\mu_{\gamma(\overrightarrow{w_s})} \approx 0.68$. Also, since there is only one validation point for the entire study area, $L = 3$ is justifiable.

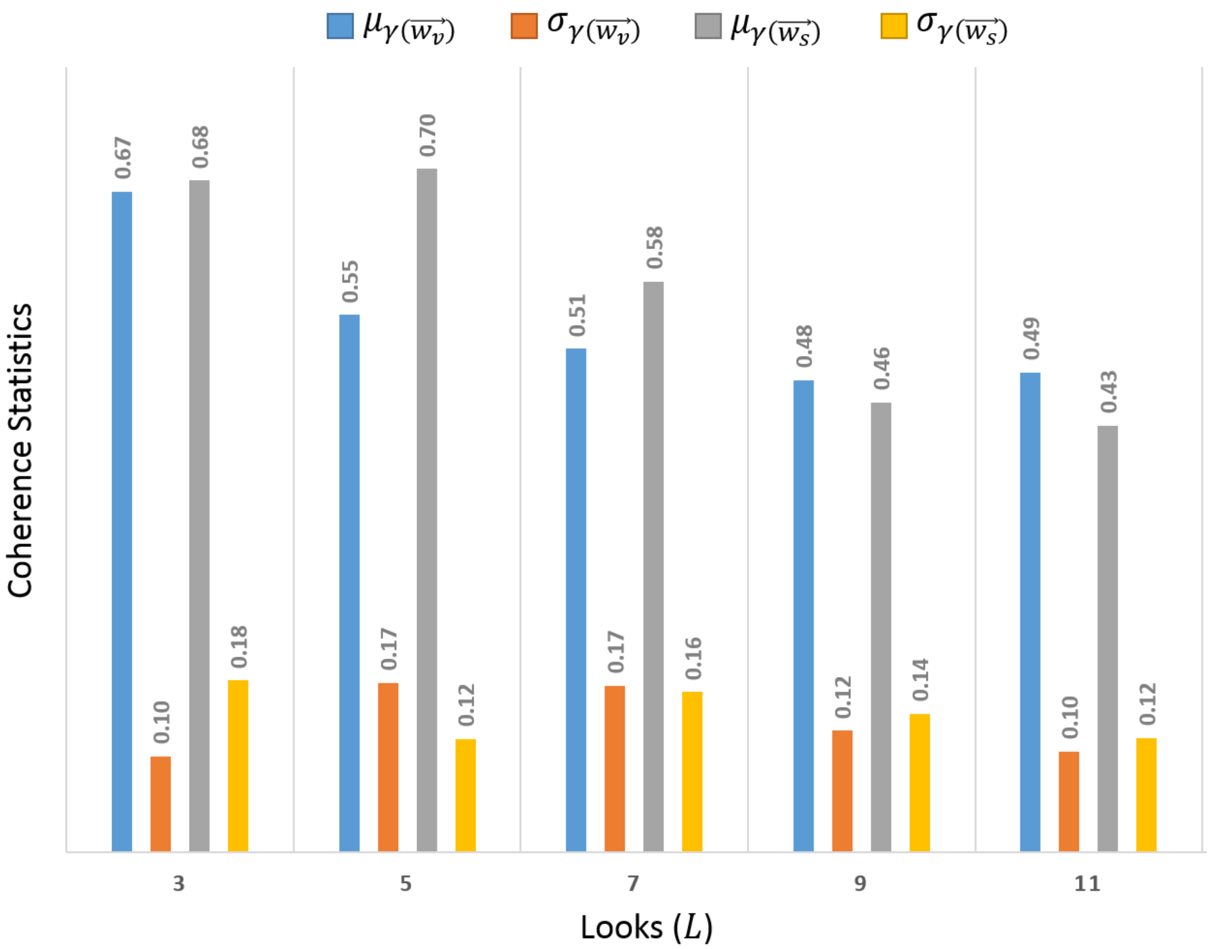

Figure 18: Effect of the number of looks (L) on the volume and surface coherence. All the values are rounded to 2 decimal places.

However, there exist several free parameters in this Pol-InSAR based SSD inversion model (section 4.3) and hence, the volume and surface coherence ensemble windows need to be kept constant ($L = 3$) for the subsequent SA of the other parameters.

Scaling parameters

It has been previously discussed in section 4.3 that there are two scaling parameters involved in the SSD estimation process. These are the vertical wavenumber scaling parameter ($\eta' \in \mathbb{R}^{+}_{>0}$) and the scaling factor ($\eta \in$ [0, 1]) of the hybrid DEM differencing approach (section 2.2.1) developed by Cloude (2010). Here, the SA of only η is carried out and $\eta' = 5$ (section 4.3) is kept constant throughout the entire workflow. Also, the volume coherence threshold, $\tau_v = 0.6$, $L = 3$, ground phase median ensemble filter window (21×21), vertical wavenumber ensemble average window (21×21), and the SSD ensemble average window of size 57×57 are unchanged during this SA.

The monotonically increasing SSD with respect to increasing η are displayed in Figure 19. For $\eta = 0$, the standard DEM differencing technique results in the mean SSD, $\mu_S \approx$ 42.46 cm with the corresponding SSD standard deviation, $\sigma_S \approx$ 0.49 cm. As the SPA measured SSD at 06:22 hrs IST, January 8, 2016, is 54.9 cm, so μ_S is underestimated. Naturally, the mean SSWE, $\mu_{SS} \approx$ 133.76 mm (with SSWE standard deviation, $\sigma_{SS} \approx$ 1.53 mm) is also lower compared to the SPA measured SSWE of 173 mm. Thus, to effectively optimise the volumetric height, η needs to be suitably increased (Cloude, 2005, 2010).

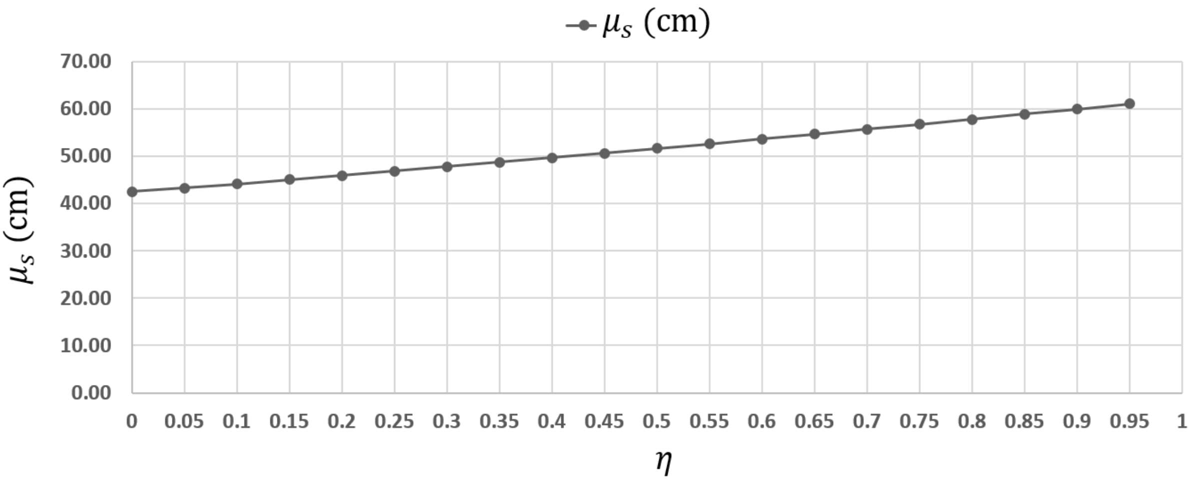

Figure 19: Increasing mean SSD with respect to the scaling parameter η. This SA has been carried out to optimise this parameter to closely match the estimated SSD with the SPA measured ground SSD.

In this context, Cloude (2005) has suggested setting $\eta = 0.4$ for which the accuracy of the estimated tree height is found to be more than 90%. Although by keeping $\eta = 0.4$, $\mu_S \approx$ 49.64 cm ($\sigma_{SS} \approx$ 0.54 cm) is obtained with ~90.42% accuracy, the complexity of the snow microstructure, anisotropy, and length scales (section 2.1.2), necessitates the need for achieving even higher accuracies (Leinss, 2015). Moreover, in the presence of significantly varying hydrometeorological conditions which include high surface roughness and associated uncertainty sources (section 5.1), the volume and surface coherence amplitudes generally do not reach expected values of higher than 0.8 (Cloude, 2005; Kugler et al., 2015). Therefore, with $\eta =$ 0.65, the best SSD and SSWE accuracies of 99.53% ($\mu_S \approx$ 54.64 cm) and 99.48% ($\mu_{SS} \approx$ 172.10 mm) respectively are achieved over Dhundi with low standard deviations ($\sigma_S \approx$ 0.58 cm, $\sigma_{SS} \approx$ 1.82 mm) accounting for high reliability. These results highlight the significance of this scaling parameter η towards controlling the snow structural height variations (Cloude, 2005, 2010) and hence, the robustness of the hybrid DEM differencing model (section 4.3) is verified.

Computing SINC Inverse

In order to test the accuracy of the sinc_π inverse function, sample test data representing the actual inverse, α_r, have been prepared as shown in Table 3. Next, the sinc_π of these data, $\mathrm{sinc}_\pi(\alpha_r)$, is computed which essentially corresponds to the possible $\gamma(\overrightarrow{w_v})$ values. So, the idea of performing SA in this scenario is to check the accuracy of the calculated $\mathrm{sinc}_{\pi C}^{-1}$ (normalised Cloude (2010) approximation given by Eq. (34)) and $\mathrm{sinc}_{\pi S}^{-1}$ (secant method, Eq. (33)) of the $\mathrm{sinc}_\pi(\alpha_r)$ values by comparing these with α_r.

Table 3: Comparison between the normalised Cloude (2010) sinc inverse and the secant sinc inverse methods.

α_r (rad)	$\mathrm{sinc}_\pi(\alpha_r)$	$\mathrm{sinc}_{\pi C}^{-1}$ (rad)	$\mathrm{sinc}_{\pi S}^{-1}$ (rad)
0.1	0.984	0.103	0.100
0.2	0.935	0.206	0.200
0.3	0.858	0.308	0.300
0.4	0.757	0.409	0.400
0.5	0.637	0.509	0.500
0.6	0.505	0.607	0.600
0.7	0.368	0.703	0.700
0.8	0.234	0.798	0.800
0.9	0.109	0.891	0.900

From Table 3 it is observed that the secant method converges exactly (up to 13 decimal places) to the actual α_r while the normalised Cloude (2010) approximation of the sinc_π inverse has some minute errors involved (RMSE $\approx$ 0.02 rad). Similarly, the sinc function is tested (Table 4) where sinc_C^{-1} and sinc_S^{-1} denote the standard Cloude (2010) approximation (Eq. (26)) and the secant method of root finding for the traditional sinc function respectively. Again, the secant method exactly converges (up to 13 decimal places) whereas RMSE $\approx$ 0.02 rad is associated with the sinc_C^{-1}. Here, the computed results shown in Table 3 and Table 4 are rounded to 3 decimal places.

Table 4: Comparison between the traditional Cloude (2010) sinc inverse and the secant sinc inverse methods.

α_r (rad)	$\mathrm{sinc}(\alpha_r)$	sinc_C^{-1} (rad)	sinc_S^{-1} (rad)
0.1	0.998	0.103	0.100
0.2	0.993	0.207	0.200
0.3	0.985	0.31	0.300
0.4	0.974	0.413	0.400
0.5	0.959	0.516	0.500
0.6	0.941	0.618	0.600
0.7	0.92	0.721	0.700
0.8	0.897	0.823	0.800
0.9	0.87	0.925	0.900

Therefore, by performing an SA of the $\mathrm{sinc}_{\pi C}^{-1}$, $\mathrm{sinc}_{\pi S}^{-1}$, sinc_C^{-1}, and sinc_S^{-1}, it is clearly understood that the secant method provides highly accurate results and hence, in this work, $\mathrm{sinc}_{\pi S}^{-1}$ is applied for solving

Eq. (25) wherein the $\text{sinc}_{\pi c}^{-1}(\gamma(\overrightarrow{w_v}))$ value is used as an initial guess to the secant method for fast convergence.

SSD Ensemble Window

Another essential free parameter used in the Pol-InSAR based SSD estimation model (section 4.3) is the SSD ensemble averaging window size. By keeping $\eta = 0.65$, $\eta' = 5$, and other ensemble window sizes constant, the SA has been carried out to observe the SSD variations which are shown in Figure 20. Here, the ensemble windows are the same which have been previously applied for the FSD values (section 5.2.1) so as to appropriately compare the SSD and FSD estimates.

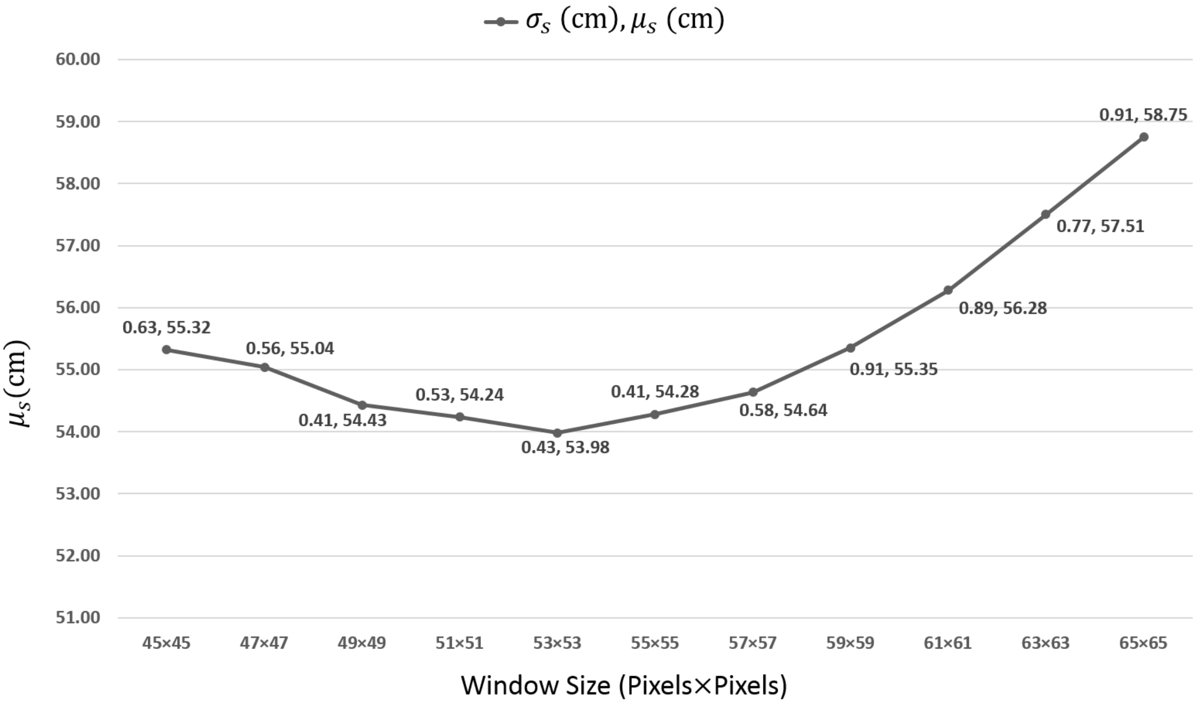

Figure 20: Effect of the ensemble window size on the SSD values.

The graphical representation in Figure 20 shows that when the window size is increased beyond 57×57, the SSD values increase sharply whereas, between the windows 53×53 and 57×57, the values are mostly similar. This could be attributed by the fact that, in mountainous terrains, elevation, and not distance, plays a critical role in controlling the snow accumulation (Liu et al., 2017; Singh et al., 2014, 2017; Thakur et al., 2012). The varying topographical conditions prominently visible in Figure 13 also ascertain that for larger window sizes, the snow depth variability could increase if a nearby mountain also lies within the neighbourhood window. So, considering these aspects, the ensemble window size of 57×57 is selected which results in $\mu_s \approx 54.64$ cm with $\sigma_s \approx 0.58$ cm as discussed in the scaling parameter SA (page 39).

5.2.3. DEM and LIA Error Analysis

During the field visit (section 3.1.2), several DGPS points which had been acquired are used to check the accuracy of the ALOS PALSAR DEM. In essence, the observed errors are then used to analyse the change in the LIA (Eq. (35)) induced by the corrected DEM (the erroneous DEM pixels are replaced by the respective DGPS measurements).

The DEM errors calculated using the Dhundi and Kothi DGPS readings are displayed in Figure 21(a) and the subsequent LIA differences (computed from the corrected and original DEMs) for these points are shown in Figure 21(b). As seen from these graphs, the absolute elevation errors range from 0.08 m to 16.30 m in the Dhundi region, whereas these vary from 0.19 m to 25.32 m in the Kothi area. Accordingly, the RMSE values for the elevation errors are approximately 6.71 m and 8.8 m respectively.

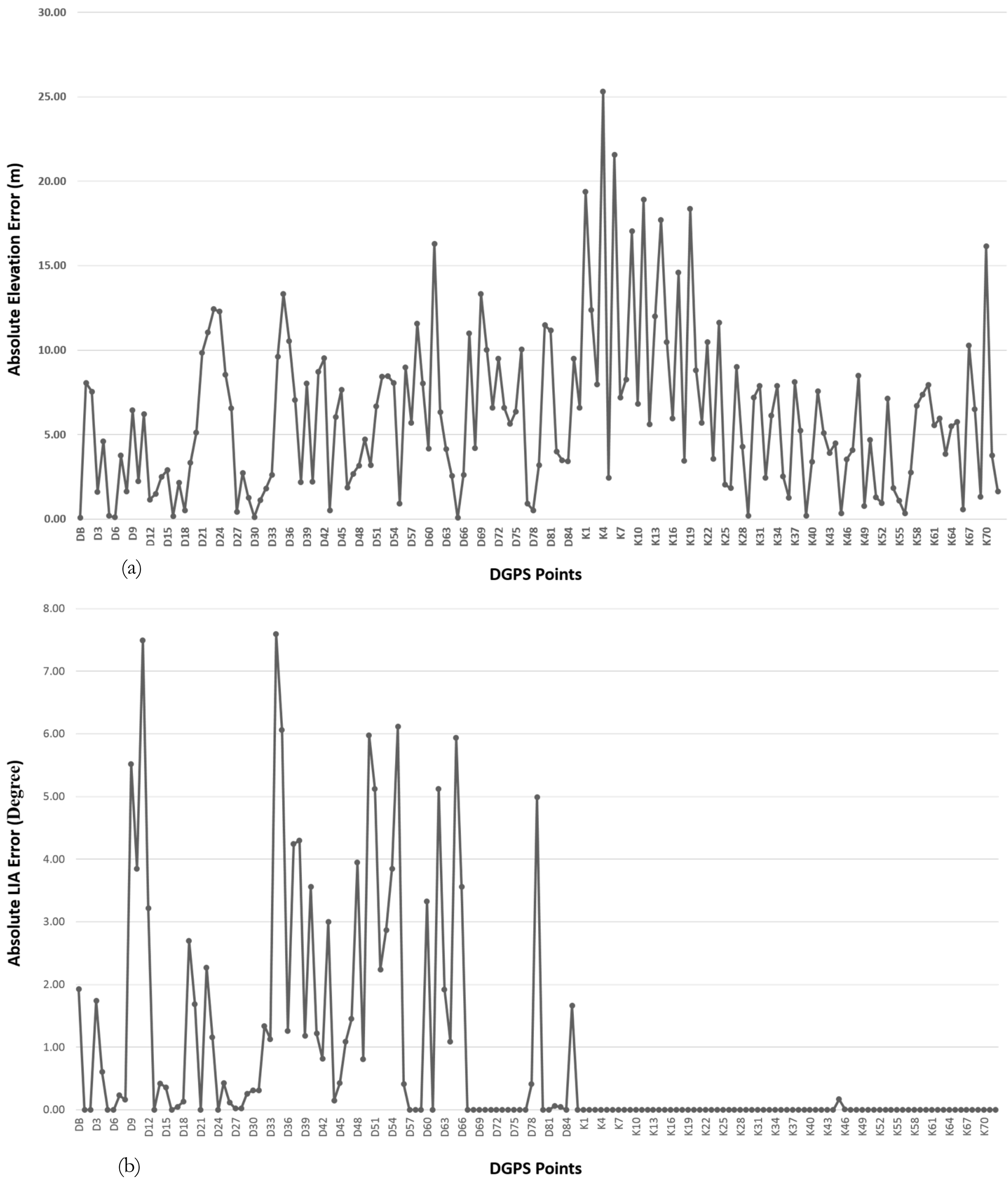

Figure 21: (a) Absolute DEM errors obtained by comparing ALOS PALSAR DEM and the DGPS measurements and (b) observed absolute LIA errors. Here DB is the Dhundi base station point, D1-D86 are acquired in the Dhundi region, and K1-K72 are measured in the Kothi area using the DGPS.

In addition, the LIA varies from 0° to 7.59° (Dhundi) and 0° to 0.17° (Kothi) in these areas with the corresponding RMSE being nearly 2.54° and 0.02°. However, since the LIA is dependent on the slope values (Eq. (35)), the DEM errors do not significantly influence the LIA. Also, in the FSD inversion model and the vertical wavenumber calculation (used in the SSD estimation) given by Eq. (8) and Eq. (17) respectively, the sine ($\sin$) of the LIA is considered. So, the minute changes in the LIA do not strongly affect the FSD and SSD estimates which are obtained after applying sufficient ensemble averaging operation (chapter 4). Evidently, the LIA only changes by about 1.9° near the Dhundi base station and thus, the FSD and SSD results are not exhibiting any sizeable impact from the associated DEM errors.

Therefore, the SA concerning the DEM errors and its propagation highlights that the subsequent LIA errors are not directly governed by the changes in the elevation values, rather the slopes in x and y directions (section 4.4.3) act as the primary error sources. Also, the ALOS PALSAR DEM is sufficiently accurate even in the complex terrains and hence, its usage in the LIA computation is justified. However, it is noteworthy that several of the DGPS measurements had been acquired through the kinematic mode (section 3.1.2) which essentially implies the ground observations themselves to be associated with minor erroneous altitude measurements. This could be the reason behind the low RMSE in the Dhundi area (most points had been surveyed through the static mode) whereas, in the Kothi region, the kinematic mode had to be relied upon due to the inaccessibility or the absence of any suitable locations for setting up the base.

5.2.4. Effects of Terrain Aspect, Elevation, and Slope

Snow accumulation is heavily dependent on the terrain characteristics which include the elevation, slope, and the slope direction or aspect (Grünewald et al., 2014; Jain, Goswami, & Saraf, 2009; Negi et al., 2009; Srinivasulu & Kulkarni, 2004; Zheng et al., 2016). In this context, previous studies focusing on mountainous regions (Grünewald et al., 2014; Jain et al., 2009) have found that the elevation and snow depth are positively correlated till a certain elevation threshold. After this, there is a significant decrease in the SD with increasing elevation values.

Moreover, snow accumulation is not prominent in steep slopes due to the snow redistribution caused by avalanches and wind drift (Grünewald et al., 2014). Freshly fallen snow on top of standing or old snow in the windward slope (mountain side which receives heavy precipitation) are eroded and at the same time deposited to some other slopes which alters the snow cover area (Lehning, Löwe, Ryser, & Raderschall, 2008). In addition, the process of preferential deposition occurring in steep terrains leads to the snow deposition in the leeward side (mountain side which generally receives low precipitation) of a mountain where low snow accumulation is expected (Lehning et al., 2008).

Apart from this, the research conducted by Jain et al. (2009) shows that the terrain aspect significantly controls the snow accumulation in lower altitudes as compared to higher elevation regions. Specifically, in the northwestern Himalayan belt, the maximum snow depth occurs in the northwest (NW) and northeast (NE) slopes due to the low amount of received sunlight particularly during the winters (Jain et al., 2009).

Therefore, as the final step of the SA task, the effects of the aspect, elevation, and slope on the layover, forests, scattering mechanisms (section 5.1), FSD, and SSD are considered, the analysis of which is provided below. Additionally, the fresh snow cover area (FSCA) and standing snow cover area (SSCA) are also computed for all these three terrain attributes.

Aspect

The aspect map of the study area (prepared from the ALOS PALSAR DEM) along with the corresponding histogram are shown in Figure 22(a) and Figure 22(b) respectively. As observed from the histogram, there are significant aspect variations which inherently affect the FSD and SSD estimates.

In order to quantify these effects, the layover, forest, FSCA and SSCA have been computed for each of the slope directions. Moreover, the mean FSD and SSD over each such direction are calculated to check which aspect has the highest amount of snow accumulation and whether these are following similar spatial patterns found by Jain et al. (2009) in their research conducted over the Beas watershed.

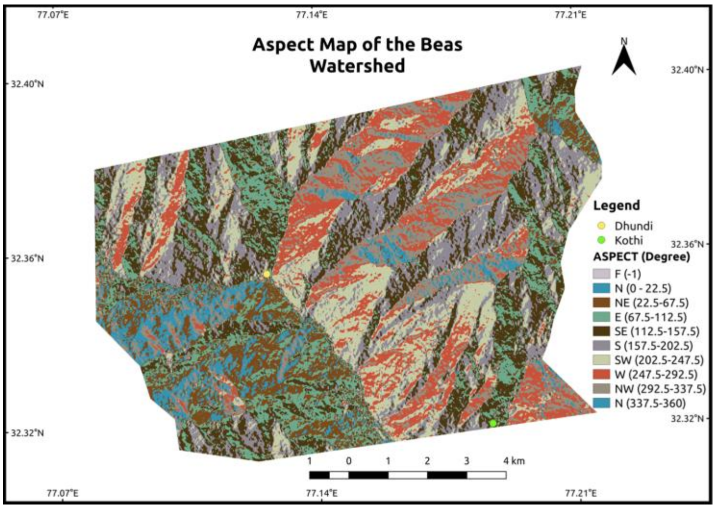

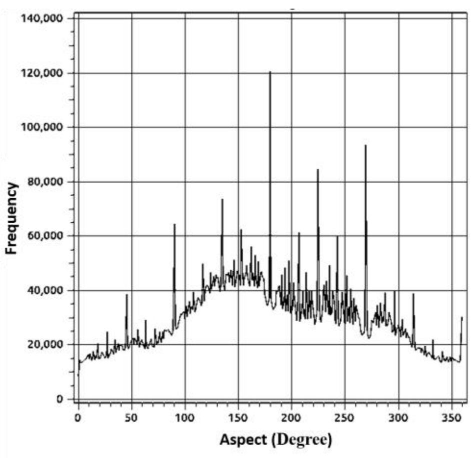

(a) (b)

Figure 22: (a) Aspect map of the Beas watershed and (b) its corresponding histogram generated using QGIS. Here F indicates flat surface if any, the eight slope directions include north (N), northeast (NE), east (E), southeast (SE), south (S), southwest (SW), west (W), and northwest (NW).

The area analysis is shown in Figure 23(a) where, $A_{layover}$, A_{forest}, A_{Zi}, A_f, A_s, and A_{total} denote the layover area (contains shadow as well), forest area, scattering zone (Zi, $\forall i \in [1, 9]$, section 4.4.2) area, FSCA, SSCA, and the total area respectively (January 8, 2016 data). However, since the surface (Z3) and volume scatterings (Z5 and Z8) are used in the FSD and SSD inversion models, the other scattering type areas are not mentioned explicitly. In addition, the mean FSD (μ_{A_f}) and SSD (μ_{A_s}) variations over A_f and A_s respectively are depicted in Figure 23(b).

It is observed from Figure 23(a) that the maximum Bragg surface scattering (Z3) occurs in the south aspect with $A_{Z3} \approx$ 2.14 km² which is about 2% of the entire study area (96.44 km²). Accordingly, the maximum $\mu_{A_f} \approx$ 22.63 cm is also found in this region (Figure 23(b)) which is having $A_{layover} \approx$ 4 km² and $A_{forest} \approx$ 1.6 km² (including overlapping layover and forest regions). However, the maximum $\mu_{A_s} \approx$ 134.91 cm is found to be in the west aspect even though the highest volume scattering area, $A_{Z5} + A_{Z8} \approx$ 4.87 km² is in the SW direction. This could be attributed to the low $A_{Z3} \approx$ 0.22 km² (second lowest after NW) which results in the underestimation of the ground topographic phase (section 4.3) and consequently, μ_{A_s} could potentially be overestimated in the west aspect.

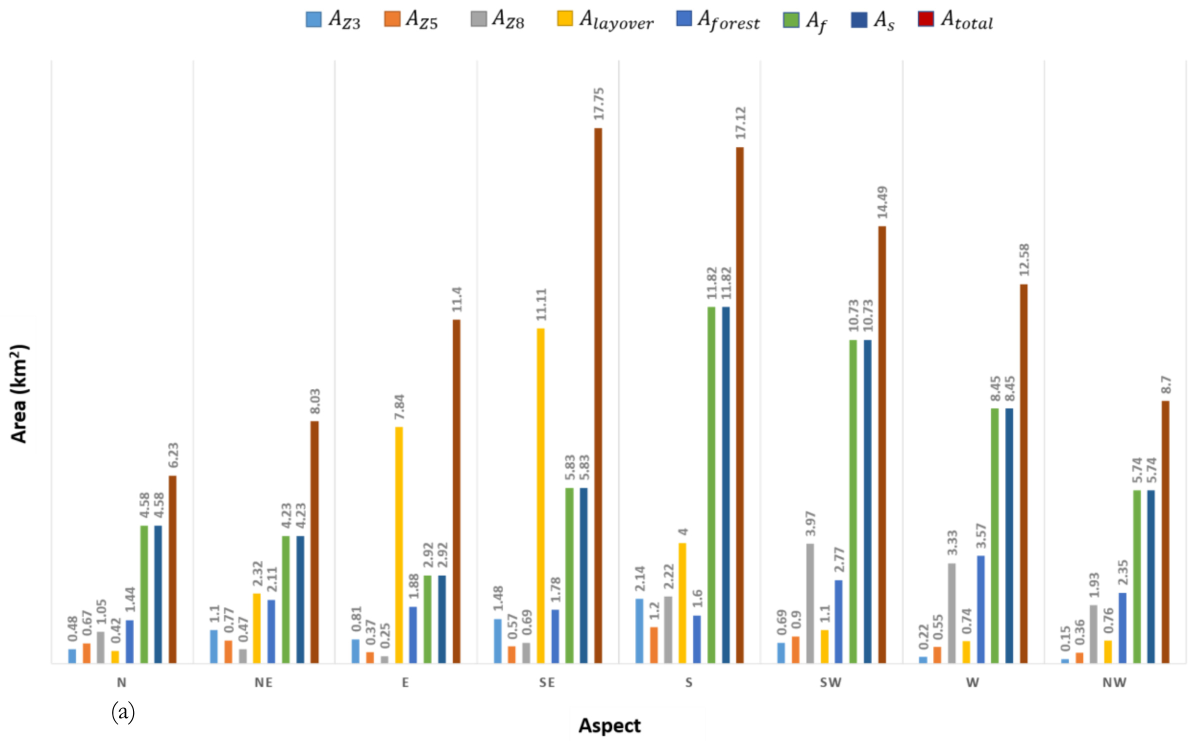

(a)

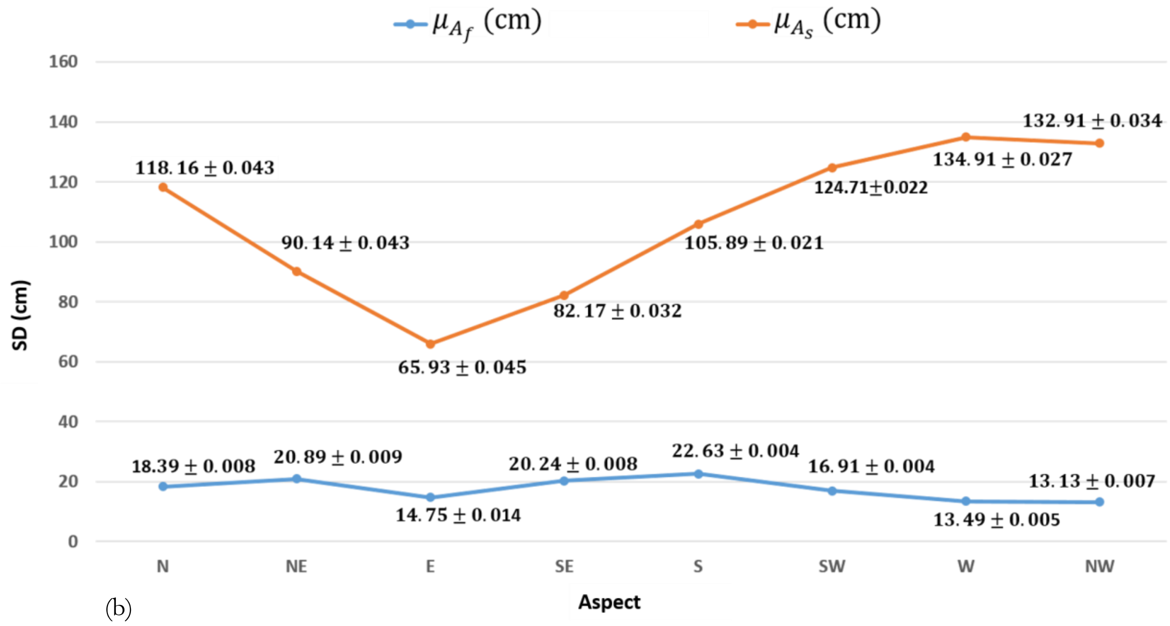

(b)

Figure 23: (a) Layover, forest, surface scattering, volume scattering, and snow cover areas (b) Mean FSD and SSD over different aspects. All the SD estimates are rounded to 2 decimal places. Also, $A_f = A_s$ for all the aspects because only layover and forest masks have been applied (section 4.1). So, the fresh snow and standing snow are always present together. Additionally, the scattering areas include the forested regions, and the forest and layover areas may overlap. Therefore, the total area, A_{total} in (a) cannot be obtained simply by summing up the other areas. In (b), the standard errors (Appendix-C, page 68), rounded to 3 decimal places, are shown to quantify the associated uncertainty.

Furthermore, the highest amount of SSD (total $\mu_{A_s} \approx 341.21$ cm) is present in the northern slopes (N, NE, and NW) which qualitatively agrees with the results obtained by Jain et al. (2009). But in the case of

FSD, the southern slopes (S, SE, and SW) have a total $\mu_{A_f} \approx 59.78$ cm which is slightly higher than the northern slopes (total $\mu_{A_f} \approx 52.41$ cm). One plausible reason for this could be the strong wind drift phenomenon which is commonly observed in the Himalayan terrains (Jain et al., 2009; Lehning et al., 2008). Also, the rugged topography is significantly responsible for reducing the surface coherence (Leinss et al., 2014) and could also be a valid reason for this observation.

Elevation

It has been previously mentioned that the study area comprises of extreme topographic variations which can be qualitatively observed through the ALOS PALSAR DEM shown in Figure 6. The corresponding histogram of the elevation values is provided in Figure 24.

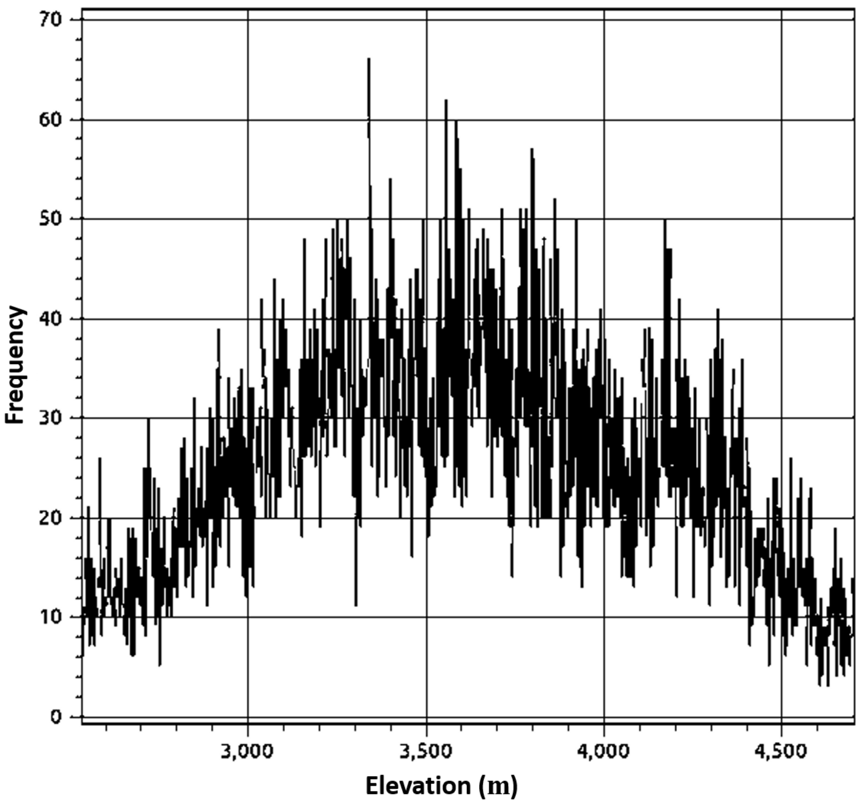

Figure 24: Histogram of the ALOS PALSAR DEM values.

For performing the SA of the layover area, forest area, scattering class areas, FSCA, and SSCA with respect to the elevation changes, six elevation classes— E1(≤2500 m), E2 (2500-3000 m], E3 (3000-3500 m), E4 (3500-4000 m), E5 (4000-4500 m), and E6 (>4500 m) have been defined in a 500 m interval. The area analysis is shown in Figure 25(a) and the FSD and SSD variations are shown in Figure 25(b). Again, $A_f = A_s$ since only forest and layover masks have been applied.

Accordingly, the elevation based SA shows that the maximum $\mu_{A_f} \approx 19.81$ cm and $\mu_{A_s} \approx 115.66$ cm occurs in the E1 and E6 classes respectively. Since E1 and E6 have low ground areas (1.4 km^2 and 4.72 km^2), so the high μ_{A_f} and μ_{A_s} are caused by the less number of pixels which have been averaged. However, the maximum $A_{Z3} \approx 2.1$ km^2 and $A_{Z5} + A_{Z8} \approx 5.64$ km^2 are present in the E3 class even though the total area of E4 (27.73 km^2) is 0.54% higher than that of E3 (27.58 km^2). In addition, the total mask area, $A_{layover} + A_{forest} \approx 15.9$ km^2 is greater in E3 as compared to that of E4 (11.23 km^2).

Despite these masked out regions and lower $A_f = A_s \approx 13.71$ km² when compared to E4 (16.88 km²), $\mu_{A_f} \approx 17.31$ cm and $\mu_{A_s} \approx 110.82$ cm of class E3 closely follows those of E4 (Figure 25(b)). Therefore, E3 could be within the elevation threshold after which the snow accumulation starts decreasing and could also consist of favourable aspect and slope conditions for snow deposition (Jain et al., 2009; Lehning et al., 2008).

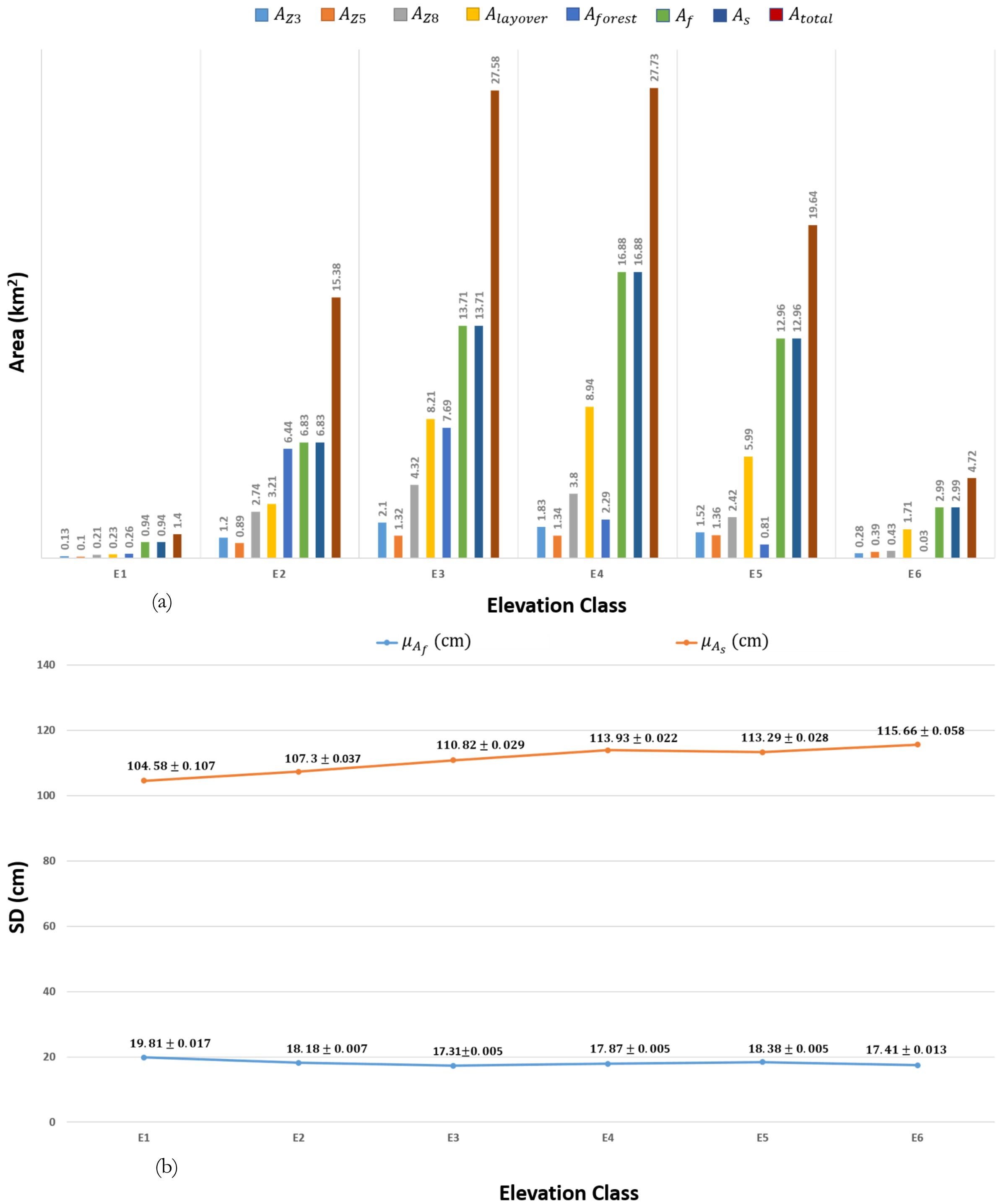

Figure 25: Layover, forest, surface scattering, volume scattering, and snow cover areas (b) Mean FSD and SSD over different elevation classes. All the SD estimates are rounded to 2 decimal places. Also, (a) has been generated in a similar way as that of Figure 23(a). Similarly, the standard errors like those in Figure 23(b) are reported.

Slope

Similar to the aspect, the slope (inclination angle) map in Figure 26(a) is prepared from the ALOS PALSAR DEM. The slope variations can be observed through the histogram depicted in Figure 26(b) which shows that most of the slopes in the region lie within the range 20° and 40°.

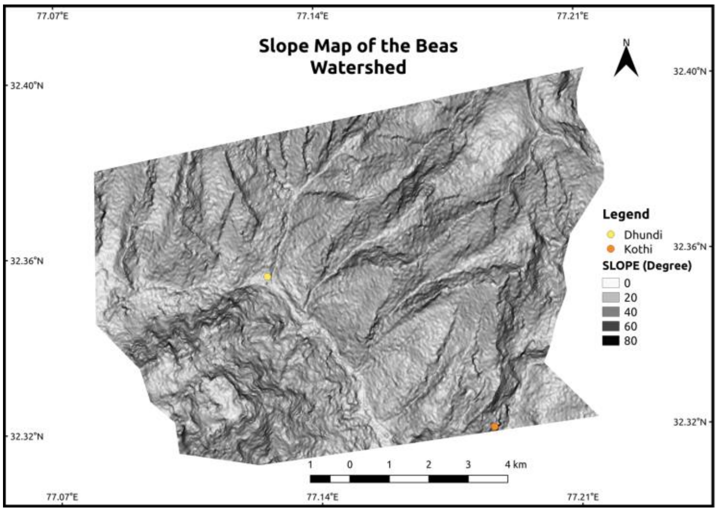

(a)

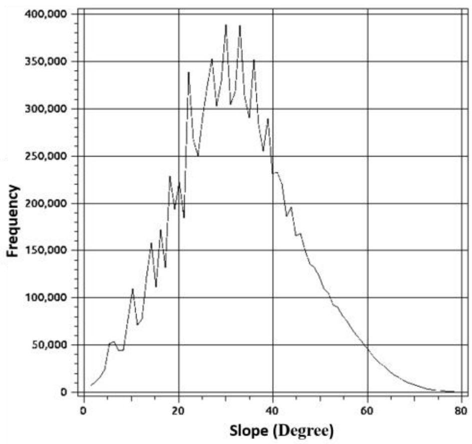

(b)

Figure 26: (a) Slope map of the Beas watershed and (b) its histogram.

In order to carry out the SA of the same variables as done for the aspect and elevation classes, three slope zones have been defined. These are S1 (≤20°), S2 (20°-40°), and S3 (≥40°) which correspond to low, medium, and high slope values. From the area and SD analysis shown in Figure 27(a) and Figure 27(b) respectively, it is seen that even though the total area, A_{total} ≈ 52.32 km² of S2 is substantially larger than that of S1 (A_{total} ≈ 17.36 km²), μ_{A_f} ≈ 20.26 cm of S1 is higher as compared to S2 (μ_{A_f} ≈ 17.51 cm). Additionally, both the surface scattering area, A_{Z3} ≈ 4.23 km² and total volume scattering area, $A_{Z5} + A_{Z8}$ ≈ 11.98 km² are significantly higher in S2. Although, most of the layover (including shadow) and forest areas, $A_{layover} + A_{forest}$ ≈ 21.56 km² (including overlaps) lie in class S2, still, the remaining $A_f = A_s$ ≈ 32.22 km² > A_{total} of S1. Therefore, the FSD estimates in class S1 could either be potentially overestimated or could be attributed to the wind drift and preferential deposition phenomena (Lehning et al., 2008).

Apart from this, the maximum μ_{A_s} ≈ 128.3 cm is present in the S3 class despite the lower A_{Z3} ≈ 1 km² and $A_{Z5} + A_{Z8}$ ≈ 3.01 km² when compared to S2. Again, there is a possibility of overestimation of the SSD estimates in S3. This is because, the total volume scattering percentage in S2 (37.18%) is higher than both S1 (33.64%) and S3 (32.43%) wherein the percentages are calculated based on the number of valid pixel areas (i.e., $A_f = A_s$) of each slope class.

Nevertheless, snow being a highly variable distributed scatterer, slope alone cannot determine whether the FSD and SSD estimates are overestimated or underestimated. Moreover, the effects of the elevation and aspect have not been considered for this particular SA. This could have a significant impact on the area analysis as favourable altitudinal and directional (slope) variations could result in S1 or S3 having higher snow accumulation. In addition, the S2 class needs to be further segregated so that more variations in the areas and SD estimates can be observed. This is another reason why a linear trend is being depicted in Figure 27(b) since most of the study area is falling in the S2 class.

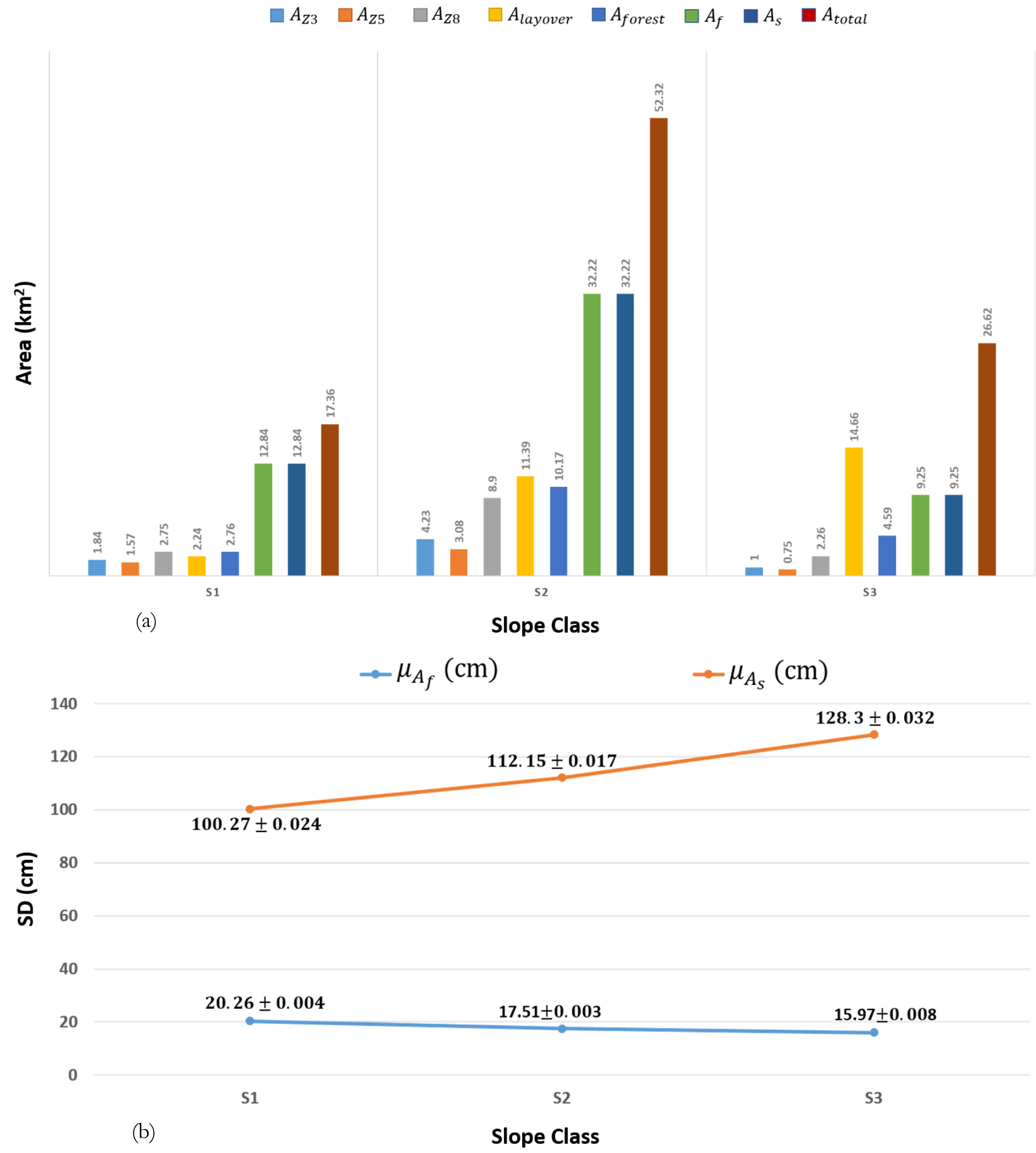

Figure 27: (a) Layover, forest, surface scattering, volume scattering, and snow cover areas (b) Mean FSD and SSD over different slopes. All the SD estimates are rounded to 2 decimal places. Again, the standard errors are displayed like those in Figure 23(b) and Figure 25(b).

Thus, the overall SA which included model parameter tuning or optimisation along with the DEM and LIA error analysis, and terrain characteristics, verifies the fact that in the presence of extreme hydrometeorological conditions, snow depth retrieval becomes a complex process involving several uncertainty sources (section 5.1). In particular, the vertical wavenumber scaling is a subjective process requiring prior knowledge of the maximum SD of the study area (section 4.3). Also, the window sizes are critical for obtaining reliable results (sections 5.2.1 and 5.2.2). Still, sufficient SA has been carried out to address most of the key modelling issues for the FSD and SSD computation.

5.3. Comparative Analysis of the Snow Property Estimates

In order to visually observe the spatial patterns of the FSD and SSD estimates, suitable maps have been prepared which are shown in Figure 28(a) and Figure 28(b) respectively. Additionally, the corresponding histograms are displayed in Figure 30(a) and Figure 30(c). Moreover, the resultant FSWE and SSWE maps are depicted in Figure 29(a) and Figure 29(b) which are computed by multiplying the constant snow densities, $\rho_f = 0.07$ g/cm^3 and $\rho_s = 0.315$ g/cm^3 to the FSD and SSD values respectively. So the SWE maps and histograms in Figure 30(b) and Figure 30(d) exhibit a similar pattern like that of the snow depth estimates.

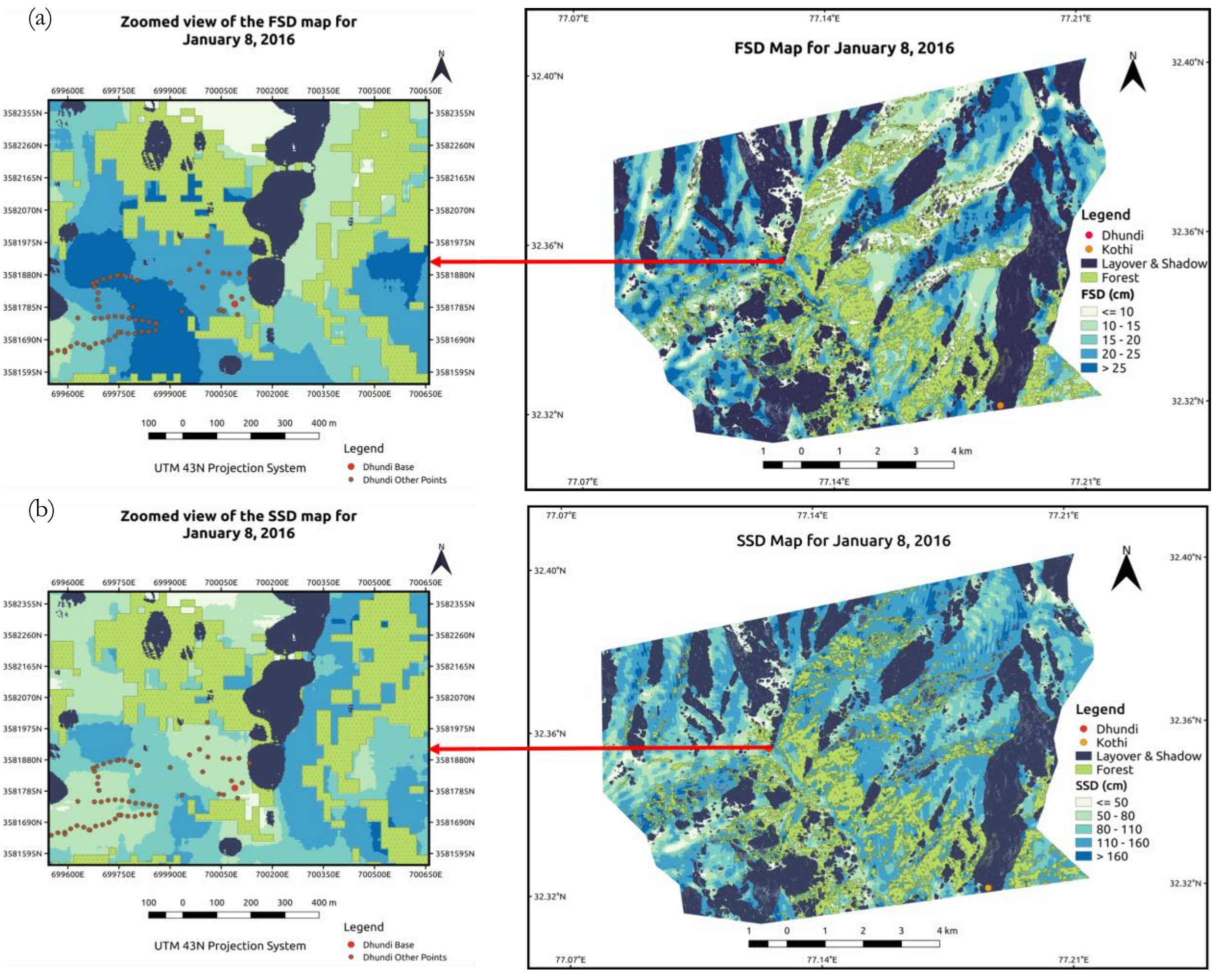

Figure 28: Zoomed views of the (a) FSD map and (b) SSD map for January 8, 2016. Here, the ground points surveyed (section 3.1.2) are shown wherein the closely spaced points have been acquired using the DGPS kinematic mode and fall on the nearby roads in the Dhundi region. The other points including the Dhundi base are measured using the static mode. Since the Kothi area falls in the layover and shadow zone, it is excluded from the zoomed view analysis.

As discussed earlier in sections 5.2.1 and 5.2.2, the optimal FSD and SSD ensemble window sizes are 65×65 and 57×57 respectively. The maps in Figure 28 and Figure 29 show these ensemble averaged estimates wherein $\mu_f \approx 18.93 \pm 5.03$ cm ($\sigma_s \approx 0.1$ cm) and $\mu_s \approx 54.64 \pm 5.19$ cm ($\sigma_s \approx 0.58$ cm) are observed over the 3×3 neighbourhood window surrounding the Dhundi area with the corresponding $\mu_{fs} \approx 13.25 \pm 5.02$ mm ($\sigma_{fs} \approx 0.07$ mm) and $\mu_{ss} \approx 172.10 \pm 5.61$ mm ($\sigma_{ss} \approx 1.82$ mm). Here, the uncertainties are calculated based on the standard error (Appendix-C, page 68) of the estimate and the SPA measurement biases of 5 cm and 5 mm for the SD and SWE have been assumed respectively.

In addition, the histogram analyses for the entire study area show that the overall mean FSD and SSD are 17.90 cm and 112.17 cm respectively wherein the standard deviations are found to be ~6.46 cm and ~30.80 cm. Accordingly, the mean FSWE and SSWE are ~12.12 mm and ~377.81 mm respectively where the associated standard deviations are ~4.46 mm and ~101.55 mm.

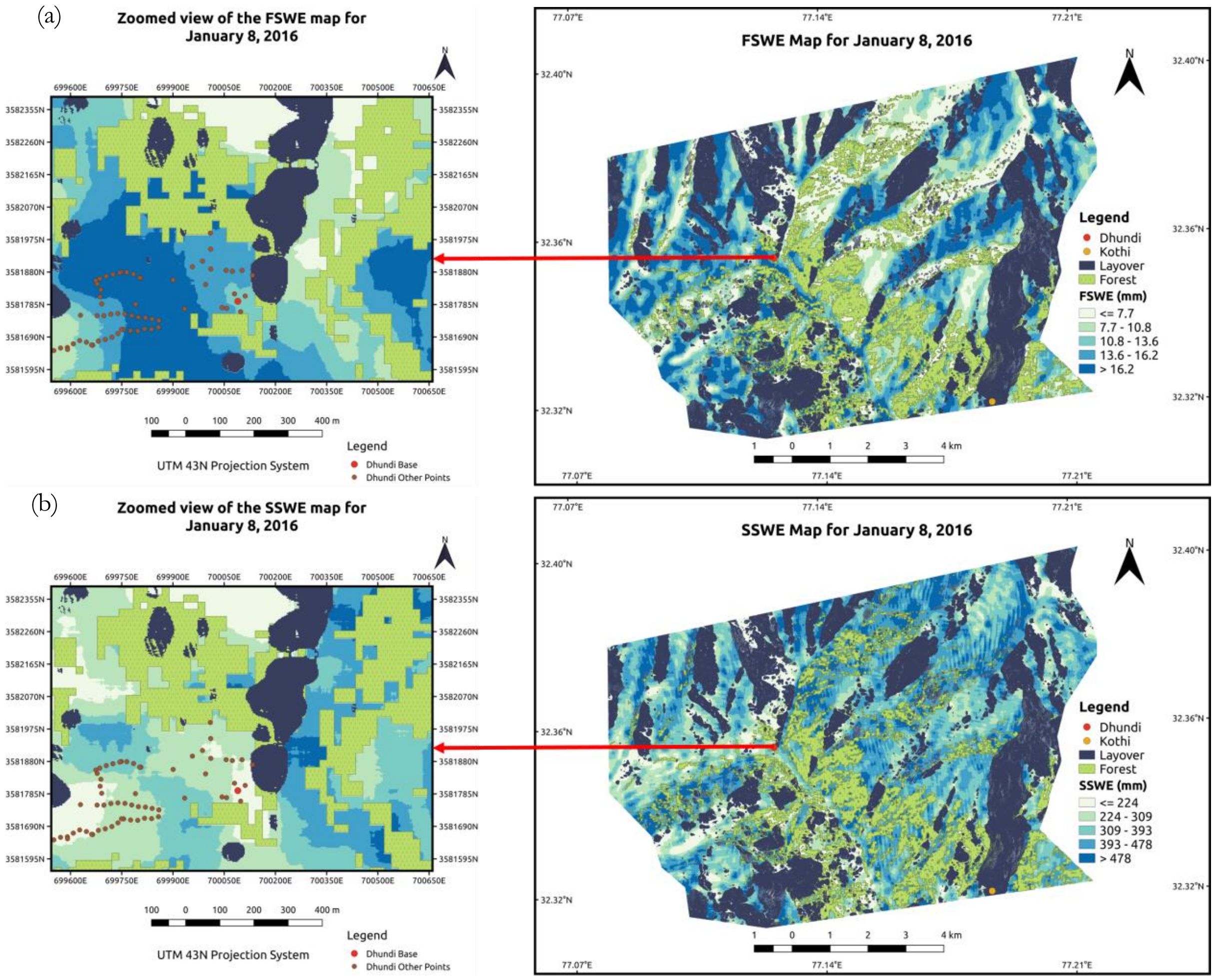

Figure 29: Zoomed views of the (a) FSWE map and (b) SSWE map for January 8, 2016. The ground points in these maps are the exact same ones shown in Figure 28.

The high SSD and SSWE standard deviations for the complete region highlight the extreme topographical conditions present in the study area. These variations can be confirmed from the ground survey (section 3.1.2) where the points (shown in Figure 28 and Figure 29) had been acquired by considering the terrain undulations. Also, the aspect, slope, and elevation significantly influence the FSD and SSD estimates, the details of which have been previously discussed in section 5.2.4.

Apart from this, it can be observed that these estimates are lower in the Dhundi base station area as compared to the surrounding regions. This phenomenon can be attributed to the presence of the human settlements (Figure 7(b)) near the base point and are expected to have less snow accumulation than the natural surroundings. Moreover, the effect of multiple or double bounce scattering (Z4) near the Dhundi base is prominent even during the winter (Figure 13(a)). So, this could effectively reduce the copolar, volume and surface coherences (sections 5.2.1 and 5.2.2) thereby explaining this observation.

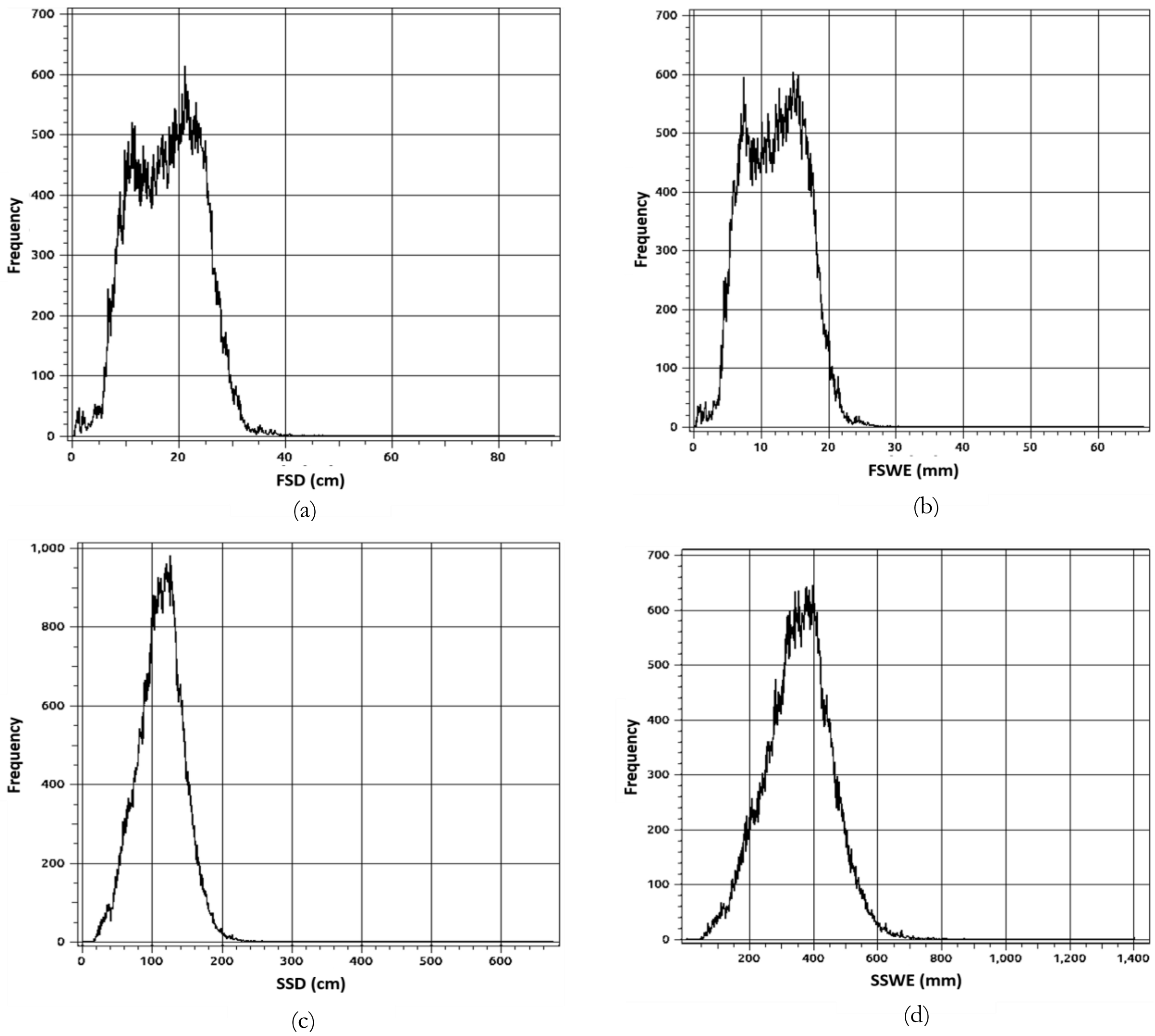

Figure 30: Histograms of (a) FSD, (b) FSWE, (c) SSD, and (d) SSWE.

5.4. Chapter Summary

The results obtained by following the methodological framework (chapter 4) are described in this chapter along with the relevant analysis. At first, the uncertainty assessment results based on the H-α decomposition and unsupervised Wishart classification (section 5.1) have been provided following which a detailed documentation on the SA results (section 5.2) is given. Thereafter, a specific discussion on the comparative analysis of the FSD, FSWE, SSD, and SSWE is put forward in section 5.3. In the next chapter, the answers to the research questions (section 1.4.2) are provided.

6. DISCUSSION

This chapter briefly describes the answers to the research questions related to the specific research objectives (section 1.4).

6.1. DEM Generation from Available Data

In the initial stage of this research, a single DEM had been prepared by selecting the April 15, 2017, bistatic acquisition (Table 2). This dataset was chosen because of the optimum $B_{\perp} = 327.53$ m, the suitable acquisition time (onset of summer), and low Δf_{DC} (which implies low a target shift between the master and the slave images) (Hanssen, 2001). However, the phase unwrapping process (Hanssen, 2001) introduced significant unwrapping errors which are expected in mountainous terrains (Chen & Zebker, 2002). Therefore, a least pixelwise error technique (Appendix-B, page 67) had been applied by considering all the possible DEMs which can be generated from the available datasets (Table 2). Although the errors had been substantially reduced (from about 600 m to 150 m over Dhundi, and over 300 m to less than 1 m over Kothi), still, sufficient level of accuracy had not been achieved.

It is noteworthy that, the SRTM 30 m DEM resampled (bilinear interpolation) to 3 m had been used for checking the accuracy of the computed (stacked) DEM and not the ALOS PALSAR DEM which has been used throughout this work. Thus, the DEM error analysis showed that it is difficult to achieve an adequately accurate DEM over the study area and hence, the reference ALOS PALSAR DEM had to be incorporated. In this context, the effect of different resampling strategies such as cubic convolution or nearest neighbour can also significantly affect the error analysis (Tan et al., 2015). Here, the bilinear interpolation has been used as it is usually the preferred choice for DEM resampling (Rees, 2000).

6.2. FSD Inversion Model

As per the X-ray based micro-CT (μ-CT) scan experiments of the snow microstructure evolution (Riche et al., 2013), it has been revealed that fresh snow typically exhibits horizontally aligned oblate structures. Therefore, the oblate shape is considered to calculate the depolarisation factors from Eq. (5). Regarding the axial ratio, $a_x/a_z = 1.5$ has been kept constant throughout the FSD workflow (section 4.2) which resulted in achieving 94.83% FSD and 94.84% FSWE accuracies over Dhundi. However, the sensitivity analysis of this axial ratio parameter has been separately carried out which is discussed in Appendix-C (page 68).

The ice or snow grains' volume fraction, f_{vol}, is calculated using Eq. (6) which requires the snow density, ρ_{snow}, and ice density, ρ_{ice}. For the FSD estimation, $\rho_{snow} = \rho_f = 0.07$ g/cm^3 is set by referring to the Dhundi manual recordings (section 3.1.2). Here, ρ_f remains constant for the entire study area (section 4.2). Moreover, $\rho_{ice} = 0.917$ g/cm^3 is chosen following relevant literatures in this context (Leinss, 2015; Tedesco, 2015). Therefore, $f_{vol} \approx 0.08$ is used in the FSD inversion model (section 4.2).

6.3. SSD Inversion Model

The hybrid DEM differencing and coherence amplitude inversion model based on the single-baseline Pol-InSAR technique is used for estimating the SSD (section 4.3). This model is chosen because of its less computational complexity and also due to its robustness towards structural variations in the volume scatterer (Cloude, 2005, 2010). The parameter η which effectively controls this volumetric height variation is described in section 5.2.2 (page 39).

Here, the optimisation of the free parameters is carried out through the sensitivity analysis which is explicitly discussed in section 5.2.2. Moreover, this inversion model has been improved by replacing the $\text{sinc}_{\pi_C}^{-1}$ function with the $\text{sinc}_{\pi_s}^{-1}$ function (page 40). Additionally, the ensemble window based filters have been applied on the various SSD model parameters, the details of which are provided in section 5.2.2.

6.4. Comparing FSWE and SSWE

A comparative analysis of the FSD, FSWE, SSD, and SSWE for the January 8, 2016 data is provided in section 5.3. Accordingly, $\mu_{ss} - \mu_{fs} \approx 158.85$ mm over Dhundi which essentially highlights the fact that since standing snow represents the deposited or accumulated (old) snow over time, $\Delta Z_s \geq \Delta Z_f$ will always hold (Leinss, 2015). Here, $\mu_s \approx 54.64 \pm 5.19$ cm and $\mu_f \approx 18.93 \pm 5.03$ cm with $\rho_s = 0.315$ g/cm^3 and $\rho_f = 0.07$ g/cm^3. This leads to the large difference between the obtained SSWE and FSWE.

6.5. Uncertainty Assessment and Sensitivity Analysis

The potential uncertainty sources present in the study area are identified by means of the dual-pol H-α decomposition and unsupervised Wishart classification techniques. This is done by comparing the summer (June 8, 2017) and wintertime (January 8, 2016) Wishart classified images (section 5.1). The analysis shows a substantial change in the scattering mechanisms exhibited by the ground features including forests and river beds (Figure 7). Moreover, the SPA sensor biases of 5 cm and 5 mm for the SD and SWE have been assumed respectively. These along with the standard errors are used to quantify the estimate uncertainties.

As for the sensitivity analysis, the different FSD and SSD model parameters are tested to observe the effects on the FSD and SSD values (sections 5.2.1 and 5.2.2). In addition, the reference ALOS PALSAR DEM errors and their consequent propagation are analysed by observing the change in the LIA values (section 5.2.3). Also, the SSD, SWE, layover (including shadow), forest, and scattering class variations with respect to the terrain aspect, elevation, and slope are sufficiently analysed in section 5.2.4.

6.6. Validation Process

Due to the limited availability of ground-truth measurements, the SD and SWE validation has been performed by considering a 3×3 (81 m^2 ground area) neighbourhood window over Dhundi (section 4.4.1). The Kothi AWS area has been excluded from the validation process because it is lying in the layover and shadow region for the descending pass acquisitions (Figure 28(b)). In this context, the mean and standard deviation of the values within this validation window are considered for effectively addressing the reliability of the FSD, FSWE, SSD, and SSWE estimates (section 5.2).

6.7. Filtering Steps

In order to optimise the ensemble window size, the model results had been iterated over different window sizes (sections 5.2.1 and 5.2.2). This SA showed that for the FSD estimates, ensemble window sizes of 3×3 and 65×65 over the CPD and FSD values respectively ($a_x/a_z = 1.5$) are resulting in high accuracies (94.83% FSD and 94.84% FSWE). As for the SSD estimation, the SA concluded that by keeping the other model parameters constant ($\eta' = 5, \eta = 0.65, \tau_v = 0.6$, coherence windows of 3×3, ground phase, ϕ_{topo}^{w}, and scaled vertical wavenumber, k_z' windows as 21×21), the SSD window of size 65×65 is providing high SSD and SSWE accuracies of nearly 99.53% and 99.48% respectively. Thus, the filtering steps are essential for both these models.

7. CONCLUSIONS AND RECOMMENDATIONS

In this chapter, the relevant conclusions derived from the overall research are provided. Additionally, the recommendations regarding future studies related to this thesis have been discussed succinctly.

7.1. Conclusions

The primary focus of this research lies in estimating the snow depth using which the snow water equivalent has been measured. Here, two different types of snow have been considered— freshly fallen (new) snow and standing (old) snow. In order to compute the FSD, the CPD method has been applied (section 4.2) on the January 8, 2016, TSX-TDX CoSSC bistatic dataset (Table 2) acquired over the Beas watershed, northwestern Himalayas (Figure 6). Additionally, the hybrid DEM differencing and coherence amplitude inversion algorithm based on the single-baseline Pol-InSAR technique has been utilised to estimate the SSD for the same dataset (section 4.3). Also, the corresponding FSWE and SSWE are obtained by multiplying constant fresh and standing snow densities.

Due to the complex hydrometeorological and topographical conditions of the study area (section 3.1.1), significant uncertainty sources are present. These include the forests, boulders, highly rough surfaces, and human settlements (Figure 7) which substantially reduce the surface and volume scattering coherences required to estimate the snow depths with adequate accuracy (section 4.4). Moreover, the limited ground-truth data availability has always been a major challenge from the onset of this work (section 3.2). Apart from this, the SAR data are affected by layover, shadowing and foreshortening in mountainous terrains and hence, these errors are inherently propagated through the subsequent processing steps. Furthermore, to resolve the topography induced terrain undulation effect on the radar incidence angle, the LIA is used in SAR remote sensing studies carried out in mountain regions (section 2.2). However, an accurate DEM is necessary to compute the LIA which consequently leads to further error propagation (section 1.3). In short, these are the main concerns involved in this work.

Therefore, the uncertainty assessment and sensitivity analysis have been extensively conducted to address these research problems appropriately. By performing the dual-pol H-α decomposition and unsupervised Wishart classification, the different scattering mechanisms have been identified and linked with their potential sources on the ground (section 5.1). Additionally, the summer (June 8, 2017) and wintertime (January 8, 2016) comparisons of the Wishart classified images explicitly showcase the significant changes in the scattering properties in the presence of snow during the winters. It is observed that, the surface scattering (Z3) has greatly reduced near the river bed (Figure 7(c)) which essentially suggests that the PolSAR CPD method will potentially result in underestimated values. However, due to this reduced Z3 scattering, the topographic or ground phase required in the SSD inversion model would also be underestimated and could result in the overestimation of the SSD measurements. Hence, the quantitative comparative analysis of the scattering mechanism changes (Figure 14) enables to suitably interpret the variations in the final FSD and SSD maps (section 5.3).

Regarding the SA, the changes in the layover (including shadow), forest, scattering classes, fresh snow, and standing snow areas corresponding to the aspect, elevation, and slope are considered. Also, the variations in the mean snow depths are calculated with respect to these terrain attributes (section 5.2.4). In addition, the different FSD and SSD user-defined model parameters are thoroughly tested for optimality. These optimisation steps are driven by means of appropriate accuracy assessments via a 3×3 validation window over Dhundi. Notably, the estimates exhibit a strong dependence on the ensemble window based averaging which is a mandatory processing step common to both these models. Moreover, the reference ALOS PALSAR DEM errors are computed using the acquired DGPS measurements during the field visit to Dhundi and Kothi. However, it is observed that the elevation errors do not significantly alter the LIA values which are in turn, required for the FSD and SSD inversion models (section 5.2.3).

Thus, the novelty of this research lies in suitably modifying and ultimately improving (page 40) the hybrid Pol-InSAR model to estimate the SSD which is new in the context of cryospheric studies. Additionally, the PolSAR CPD method for FSD retrieval has been tested for the first time in the presence of extreme topographically varying conditions. Although the FSD and SSD ground-truth measurements from only the Dhundi station had been available, the high accuracies of 94.83% and 99.53% respectively imply that these improved models work sufficiently well under the complex hydrometeorological situations.

7.2. Recommendations

One of the main limitations of this work is the high subjectivity of the free parameters involved in the FSD and SSD inversion models. For example, the vertical wavenumber scaling parameter, η', which is set to 5 for the SSD estimation (section 4.3), can significantly alter the results because the associated ambiguity height, $h'_{2\pi}$, is almost equal to the maximum height of the volume scatterer (snow). Also, the prior knowledge of this maximum snow depth, $\Delta Z_{s,max}$, is seemingly impossible to obtain without any appropriate field survey. So, it is recommended to use the multi-baseline Pol-InSAR technique (Cloude, 2010) wherein k_z can be simulated (instead of scaling by η') after an appropriate accuracy assessment (S. Kumar et al., 2017). However, this approach will only be feasible if there are adequately sampled (both spatially and temporally) SD field measurements.

Similarly, the effect of different window shapes (square or rectangular) and sizes can be considered for the ensemble averaging operation. This sort of sensitivity analysis will help in deciding optimal window structures separately for each model. Moreover, it is recommended to apply scattering mechanism based masks in conjunction with snow masks prepared from the high resolution optical datasets such as those provided by Sentinel-2 (Zhu, Wang, & Woodcock, 2015). Additionally, the prior classification of the dry and wet snow including the preparation of snow cover maps (Leinss et al., 2018; Thakur et al., 2017; Zhu et al., 2015) as necessary preprocessing steps will certainly improve the uncertainty assessment process.

Apart from this, it is noteworthy that, although the aspect plays a critical role in controlling the snow accumulation variations, it cannot be solely used to justify the spatial behaviour of snow in the complex alpine terrains. As a result, the elevation and slope need to be used in conjunction with the aspect to address the snow variability. However, in this thesis, these three terrain attributes are individually used to assess the effects on the FSD and SSD estimates. Hence, the combined analysis of these is recommended in future studies in this regard.

Additionally, the use of the newer multi-temporal high resolution L-band datasets acquired by the upcoming SAR missions (Krieger et al., 2016; Rosen et al., 2017) is recommended to further verify and validate these models. Moreover, radar altimeters such as the Ka-band InSAR altimeter could potentially improve the SD and SWE estimates, and could also be used for operational snow depth monitoring on a large-scale (Hensley, Moller, Oveisgharan, Michel, & Wu, 2016; Kim, Gatebe, Hall, & Kang, 2018; Moller et al., 2011; Speziali et al., 2018).

In this work, due to the time constraints, only one dataset (January 8, 2016, Table 2) has been used for analysis. Instead, if a full scale time series analysis is performed, then the robustness of the SSD and FSD retrieval models can be checked. Furthermore, the polarisation weight vectors (Table 1) can be optimised specifically to the data which will eventually improve the accuracy of the estimates (Cloude, 2005, 2010). Also, since the assumption of a constant snow density over such undulating terrains is impractical (page 20), the snow densities need to be computed gridwise (or if possible, pixelwise) by using hydrological modelling approaches (Bartelt & Lehning, 2002; Liang, Lettenmaier, Wood, & Burges, 1994). The snow densities can also be estimated from the PolSAR based techniques which are in practice (Singh et al., 2017; Thakur et al., 2012). Finally, appropriate statistical significance testing needs to be carried out to quantify further the uncertainties associated with the FSD and SSD estimates.

LIST OF REFERENCES

Abe, T., Yamaguchi, Y., & Sengoku, M. (1990). Experimental study of microwave transmission in snowpack. *IEEE Transactions on Geoscience and Remote Sensing*, *28*(5), 915–921. https://doi.org/10.1109/36.58981

Anderton, S. P., White, S. M., & Alvera, B. (2004). Evaluation of spatial variability in snow water equivalent for a high mountain catchment. *Hydrological Processes*, *18*(3), 435–453. https://doi.org/10.1002/hyp.1319

Balss, U., Breit, H., Duque, S., Fritz, T., & Rossi, C. (2012). *CoSSC Generation and Interferometric Considerations (TD-PGS-TN-3129). Remote Sensing Institute, DLR*. Oberpfaffenhofen, Germany. Retrieved from https://tandemx-science.dlr.de/pdfs/TD-PGS-TN-3129_CoSSCGenerationInterferometricConsiderations_1.0.pdf

Barry, R. G., & Gan, T. Y. (2011). *The Global Cryosphere: Past, Present and Future*. Cambridge: Cambridge University Press. https://doi.org/10.1017/CBO9780511977947

Bartelt, P., & Lehning, M. (2002). A physical SNOWPACK model for the Swiss avalanche warning. *Cold Regions Science and Technology*, *35*(3), 123–145. https://doi.org/10.1016/S0165-232X(02)00074-5

Bohleber, P., Wagner, N., & Eisen, O. (2012). Permittivity of ice at radio frequencies: Part II. Artificial and natural polycrystalline ice. *Cold Regions Science and Technology*, *83–84*, 13–19. https://doi.org/10.1016/j.coldregions.2012.05.010

Brunner, D. (2009). *Advanced Methods For Building Information Extraction From Very High Resolution SAR Data To Support Emergency Response (Doctoral Thesis)*. Trento: University of Trento. Retrieved from http://eprints-phd.biblio.unitn.it/233/1/PHD_Thesis_Dominik_Brunner.pdf

Bryan, A. B., & Sanders, I. C. (1928). The Dielectric Constant of Air at Radio Frequencies. *Physical Review*, *32*(2), 302–310. https://doi.org/10.1103/PhysRev.32.302

Buchner, R., Barthel, J., & Stauber, J. (1999). The dielectric relaxation of water between 0°C and 35°C. *Chemical Physics Letters*, *306*(1–2), 57–63. https://doi.org/10.1016/S0009-2614(99)00455-8

Budillon, A., Pascazio, V., & Schirinzi, G. (2008). Multichannel Along-Track Interferometric SAR Systems: Moving Targets Detection and Velocity Estimation. *International Journal of Navigation and Observation*, *2008*, 1–16. https://doi.org/10.1155/2008/310656

Chen, C. W., & Zebker, H. A. (2002). Phase unwrapping for large SAR interferograms: Statistical Segmentation and Generalized Network Models. *IEEE Transactions on Geoscience and Remote Sensing*, *40*(8), 1709–1719. https://doi.org/10.1109/TGRS.2002.802453

Cheney, E. W., & Kincaid, D. R. (2012). Nonlinear equations. In *Numerical Mathematics and Computing* (7th ed., pp. 114–150). Boston, USA: Cengage Learning.

Cloude, S. R. (2005). *POL-InSAR training course*. Retrieved from https://earth.esa.int/polsarpro/Manuals/1_Pol-InSAR_Training_Course.pdf

Cloude, S. R. (2010). *Polarisation: Applications in Remote Sensing*. New York: Oxford University Press. https://doi.org/10.1093/acprof:oso/9780199569731.001.0001

Deems, J. S., Fassnacht, S. R., & Elder, K. J. (2006). Fractal Distribution of Snow Depth from Lidar Data. *Journal of Hydrometeorology*, *7*(2), 285–297. https://doi.org/10.1175/JHM487.1

Deems, J. S., Painter, T. H., & Finnegan, D. C. (2013). Lidar measurement of snow depth: a review. *Journal of Glaciology*, *59*(215), 467–479. https://doi.org/10.3189/2013JoG12J154

Dierking, W. (2013). Sea Ice Monitoring by Synthetic Aperture Radar. *Oceanography*, *26*(2), 101–111. https://doi.org/10.5670/oceanog.2013.33

Ellison, W. J., Lamkaouchi, K., & Moreau, J.-M. (1996). Water: a dielectric reference. *Journal of Molecular Liquids*, *68*(2–3), 171–279. https://doi.org/10.1016/0167-7322(96)00926-9

ESA. (2018). SNAP. Retrieved February 7, 2019, from http://step.esa.int/main/toolboxes/snap/

Esmaeily-Gazkohani, A., Granberg, H. B., & Gwyn, Q. H. J. (2010). Repeat-pass cross-track interferometric SAR to measure dry snow water equivalent and depth. *Canadian Journal of Remote Sensing*, *36*(sup2), S316–S326. https://doi.org/10.5589/m10-064

Evans, S. (1965). Dielectric Properties of Ice and Snow- A Review. *Journal of Glaciology*, *5*(42), 773–792. https://doi.org/10.3189/S0022143000018840

Ferretti, A., Monti-Guarnieri, A., C., P., & Rocca, F. (2007). *InSAR Principles: Guidelines for SAR Interferometry Processing and Interpretation*. (K. Fletcher, Ed.). Noordwijk, The Netherlands: ESA Publications. Retrieved from https://www.esa.int/esapub/tm/tm19/TM-19_ptA.pdf

Goodman, J. W. (2007). *Speckle phenomena in optics: Theory and applications*. Englewood, Colo: Roberts & Co.
Grünewald, T., Bühler, Y., & Lehning, M. (2014). Elevation dependency of mountain snow depth. *The Cryosphere*, *8*(6), 2381–2394. https://doi.org/10.5194/tc-8-2381-2014
Guneriussen, T., Høgda, K. A., Johnsen, H., & Lauknes, I. (2001). InSAR for estimation of changes in snow water equivalent of dry snow. *IEEE Transactions on Geoscience and Remote Sensing*, *39*(10), 2101–2108. https://doi.org/10.1109/36.957273
Hajnsek, I., Kugler, F., Lee, S.-K., & Papathanassiou, K. P. (2009). Tropical-Forest-Parameter Estimation by Means of Pol-InSAR: The INDREX-II Campaign. *IEEE Transactions on Geoscience and Remote Sensing*, *47*(2), 481–493. https://doi.org/10.1109/TGRS.2008.2009437
Haldar, D., Rana, P., Yadav, M., Hooda, R. S., & Chakraborty, M. (2016). Time series analysis of co-polarization phase difference (PPD) for winter field crops using polarimetric C-band SAR data. *International Journal of Remote Sensing*, *37*(16), 3753–3770. https://doi.org/10.1080/01431161.2016.1204024
Hallikainen, M., Ulaby, F., & Van Deventer, T. (1987). Extinction Behavior of Dry Snow in the 18-to 90-GHz Range. *IEEE Transactions on Geoscience and Remote Sensing*, *GE-25*(6), 737–745. https://doi.org/10.1109/TGRS.1987.289743
Hanssen, R. F. (2001). *Radar Interferometry - Data Interpretation and Error Analysis* (Vol. 2). Dordrecht: Kluwer Academic Publishers. https://doi.org/10.1007/0-306-47633-9
Hensley, S., Moller, D., Oveisgharan, S., Michel, T., & Wu, X. (2016). Ka-Band Mapping and Measurements of Interferometric Penetration of the Greenland Ice Sheets by the GLISTIN Radar. *IEEE Journal of Selected Topics in Applied Earth Observations and Remote Sensing*, *9*(6), 2436–2450. https://doi.org/10.1109/JSTARS.2016.2560626
Hoen, E. W., & Zebker, H. A. (2000). Penetration depths inferred from interferometric volume decorrelation observed over the Greenland Ice Sheet. *IEEE Transactions on Geoscience and Remote Sensing*, *38*(6), 2571–2583. https://doi.org/10.1109/36.885204
Jain, S. K., Goswami, A., & Saraf, A. K. (2009). Role of elevation and aspect in snow distribution in Western Himalaya. *Water Resources Management*, *23*(1), 71–83. https://doi.org/10.1007/s11269-008-9265-5
JetBrains. (2018). PyCharm Documentation. Retrieved February 7, 2019, from https://www.jetbrains.com/pycharm/documentation/index.html
Jones, E., Oliphant, E., & Peterson, P. (2001). SciPy: Open Source Scientific Tools for Python. Retrieved February 12, 2019, from http://www.scipy.org/
Judson, A., & Doesken, N. (2000). Density of Freshly Fallen Snow in the Central Rocky Mountains. *Bulletin of the American Meteorological Society*, *81*(7), 1577–1587. https://doi.org/10.1175/1520-0477(2000)081<1577:DOFFSI>2.3.CO;2
Kampes, B., & Usai, S. (1999). Doris: the Delft Object−oriented Radar Interferometric Software. In *Proceedings of the 2nd International Symposium on Operationalization of Remote Sensing* (pp. 1–4). Enschede, The Netherlands. Retrieved from http://citeseerx.ist.psu.edu/viewdoc/download?doi=10.1.1.46.1689&rep=rep1&type=pdf
Kim, E. J., Gatebe, C. K., Hall, D. K., & Kang, D. H. (2018). *NASA's SnowEx Campaign and Measuring Global Snow from Space (GSFC-E-DAA-TN55784)*. Pyeongchang, Republic of Koraa: NASA. Retrieved from https://ntrs.nasa.gov/search.jsp?R=20180005187
Krieger, G., Moreira, A., Zink, M., Hajnsek, I., Huber, S., Villano, M., … Bewick, C. (2016). Tandem-L: Main results of the phase a feasibility study. In *2016 IEEE International Geoscience and Remote Sensing Symposium (IGARSS)* (pp. 2116–2119). IEEE. https://doi.org/10.1109/IGARSS.2016.7729546
Kugler, F., Lee, S.-K., Hajnsek, I., & Papathanassiou, K. P. (2015). Forest Height Estimation by Means of Pol-InSAR Data Inversion: The Role of the Vertical Wavenumber. *IEEE Transactions on Geoscience and Remote Sensing*, *53*(10), 5294–5311. https://doi.org/10.1109/TGRS.2015.2420996
Kumar, S., Khati, U. G., Chandola, S., Agrawal, S., & Kushwaha, S. P. S. (2017). Polarimetric SAR Interferometry based modeling for tree height and aboveground biomass retrieval in a tropical deciduous forest. *Advances in Space Research*, *60*(3), 571–586. https://doi.org/10.1016/j.asr.2017.04.018
Kumar, V., & Venkataraman, G. (2011). SAR interferometric coherence analysis for snow cover mapping in the western Himalayan region. *International Journal of Digital Earth*, *4*(1), 78–90. https://doi.org/10.1080/17538940903521591

Lee, J.-S., & Pottier, E. (2009). *Polarimetric Radar Imaging: From Basics to Applications*. Boca Raton, Florida, USA: CRC Press. Retrieved from https://www.taylorfrancis.com/books/9781420054972
Lee, J.-S., Schuler, D. L., & Ainsworth, T. L. (2000). Polarimetric SAR data compensation for terrain azimuth slope variation. *IEEE Transactions on Geoscience and Remote Sensing*, *38*(5), 2153–2163. https://doi.org/10.1109/36.868874
Lehning, M., Löwe, H., Ryser, M., & Raderschall, N. (2008). Inhomogeneous precipitation distribution and snow transport in steep terrain. *Water Resources Research*, *44*(7). https://doi.org/10.1029/2007WR006545
Lei, Y., Siqueira, P., & Treuhaft, R. (2016). A dense medium electromagnetic scattering model for the InSAR correlation of snow. *Radio Science*, *51*(5), 461–480. https://doi.org/10.1002/2015RS005926
Leica Geosystems AG. (2012). *Leica GS10/GS15 User Manual (772916-4.1.0en). Leica Geosystems AG*. Heerbrugg, Switzerland. Retrieved from http://www.surveyequipment.com/PDFs/Leica_Viva_GS10_GS15_User_Manual.pdf
Leinss, S. (2015). *Depth, anisotropy, and water equivalent of snow estimated by radar interferometry and polarimetry (Doctoral thesis)*. Zürich: ETH-Zürich. https://doi.org/10.3929/ethz-a-010603517
Leinss, S., Antropov, O., Vehvilainen, J., Lemmetyinen, J., Hajnsek, I., & Praks, J. (2018). Wet Snow Depth from Tandem-X Single-Pass Insar Dem Differencing. In *IGARSS 2018 - 2018 IEEE International Geoscience and Remote Sensing Symposium* (pp. 8500–8503). IEEE. https://doi.org/10.1109/IGARSS.2018.8518661
Leinss, S., Parrella, G., & Hajnsek, I. (2014). Snow height determination by polarimetric phase differences in X-Band SAR Data. *IEEE Journal of Selected Topics in Applied Earth Observations and Remote Sensing*, *7*(9), 3794–3810. https://doi.org/10.1109/JSTARS.2014.2323199
Leinss, S., Wiesmann, A., Lemmetyinen, J., & Hajnsek, I. (2015). Snow Water Equivalent of Dry Snow Measured by Differential Interferometry. *IEEE Journal of Selected Topics in Applied Earth Observations and Remote Sensing*, *8*(8), 3773–3790. https://doi.org/10.1109/JSTARS.2015.2432031
Li, H., Wang, Z., He, G., & Man, W. (2017). Estimating Snow Depth and Snow Water Equivalence Using Repeat-Pass Interferometric SAR in the Northern Piedmont Region of the Tianshan Mountains. *Journal of Sensors*, *2017*, 1–17. https://doi.org/10.1155/2017/8739598
Liang, X., Lettenmaier, D. P., Wood, E. F., & Burges, S. J. (1994). A simple hydrologically based model of land surface water and energy fluxes for general circulation models. *Journal of Geophysical Research*, *99*(D7), 14415–14428. https://doi.org/10.1029/94JD00483
Liu, Y., Li, L., Yang, J., Chen, X., & Hao, J. (2017). Estimating snow depth using multi-source data fusion based on the D-InSAR method and 3DVAR fusion algorithm. *Remote Sensing*, *9*(11). https://doi.org/10.3390/rs9111195
Luo, X., Richter, B., & Cole, A. (2014). *GLONASS only and BeiDou only RTK Positioning. Leica Geosystems AG*. Heerbrugg, Switzerland. Retrieved from https://leica-geosystems.com/-/media/Files/LeicaGeosystems/Products/White Papers/GLONASS_BeiDou_RTK_Positioning_WPA.ashx
Majumdar, S., Thakur, P. K., Chang, L., & Kumar, S. (2019). X-band Polarimetric SAR Copolar Phase Difference for Fresh Snow Depth Estimation in the Northwestern Himalayan watershed. Submitted to IGARSS 2019.
Massonnet, D., & Feigl, K. L. (1998). Radar interferometry and its application to changes in the Earth's surface. *Reviews of Geophysics*, *36*(4), 441–500. https://doi.org/10.1029/97RG03139
Matzler, C. (1996). Microwave permittivity of dry snow. *IEEE Transactions on Geoscience and Remote Sensing*, *34*(2), 573–581. https://doi.org/10.1109/36.485133
Mätzler, C. (2002). Relation between grain-size and correlation length of snow. *Journal of Glaciology*, *48*(162), 461–466. https://doi.org/10.3189/172756502781831287
Matzler, C., & Wegmuller, U. (1987). Dielectric properties of freshwater ice at microwave frequencies. *Journal of Physics D: Applied Physics*, *20*(12), 1623–1630. https://doi.org/10.1088/0022-3727/20/12/013
Mätzler, C., & Wiesmann, A. (1999). Extension of the Microwave Emission Model of Layered Snowpacks to Coarse-Grained Snow. *Remote Sensing of Environment*, *70*(3), 317–325. https://doi.org/10.1016/S0034-4257(99)00047-4
Mestre-Quereda, A., Lopez-Sanchez, J. M., Selva, J., & Gonzalez, P. J. (2018). An Improved Phase Filter for Differential SAR Interferometry Based on an Iterative Method. *IEEE Transactions on Geoscience*

and Remote Sensing, *56*(8), 4477–4491. https://doi.org/10.1109/TGRS.2018.2820725
Moller, D., Hensley, S., Sadowy, G. A., Fisher, C. D., Michel, T., Zawadzki, M., & Rignot, E. (2011). The Glacier and Land Ice Surface Topography Interferometer: An Airborne Proof-of-Concept Demonstration of High-Precision Ka-Band Single-Pass Elevation Mapping. *IEEE Transactions on Geoscience and Remote Sensing*, *49*(2), 827–842. https://doi.org/10.1109/TGRS.2010.2057254
Moreira, A., Prats-Iraola, P., Younis, M., Krieger, G., Hajnsek, I., & Papathanassiou, K. P. (2013). A tutorial on synthetic aperture radar. *IEEE Geoscience and Remote Sensing Magazine*, *1*(1), 6–43. https://doi.org/10.1109/MGRS.2013.2248301
Negi, H. S., Kulkarni, A. V., & Semwal, B. S. (2009). Estimation of snow cover distribution in Beas basin, Indian Himalaya using satellite data and ground measurements. *Journal of Earth System Science*, *118*(5), 525–538. https://doi.org/10.1007/s12040-009-0039-0
Papathanassiou, K. P., & Cloude, S. R. (2001). Single-baseline polarimetric SAR interferometry. *IEEE Transactions on Geoscience and Remote Sensing*, *39*(11), 2352–2363. https://doi.org/10.1109/36.964971
Parrella, G., Hajnsek, I., & Papathanassiou, K. P. (2013). On the Interpretation of L- and P-Band PolSAR Signatures of Polythermal Glaciers. In *6th International Workshop on Science and Applications of SAR Polarimetry Polarimetric Interferometry (PolInSAR'13)* (pp. 1–6). Frascati, Italy. Retrieved from https://elib.dlr.de/78902/1/s7_parre.pdf
Pepe, A., & Calò, F. (2017). A Review of Interferometric Synthetic Aperture RADAR (InSAR) Multi-Track Approaches for the Retrieval of Earth's Surface Displacements. *Applied Sciences*, *7*(12), 1264. https://doi.org/10.3390/app7121264
Petrenko, V. F., & Whitworth, R. W. (2002). *Physics of Ice*. New York: Oxford University Press. https://doi.org/10.1093/acprof:oso/9780198518945.001.0001
Picard, G., Sandells, M., & Löwe, H. (2018). SMRT: an active–passive microwave radiative transfer model for snow with multiple microstructure and scattering formulations (v1.0). *Geoscientific Model Development*, *11*(7), 2763–2788. https://doi.org/10.5194/gmd-11-2763-2018
PostgreSQL. (2019). PostgreSQL. Retrieved February 19, 2019, from https://www.postgresql.org/
QGIS. (2016). Changelog for QGIS 2.18. Retrieved February 8, 2019, from https://www.qgis.org/en/site/forusers/visualchangelog218/index.html
Rees, W. G. (2000). The accuracy of Digital Elevation Models interpolated to higher resolutions. *International Journal of Remote Sensing*, *21*(1), 7–20. https://doi.org/10.1080/014311600210957
Reynolds, B. (1983). The chemical composition of snow at a rural upland site in Mid-wales. *Atmospheric Environment (1967)*, *17*(9), 1849–1851. https://doi.org/10.1016/0004-6981(83)90193-2
Riche, F., Montagnat, M., & Schneebeli, M. (2013). Evolution of crystal orientation in snow during temperature gradient metamorphism. *Journal of Glaciology*, *59*(213), 47–55. https://doi.org/10.3189/2013JoG12J116
Roebber, P. J., Bruening, S. L., Schultz, D. M., & Cortinas, J. V. (2003). Improving Snowfall Forecasting by Diagnosing Snow Density. *Weather and Forecasting*, *18*(2), 264–287. https://doi.org/10.1175/1520-0434(2003)018<0264:ISFBDS>2.0.CO;2
Rosen, P., Hensley, S., Shaffer, S., Edelstein, W., Kim, Y., Kumar, R., … Sagi, R. (2017). The NASA-ISRO SAR (NISAR) mission dual-band radar instrument preliminary design. In *2017 IEEE International Geoscience and Remote Sensing Symposium (IGARSS)* (pp. 3832–3835). IEEE. https://doi.org/10.1109/IGARSS.2017.8127836
Royer, A., Roy, A., Montpetit, B., Saint-Jean-Rondeau, O., Picard, G., Brucker, L., & Langlois, A. (2017). Comparison of commonly-used microwave radiative transfer models for snow remote sensing. *Remote Sensing of Environment*, *190*, 247–259. https://doi.org/10.1016/j.rse.2016.12.020
Sharma, J. J., Hajnsek, I., Papathanassiou, K. P., & Moreira, A. (2013). Estimation of Glacier Ice Extinction Using Long-Wavelength Airborne Pol-InSAR. *IEEE Transactions on Geoscience and Remote Sensing*, *51*(6), 3715–3732. https://doi.org/10.1109/TGRS.2012.2220855
Sihvola, A. (1999). *Electromagnetic Mixing Formulas and Applications* (1st ed.). UK: The Institution of Engineering and Technology. https://doi.org/10.1049/PBEW047E
Singh, G., Venkataraman, G., Yamaguchi, Y., & Park, S.-E. (2014). Capability Assessment of Fully Polarimetric ALOS–PALSAR Data for Discriminating Wet Snow From Other Scattering Types in Mountainous Regions. *IEEE Transactions on Geoscience and Remote Sensing*, *52*(2), 1177–1196. https://doi.org/10.1109/TGRS.2013.2248369
Singh, G., Verma, A., Kumar, S., Snehmani, Ganju, A., Yamaguchi, Y., & Kulkarni, A. V. (2017).

Snowpack Density Retrieval Using Fully Polarimetric TerraSAR-X Data in the Himalayas. *IEEE Transactions on Geoscience and Remote Sensing*, *55*(11), 6320–6329. https://doi.org/10.1109/TGRS.2017.2725979
Snehmani, Venkataraman, G., Nigam, A. K., & Singh, G. (2010). Development of an inversion algorithm for dry snow density estimation and its application with ENVISAT-ASAR dual co-polarization data. *Geocarto International*, *25*(8), 597–616. https://doi.org/10.1080/10106049.2010.516843
Spencer, M. K., Alley, R. B., & Creyts, T. T. (2001). Preliminary firn-densification model with 38-site dataset. *Journal of Glaciology*, *47*(159), 671–676. https://doi.org/10.3189/172756501781831765
Speziali, F., Trampuz, C., Placidi, S., Hendriks, L. C. I., Ludwig, M., & Meta, A. (2018). Development of the Multichannel Interferometric Ka-Band Airborne SAR Instrument (KaSAR). In *EUSAR 2018; 12th European Conference on Synthetic Aperture Radar* (pp. 1–5). Aachen, Germany. Retrieved from https://ieeexplore.ieee.org/abstract/document/8438262
Srinivasulu, J., & Kulkarni, A. V. (2004). Estimation of spectral reflectance of snow from IRS-1D LISS-III sensor over the Himalayan terrain. *Proceedings of the Indian Academy of Sciences, Earth and Planetary Sciences*, *113*(1), 117–128. https://doi.org/10.1007/BF02702003
Sturm, M., & Benson, C. (2004). Scales of spatial heterogeneity for perennial and seasonal snow layers. *Annals of Glaciology*, *38*, 253–260. https://doi.org/10.3189/172756404781815112
Takala, M., Luojus, K., Pulliainen, J., Derksen, C., Lemmetyinen, J., Kärnä, J.-P., … Bojkov, B. (2011). Estimating northern hemisphere snow water equivalent for climate research through assimilation of space-borne radiometer data and ground-based measurements. *Remote Sensing of Environment*, *115*(12), 3517–3529. https://doi.org/10.1016/j.rse.2011.08.014
Tan, M. L., Ficklin, D. L., Dixon, B., Ibrahim, A. L., Yusop, Z., & Chaplot, V. (2015). Impacts of DEM resolution, source, and resampling technique on SWAT-simulated streamflow. *Applied Geography*, *63*, 357–368. https://doi.org/10.1016/j.apgeog.2015.07.014
Tedesco, M. (Ed.). (2015). *Remote Sensing of the Cryosphere*. Chichester, UK: John Wiley & Sons, Ltd. https://doi.org/10.1002/9781118368909
Thakur, P. K., Aggarwal, S. P., Arun, G., Sood, S., Senthil Kumar, A., Mani, S., & Dobhal, D. P. (2017). Estimation of Snow Cover Area, Snow Physical Properties and Glacier Classification in Parts of Western Himalayas Using C-Band SAR Data. *Journal of the Indian Society of Remote Sensing*, *45*(3), 525–539. https://doi.org/10.1007/s12524-016-0609-y
Thakur, P. K., Aggarwal, S. P., Garg, P. K., Garg, R. D., Mani, S., Pandit, A., & Kumar, S. (2012). Snow physical parameters estimation using space-based Synthetic Aperture Radar. *Geocarto International*, *27*(3), 263–288. https://doi.org/10.1080/10106049.2012.672477
Tsang, L., Pan, J., Liang, D., Li, Z., Cline, D. W., & Tan, Y. (2007). Modeling Active Microwave Remote Sensing of Snow Using Dense Media Radiative Transfer (DMRT) Theory With Multiple-Scattering Effects. *IEEE Transactions on Geoscience and Remote Sensing*, *45*(4), 990–1004. https://doi.org/10.1109/TGRS.2006.888854
Tuzet, F., Dumont, M., Lafaysse, M., Picard, G., Arnaud, L., Voisin, D., … Morin, S. (2017). A multilayer physically based snowpack model simulating direct and indirect radiative impacts of light-absorbing impurities in snow. *The Cryosphere*, *11*(6), 2633–2653. https://doi.org/10.5194/tc-11-2633-2017
Ulaby, F., Stiles, W., Dellwig, L., & Hanson, B. (1977). Experiments on the Radar Backscatter of Snow. *IEEE Transactions on Geoscience Electronics*, *15*(4), 185–189. https://doi.org/10.1109/TGE.1977.294490
Usami, N., Muhuri, A., Bhattacharya, A., & Hirose, A. (2016). PolSAR Wet Snow Mapping With Incidence Angle Information. *IEEE Geoscience and Remote Sensing Letters*, *13*(12), 2029–2033. https://doi.org/10.1109/LGRS.2016.2621891
Warren, S. G., & Brandt, R. E. (2008). Optical constants of ice from the ultraviolet to the microwave: A revised compilation. *Journal of Geophysical Research*, *113*(D14), 1–10. https://doi.org/10.1029/2007JD009744
Weisstein, E. W. (2019). Sinc Function. In *MathWorld--A Wolfram Web Resource*. Retrieved from http://mathworld.wolfram.com/SincFunction.html
Wiesmann, A., & Mätzler, C. (1999). Microwave Emission Model of Layered Snowpacks. *Remote Sensing of Environment*, *70*(3), 307–316. https://doi.org/10.1016/S0034-4257(99)00046-2
Winsvold, S. H., Kääb, A., Nuth, C., Andreassen, L. M., van Pelt, W. J. J., & Schellenberger, T. (2018). Using SAR satellite data time series for regional glacier mapping. *The Cryosphere*, *12*(3), 867–890.

https://doi.org/10.5194/tc-12-867-2018
Yueh, S. H., Dinardo, S. J., Akgiray, A., West, R., Cline, D. W., & Elder, K. (2009). Airborne Ku-Band Polarimetric Radar Remote Sensing of Terrestrial Snow Cover. *IEEE Transactions on Geoscience and Remote Sensing*, *47*(10), 3347–3364. https://doi.org/10.1109/TGRS.2009.2022945
Zheng, Z., Kirchner, P. B., & Bales, R. C. (2016). Topographic and vegetation effects on snow accumulation in the southern Sierra Nevada: a statistical summary from lidar data. *The Cryosphere*, *10*(1), 257–269. https://doi.org/10.5194/tc-10-257-2016
Zhu, Z., Wang, S., & Woodcock, C. E. (2015). Improvement and expansion of the Fmask algorithm: cloud, cloud shadow, and snow detection for Landsats 4–7, 8, and Sentinel 2 images. *Remote Sensing of Environment*, *159*, 269–277. https://doi.org/10.1016/j.rse.2014.12.014
Zuniga, M., Habashy, T., & Kong, J. (1979). Active Remote Sensing of Layered Random Media. *IEEE Transactions on Geoscience Electronics*, *17*(4), 296–302. https://doi.org/10.1109/TGE.1979.294658

APPENDIX-A

1. Basic Principles of SAR

Synthetic Aperture Radar is an active system which measures the scattering of a transmitted pulse from an object in a particular microwave frequency band (Lee & Pottier, 2009). The commonly used microwave bands for spaceborne systems are listed below in Table A- 1.

Table A- 1: Operating bands of some of the popular or upcoming SAR satellites.

Band	Popular Satellites	Frequency (GHz)	Wavelength (cm)
X	TerraSAR-X, TanDEM-X	12-8	2.5-3.8
C	RADARSAT-2, SENTINEL-1	8-4	3.8-7.5
S	NISAR (upcoming)	4-2	7.5-15.0
L	ALOS 2 PALSAR2, NISAR (upcoming), Tandem-L (upcoming)	2-1	15.0-30.0

The PolSAR technique works on the basis of the polarisation behaviour or the polarimetric characteristics of a target. Evidently, the polarisation states of the incident and scattered waves can be represented in terms of the radar backscattering matrix $[S]$ (Lee & Pottier, 2009) as given by Eq. (A1).

$$[S] = \begin{bmatrix} S_{HH} & S_{HV} \\ S_{VH} & S_{VV} \end{bmatrix} \tag{A1}$$

where, S_{HH}, and S_{VV} are the copolarised channels, and S_{HV}, and S_{VH} are the cross-polarised channels respectively.

In the monostatic scenario, since the $S_{HV} = S_{VH}$ reflection symmetry is assumed, the total power P received by the SAR sensor (Lee & Pottier, 2009) is defined in Eq. (A2).

$$P = |S_{HH}|^2 + 2|S_{HV}|^2 + |S_{VV}|^2 \tag{A2}$$

2. Polarimetric Decompositions

a) Coherent Decompositions: In the coherent decompositions, $[S]$ is defined in terms of a combination of simple scattering returns. The Pauli decomposition falls in this category wherein the Pauli basis, ψ_p (Eq. (A3)) is used for the decomposition process (Lee & Pottier, 2009).

$$\psi_p = \frac{1}{\sqrt{2}}\{[\sigma]_i\}\ \forall i \in [0, 3] \tag{A3}$$

where,

$$[\sigma]_0 = \begin{bmatrix} 1 & 0 \\ 0 & 1 \end{bmatrix}, [\sigma]_1 = \begin{bmatrix} 1 & 0 \\ 0 & -1 \end{bmatrix}, [\sigma]_2 = \begin{bmatrix} 0 & 1 \\ 1 & 0 \end{bmatrix}, [\sigma]_3 = \begin{bmatrix} 0 & -1 \\ 1 & 0 \end{bmatrix}$$

Here $[\sigma]_i$ are the Pauli spin matrices using which the Pauli decomposition is given by Eq. (A4).

$$[S] = \begin{bmatrix} S_{HH} & S_{HV} \\ S_{VH} & S_{VV} \end{bmatrix} = \frac{\alpha_p}{\sqrt{2}}[\sigma]_0 + \frac{\beta_p}{\sqrt{2}}[\sigma]_1 + \frac{\gamma_p}{\sqrt{2}}[\sigma]_2 \tag{A4}$$

where,

$$\alpha_p = \frac{S_{HH} + S_{VV}}{\sqrt{2}}, \beta_p = \frac{S_{HH} - S_{VV}}{\sqrt{2}}, \gamma_p = \sqrt{2}S_{HV}$$

Intriguingly, the first, second and third terms in Eq. (A4) denote the general odd bounce scattering, even bounce scattering, and volume scattering respectively (Lee & Pottier, 2009). Moreover, the total power P in Eq. (A2) can now be defined using the weight coefficients α_p, β_p, and γ_p as shown in Eq. (A5).

$$P = |\alpha_p|^2 + |\beta_p|^2 + |\gamma_p|^2 \tag{A5}$$

where, $|\alpha_p|^2$, $|\beta_p|^2$, and $|\gamma_p|^2$ denote the scattering powers of the three aforementioned scattering mechanism respectively.

b) Incoherent Decompositions: One of the limitations of the coherent decomposition scheme is that it can only identify pure scattering mechanisms which are often not the case in reality (Lee & Pottier, 2009). The idea of the incoherent decomposition techniques is to extract the polarimetric information from the statistically defined 3×3 covariance $\langle[C_3]\rangle$ and coherency matrices $\langle[T_3]\rangle$ (Lee & Pottier, 2009) as given by Eq. (A6) and Eq.(A7) respectively.

$$[C_3] = \begin{bmatrix} |S_{HH}|^2 & \sqrt{2}S_{HH}S_{VV}^* & S_{HH}S_{VV}^* \\ \sqrt{2}S_{HV}S_{HH}^* & 2|S_{HV}|^2 & \sqrt{2}S_{HV}S_{VV}^* \\ S_{VV}S_{HH}^* & \sqrt{2}S_{VV}S_{HV}^* & |S_{VV}|^2 \end{bmatrix} \tag{A6}$$

$$[T_3] = \frac{1}{2}\begin{bmatrix} |S_{HH}+S_{VV}|^2 & (S_{HH}+S_{VV})(S_{HH}-S_{VV})^* & 2(S_{HH}+S_{VV})S_{HV}^* \\ (S_{HH}-S_{VV})(S_{HH}+S_{VV})^* & |S_{HH}-S_{VV}|^2 & 2(S_{HH}-S_{VV})S_{HV}^* \\ 2S_{HV}(S_{HH}+S_{VV}) & 2S_{HV}(S_{HH}-S_{VV})^* & 4|S_{HV}|^2 \end{bmatrix} \tag{A7}$$

In this context, the H-A-α decomposition is a widely used incoherent decomposition technique based on the eigenvalue decomposition scheme, wherein it is possible to show that:

$$\langle[T_3]\rangle = \sum_{i=1}^{3} \lambda_i \overrightarrow{w_i}\overrightarrow{w_i}^{\dagger} \tag{A8}$$

where, † represents the conjugate transpose operator, λ_i are the eigenvalues and $\overrightarrow{w_i}$ are the eigenvectors which are defined in Eq. (A9).

$$\overrightarrow{w_i} = [\cos\alpha_i \quad \sin\alpha_i\cos\beta_i e^{j\delta_i} \quad \sin\alpha_i\sin\beta_i e^{j\mu_i}]^T \tag{A9}$$

where, $\overrightarrow{w_i}$ is the general form of Eq. (16) and the symbols have the same meaning.

The H-A-α decomposition can be used to identify different scattering mechanism, a brief discussion on which is provided in section 4.4.2. Nevertheless, the following parameters defined by Eq. (A10)-Eq. (A14) are useful for performing any advanced analysis:

Table A- 2: Parameters involved in the H-A-α decomposition.

Parameter	Equation	
Total Power (P)	$P = \sum_{i=1}^{3} \lambda_i$	(A10)
Eigenvalue Probabilities (p_i)	$p_i = \frac{\lambda_i}{P}$	(A11)
Entropy (H)	$H = -\sum_{i=1}^{3} p_i \log_3(p_i)$	(A12)
Anisotropy (A)	$A = \frac{\lambda_2 - \lambda_3}{\lambda_2 + \lambda_3}$	(A13)
Mean alpha ($\bar{\alpha}$)	$\bar{\alpha} = \sum_{i=1}^{3} p_i \alpha_i$	(A14)

3. SAR Acquisition Modes

The most common image acquisition modes used in the spaceborne SAR systems are the Stripmap (SM), Spotlight (SL), and the ScanSAR (SC). In the SM mode, the radar antenna maintains a fixed viewing angle with respect to the azimuth direction. In the case of the SL mode, the azimuth resolution is improved due to the increased scene focusing time. However, this results in a lower swath as compared to the SM and SC modes. When the SAR images are acquired in the SC mode, significant ground coverage can be obtained at the cost of lower spatial resolution (Brunner, 2009). The SAR operation mode schematics are provided in Fig A- 1.

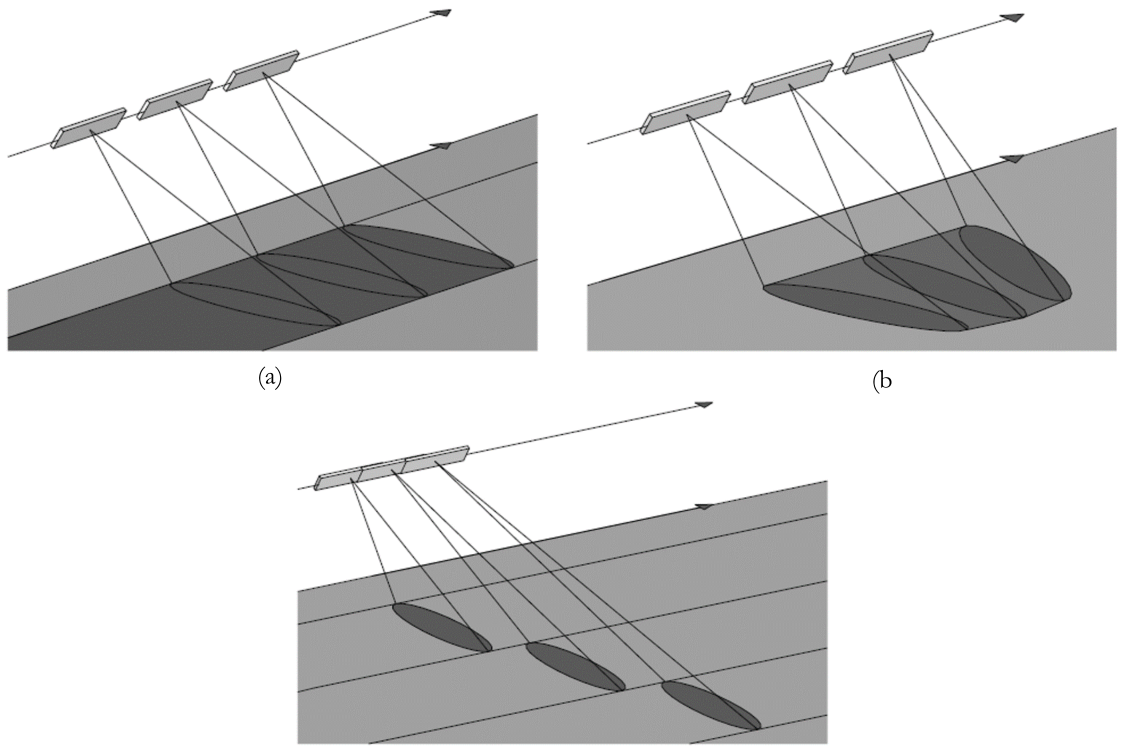

Fig A- 1: SAR operation modes, (a) Stripmap, (b) Spotlight, and (c) ScanSAR (Brunner, 2009).

APPENDIX-B

1. DEM Stacking

In order to prepare a sufficiently accurate DEM, a least pixelwise error technique had been adopted which basically selects the least erroneous pixel compared to a reference DEM (SRTM 30 m in this case) from all the HH and VV channel DEMs computed through the standard InSAR processing (Ferretti, Monti-Guarnieri, C., & Rocca, 2007) of the available datasets (Table 2).

At first, a single DEM (April 15, 2017) was checked with the SRTM 30 m DEM which had been resampled (bilinear interpolation) to 3 m. The error analysis showed substantial absolute errors surrounding the Dhundi region (more than 600 m) possibly due to the time of the acquisitions (most taken during the winters) and the improper spatial baselines ($B_{\perp} \in [150, 300]$ is the optimal perpendicular baseline for the TanDEM-X acquisitions) (Ferretti et al., 2007). Moreover, large unwrapping errors are quite common in mountainous regions (Chen & Zebker, 2002).

When this technique was applied, the overall errors reduced significantly, with the mean absolute error reducing from nearly 200 m to 62 m. However, there were still large errors presenting over Dhundi, whereas the Kothi region displayed errors in the order of 1 m. The absolute error map and its histogram are depicted in Fig A- 2(a) and Fig A- 2 (b) respectively. Additionally, the SRTM (3 m resampled) and the produced (stacked) DEM maps are shown in Fig A- 2 (c) and Fig A- 2 (d) respectively.

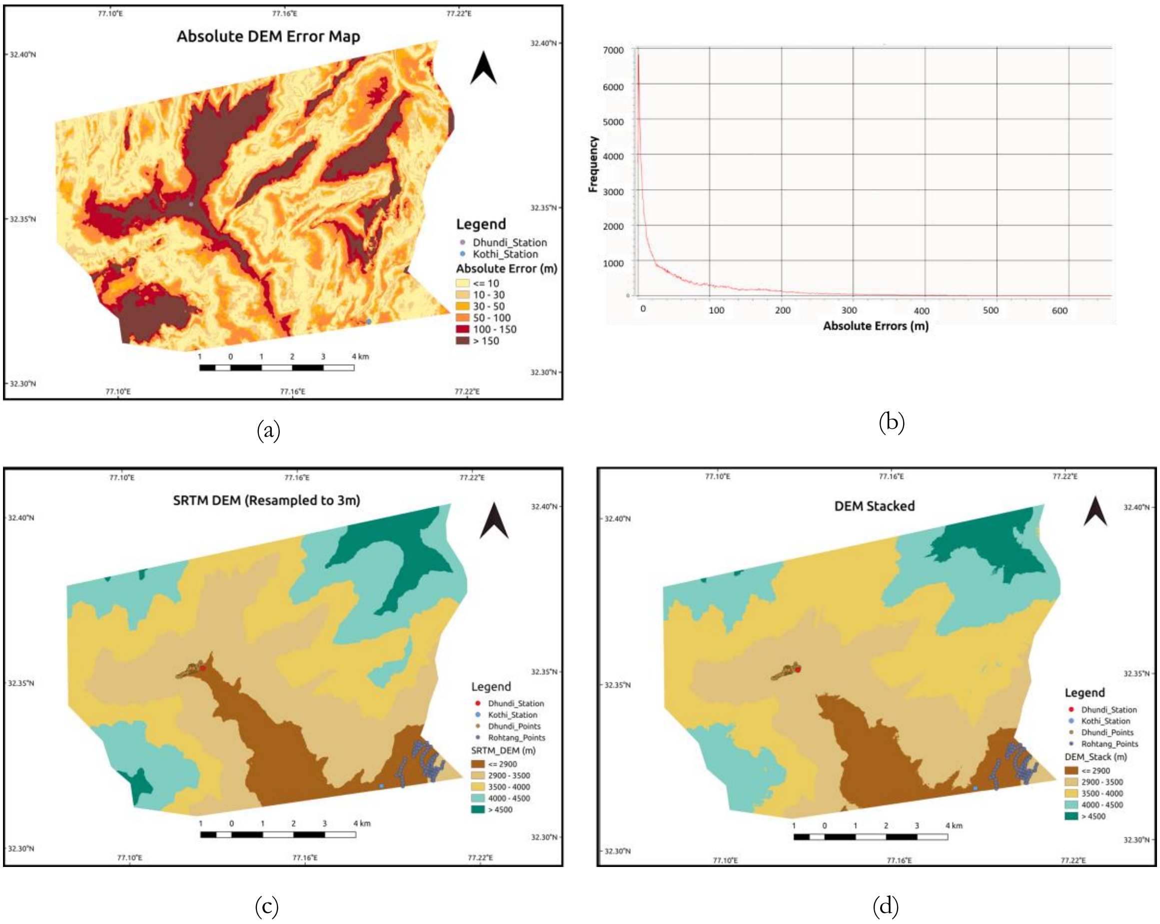

Fig A- 2: (a) Absolute error map and (b) its corresponding histogram generated by comparing (c) the SRTM 3 m resampled DEM, and (d) the stacked DEM based on the least pixelwise error technique. The DGPS readings acquired during the fieldwork are also marked.

APPENDIX-C

1. Snow Particle Axial Ratio

The snow or ice particle axial ratio (a_x/a_z) discussed in section 2.2.1 is an important component in the FSD inversion model. By keeping the other model parameters— the CPD and FSD ensemble averaging windows fixed at 3×3 and 65×65 respectively, the FSD sensitivity to the axial ratio has been checked wherein the fresh snow density, $\rho_f = 0.07$ g/cm^3 is used. The obtained graph depicted in Fig A- 3 shows that $a_x/a_z = 1.6$ provides the most accurate (~99.11%) $\mu_f \approx 18.16$ cm ($\sigma_f \approx 0.06$ cm) estimate. Therefore, this sensitivity analysis proves that the FSD inversion model can be further improved.

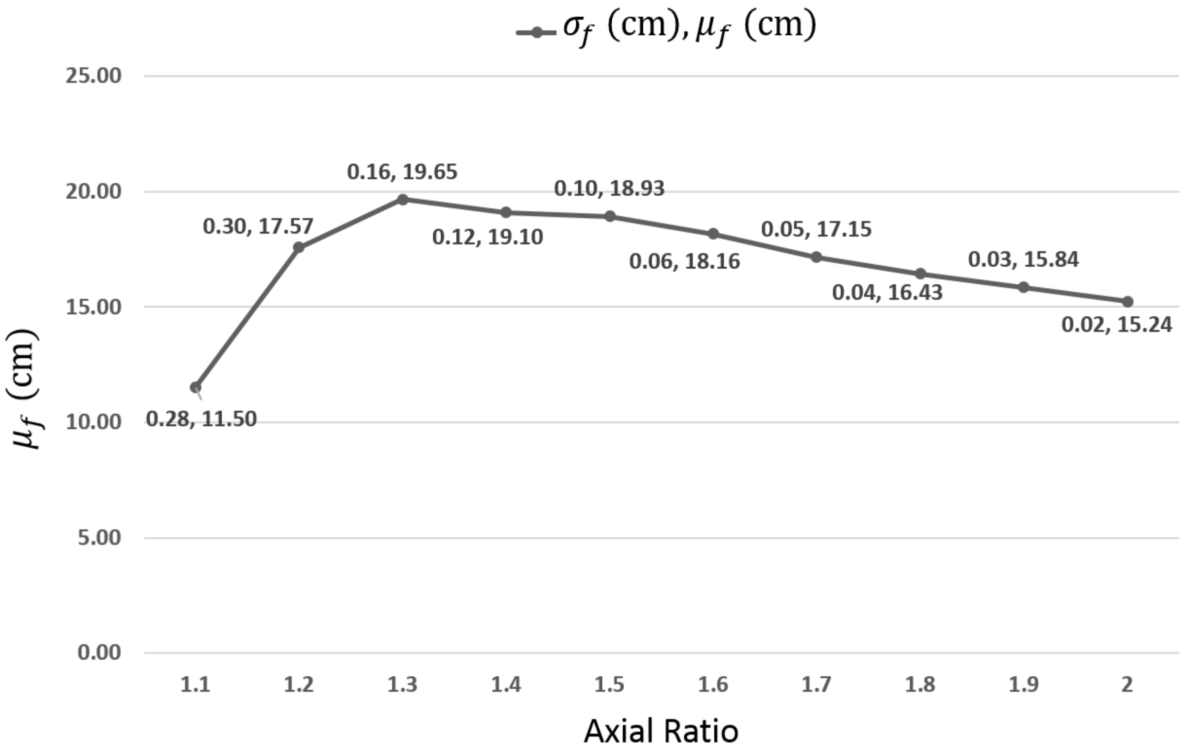

Fig A- 3: FSD variations with respect to the axial ratio changes (all values are rounded to 2 decimal places). It is noteworthy that, Leinss et al. (2014) in their work set $a_x/a_z = 2$ whereas in section 4.2, $a_x/a_z = 1.5$ is used.

2. Descriptive Statistics

Table A- 3: Some common formulas used in descriptive statistics.

Metric	Equation	
RMSE	$RMSE = \sqrt{\frac{\sum_{i=1}^{N}\left(X_i' - X_i\right)^2}{N}}$	(A15)
Sample Standard Deviation	$s = \sqrt{\frac{\sum_{i=1}^{N}(X_i - \bar{X})^2}{N-1}}$	(A16)
Standard Error	$s_{err} = s/\sqrt{N}$	(A17)

where, X_i', X_i, $\bar{X}$, and N are the predicted and observed values, the sample mean, and size respectively.